Simulación del Experimento GRAAL: La Plataforma Solar de Almería como telescopio de rayos γ

Memoria presentada por
D. David Martínez Borque
para optar al grado de Doctor en Ciencias Físicas.

Dirigida por el profesor
D. Fernando Arqueros Martínez

Departamento de Física Atómica, Molecular y Nuclear
Facultad de Ciencias Físicas
Universidad Complutense de Madrid
10th October 2001

Contents

Chapter 1

Gamma-ray astronomy

General description of present-day γ-ray astronomy.

Chapter 2

The GRAAL experiment

2.1 Working principles

As already mentioned, the GRAAL project makes use of the existing CESA-1 array of heliostats at the Plataforma Solar de Almería as a non-imaging Čerenkov telescope for γ-ray astronomy.

A central tower solar plant, as the CESA-1 array, uses hundreds of individual mirrors (*heliostats*) to reflect sunlight into a concentrator located at the top of a tower, where water, oil, sodium or other substance is heated up to produce electricity.

In GRAAL, we use these heliostats to reflect Čerenkov light generated by EAS produced by high energy primaries (hadrons, gamma-rays, ...) into concentrators located in the central tower, which focus the light onto one photo-multiplier tube (PMT). When the signals produced in the various PMT's are compatible with the expected signal for a shower (trigger condition), the time traces are recorded on magnetic tapes for later analysis.

As concentrators of the Čerenkov light in the tower we use Winston cones, each with an angular acceptance of 10 degrees. This means that each one of the cones collects light from all the heliostats in its field of view. In this way the light from several heliostats is collected into a single PMT, which leads to a much simpler electronic setup as compared with other solar-plant experiments where one PMT collects light reflected only by one heliostat.

Each one of those heliostats is a self-steered mirror controlled form a central computer with a reflecting area of the order of 40 m^2. During normal operation these mirrors track the Sun in such a way that its light is reflected and concentrated onto the collecting device. The mirrors of the heliostats are not made of a single piece, but consist of several smaller pieces called *facets* which are assembled on a frame that keeps them aligned in a way that all of them work as a single big mirror. The surface of the facets need not be of a high precision, as the intended resolution is not high (by no means near the precision needed by optical telescopes), and the alignment precision of the different facets on the frame also needn't be very high. Overall, the measured resolution (1 sigma) is of the order of 0.2 deg, which is enough for a non-imaging γ-ray Čerenkov telescope, since a typical shower has a size of around 0.6 deg diameter.

Due to the large distances from the collectors to the mirrors, typical focal lengths are very big, of the order of 100 meters. This fact, in conjunction with the diameter of the collecting Winston cones (1.2 m), lead to a narrow field of view, of about 0.6 degrees, which is nearly the typical size of an EAS. This fact will impose severe restrictions to our observing methods and performance, as will be shown.

2.2 Elements of GRAAL

2.2.1 The site

The Plataforma Solar de Almería (PSA) is a European research institution for solar thermal concentrating technologies operated by the Spanish "Centro de Investigaciones Energéticas, Medioambientales y Tecnológicas" (CIEMAT). It is located in Southern Spain ($2^o21'\,E; 37^o5'\,N$), in the Tabernas desert, at an altitude of 505 m a.s.l., very near the astronomical observatory of Calar Alto.

The weather is very good with an average of 182 clear days/year, 38 overcast days/year and less that 10 rainy days/year [1]. Additionally, wind speed is usually very low (less than 30 Km/h). Mean humidity during good observation nights is below 60% ($\sim$50% of the observing nights), but very high humidity with values above 90% are not rare (around 5% of all observation nights).

The nearest large city is Almería, at about 40 Km to the Southwest, which is very convenient for displacement. Light contamination is low, thanks to a mountain range that blocks part of the scattered light. Some scattered light from the nearest village, Tabernas, is unavoidable. Several country houses and bars located nearby don't produce much light contamination. In general the site is very dark, with worse observing conditions to the Southwest. The total night sky background (NSB) was measured at the PSA in February 1995, on a very clear night (solar constant of the previous day was about $1\,\mathrm{kW/m^2}$) using a single photon counting method developed by Mirzoyan and Lorenz [2] (wide angle setup). The total single photo-electron count rate on a FEU-130 photo-multiplier operated with voltages between 1800 and 2100 V, with a viewing angle of 0.13 sr around the zenith, was determined to be $1.2 \cdot 10^6$ counts/sec with a 2 mm diameter diaphragm covering the center of the photo-cathode. With the FEU-130 efficiencies obtained from [2] we infer a wide angle NSB between 300 and 600 nm of $3 \cdot 10^{12}$ photons/m^2/sec/sr which is a value similar to that of very good astronomical sites [2].

2.2.2 The heliostat field CESA-1

The **CESA-1** heliostat field is the largest central-tower array at the PSA, with 350 heliostats, **39.6 m^2** segmented mirrors, to the north of a central tower 80 m high. Out of the 350 heliostats, 59 are used in the experiment, giving a total area of nearly 2500 m^2, making for the largest telescope in the world.

Each heliostat is made up of **24 facets**, which are screwed to a metallic frame. For monetary reasons the facets are mass-produced with fixed curvature radii by groups (in CESA-1 facets were built with focal lengths of 90, 100, 125 and 200 m). Therefore for each heliostat, the focal length of its facets does not match exactly the distance from the heliostat to the target at the tower, which introduces a blurring in the images.

In order to correct for this effect, within each heliostat, the facets must be aligned in such a way that the images reflected by each one of the facets are located at the same place in the tower. This procedure is called canting and is routinely done by the staff at the PSA. Two procedures are used:

Off-axis Using the Sun near noon. At this time the different facets are canted, by hand, so that the images of all the facets of the heliostat overlap on a target at the tower.

On-axis Using a laser attached to the top of the tower, the facets are adjusted by hand, so that all of them reflect the laser-beam to the same point.

The second method is the preferred one as it allows for a better reproducibility, and moreover, the images produced by heliostats *canted* in this way produce less elongated images for high off-axis angles. A comparison of both methods can be seen in figure 2.1 [3].

The **reflectivity** of the mirrors is quite high (above 95%) in the wavelength range 400–550 nm and falls steeply toward lower wavelengths as is shown in figure 2.2. This curve shows the reflectivity of the mirrors after

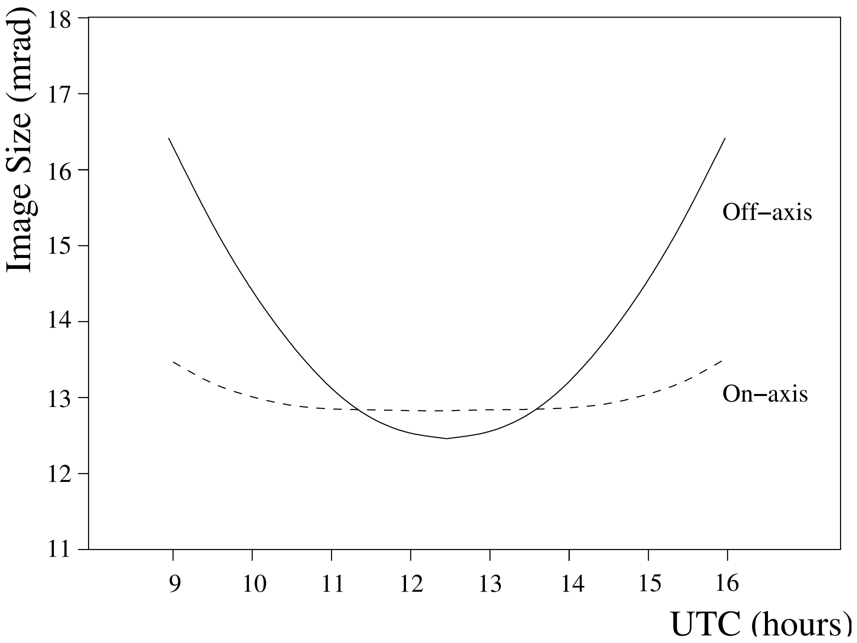

Figure 2.1: Off-axis *canting, which is done with the Sun, produces better images near noon, but for large off-axis incidence angles, the* on-axis *canting with a laser light gives better results [3].*

being washed. Due to dust, reflectivity falls over time down to around 80% within a month. The staff at the PSA has instructions to routinely wash all the mirrors, procedure that can be done in one day, and which keeps an overall reflectivity above 90% most of the observing time. In any case measures of the reflectivity are logged down every observation night.

The **steering** of the heliostats is accomplished via two step motors that control an altazimuth mount. To steer the heliostats to the observation positions, the motor movement must be communicated to each heliostat in step values for both axis, azimuth and elevation. The maximum precision in the steering of the heliostats comes from the minimum increment in motor steps, that is, 1 motor step, which is equivalent to 0.044 degrees. The communication is made via a serial line from the central control computer. The whole field is controlled with just 16 serial lines, which means that each serial line supports around 19 heliostats. The mean refresh rate in the steering of the heliostats is 4 seconds, which gives a maximum error, for observation of objects in the celestial equator, of just 0.017 degrees, well below the 0.044 degrees precision due to the motor steps.

The calculations needed for the correct orientation of the heliostats is done

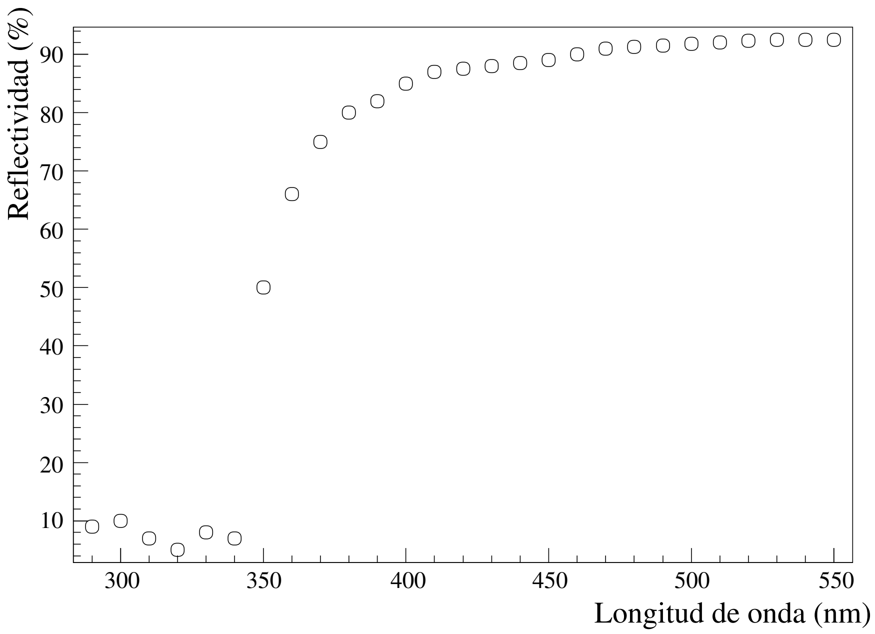

Figure 2.2: *The reflectivity curve of the mirrors of the heliostats as a function of the wavelength.*

with a program developed by our collaboration. This program calculates every second the motor-step values for every heliostat in the field and then sends the commands via the serial lines. It was impossible to use the main steering program at the PSA, because it was only prepared to track the Sun.

The new program has several steering modes for the heliostats:

Star Tracking Track of a celestial object. This is the main feature used for tracking the desired object during data taking. Heliostats are positioned in such a way that light coming from the direction of the observed object is reflected onto the defined focuses. Positions are refreshed every 4 seconds.

Fixed Position All the heliostats are aimed so that light coming from a fixed point in the atmosphere reflects onto the focal points at the tower. This point is fixed over time with respect to the altazimuth system of reference, and therefore, once the correct position of the heliostats is reached, no further movement is needed.

Manual Mode The motor steps are not calculated by the program, but introduced manually. Once the heliostat reaches the desired position, it stays there until further orders are received. Useful for testing or security reasons.

Change of Focus Several focusing points can be defined at the tower, each one for a different group of heliostats. This command chooses the desired focusing points.

Apart from this basic commands there are two major working modes:

Manual Control The program waits for the instructions above described , which are introduced through the keyboard, one at a time.

Computer Control The program reads a sequence of orders from an input file which was previously written with the different orders for the whole night, and the time at which they must be executed. The program goes through them sequentially until the stop instruction is received. Then, all heliostats are sent to *rest* position.

The second major mode is the usual way in which observation is done. The different instructions to be carried out during a night are introduced into an input file and executed automatically by the program at the predefined time. The input file is usually modified once per month, at the start of the observation shift. This procedure avoids human errors at observation time, and, as we will see, allows for remote operation.

Another requisite that arises at the steering of the heliostats is the constant need to correct for the disorders in the mechanics of the heliostat mountings that occur due to the constant wear out of the step motors and moving pieces. Otherwise, when given the same order of movement in motor steps the reflected image would not lay at the desired spot in the tower. This is corrected with the introduction of *offsets*. These values are routinely calculated by the PSA staff and kept in a data-file with info for all the heliostats.

The determination of these offsets was originally done with the main CESA-1 control computer, but lately and due to some problems with the main computer, our group developed a new application for this task. A new program running on a Windows computer was developed. The procedure consists on aiming one heliostat so that the image of the Sun reflects on a target at the central tower. The image can be seen in a monitor with an over-imposed grid. If the image is not centered on the grid, the offsets in both azimuth and zenith axes can be increased or decreased with a simple key-press, in increments of one motor step. When the image looks centered to the eye the new offsets are stored into the heliostat's data-file for later use by the control program. The procedure relays on the experienced eye of the operator, and though it may seem quite rude the precision attained is quite high, coming to the minimum possible of 1 motor step (0.044 degrees).

Along with the offset, the heliostat's data-file also keeps information on the coordinates, communication line number and focusing point for that heliostat. The exact coordinates of the focusing points is kept in a separate file, where several different focuses can be defined.

As an output, the program produces a file with the aiming coordinates of each heliostat every 3 seconds.

The **quality** of the image formed by one heliostat is determined by several factors, among them the most important ones are:

- the precision in the shape of the mirrors,
- the difference between the focal length of the facets and the real distance from the facet to the place where the image is formed,
- the possible imperfections in the *canting* of the different facets of the heliostat,
- the errors in the tracking due to the quantification of the steer movement of the heliostats in motor steps,
- the off-axis angle at which the source is usually located with respect to the optical axis of the heliostat, which introduces astigmatic errors.

The quality of the light-beam reflected by the heliostats was previously measured by the HELIOS experiment, via analysis of the reflected images of the Sun at the tower, and determined to be of about 0.21 degrees, taking all errors into account [4]. Of course this value for individual heliostats depends on the distance from the heliostat to the tower and the off-axis angle at which the Sun is, but 0.21 degrees can be taken as a good mean value for most observing configurations. This means the heliostats array has a limited imaging capability for objects about 0.6 degrees diameter (the typical size of the Sun, and also a typical size for EAS's).

Finally, an unforeseen problem arose during the first observation nights when **dew** appeared on the heliostats, barring any good observation. This problem originates in the fact, that though rain at the PSA is very seldom, with very few rainy days per year, the Mediterranean Sea is not very far away. In the heat of the day a large amount of water is evaporated into the atmosphere and in the night brought by the wind inland and, due to the temperature difference, it condenses. This was a major problem as many of the best observation nights were ruined by this cause, until we started to use an anti-dew product in January 2000. The product employed does not avoid water condensation, but it does modify the surface tension in such a way that dew droplets are not formed, keeping mirror reflectivity high enough for observation. This product is sprayed over all the GRAAL heliostats every second day in observation periods.

2.2.3 The Winston cones

As already mentioned, in GRAAL a single PMT detects light reflected by a group of heliostats. In order to limit the field of view of the PMT and to provide the appropriate aperture size (around 1 meter) each tube is coupled to a light concentrator. The chosen shape of this concentrator is that of a truncated Winston Cone [5]. The number of installed cones is four, each one aiming at a certain point on the ground so each cone collects light from a different group of heliostats, determined by its field of view (see figure 2.5).

The **size of the Winston Cones** was determined by the dimensions of the reflected image of an EAS at the Cone's plane and the intended field of view of 10 degrees, necessary to collect light from a group of heliostats. Due to the large focal lengths of the mirrors, the image at the tower produced by an object of approximately 0.6 degrees diameter (the size of a typical EAS) is about 1 meter diameter. Therefore the size of the outer opening of the Winston Cones was chosen to be 1.2 meters, while the rear part (where the PMT is attached) is determined by the size of the PMT to just 20 cm diameter. With these dimensions fixed, the total length was determined to be 2 meters.

The location of these Winston Cones is a specially-built **hut** at the 70-meter level in the central tower (figure 2.3). Physically, the hut is attached to the outside wall of the tower. Inside the hut a structure holds the cones in place aiming at specific points on the ground. The hut has a remote-controlled automatic door that is opened every night for operation and closed at the end of the night to protect the cones from weather conditions and sunlight reflected by heliostats.

The **Cones were built** at the workshops of the Max-Plank-Institut in Munich. The process started by building a wooden mold with the calculated shape. Then aluminized mylar foil was put on the mold and afterward mats saturated with epoxy resin were put on the foil. After drying the mold could be removed, and a Winston Cone with a mirrored interior resulted.

The characteristics of the Winston Cones were determined experimentally:

Fraction of light reaching the PMT The fraction of light reaching the PMT, out of all the incident light to the Cone's opening, was measured

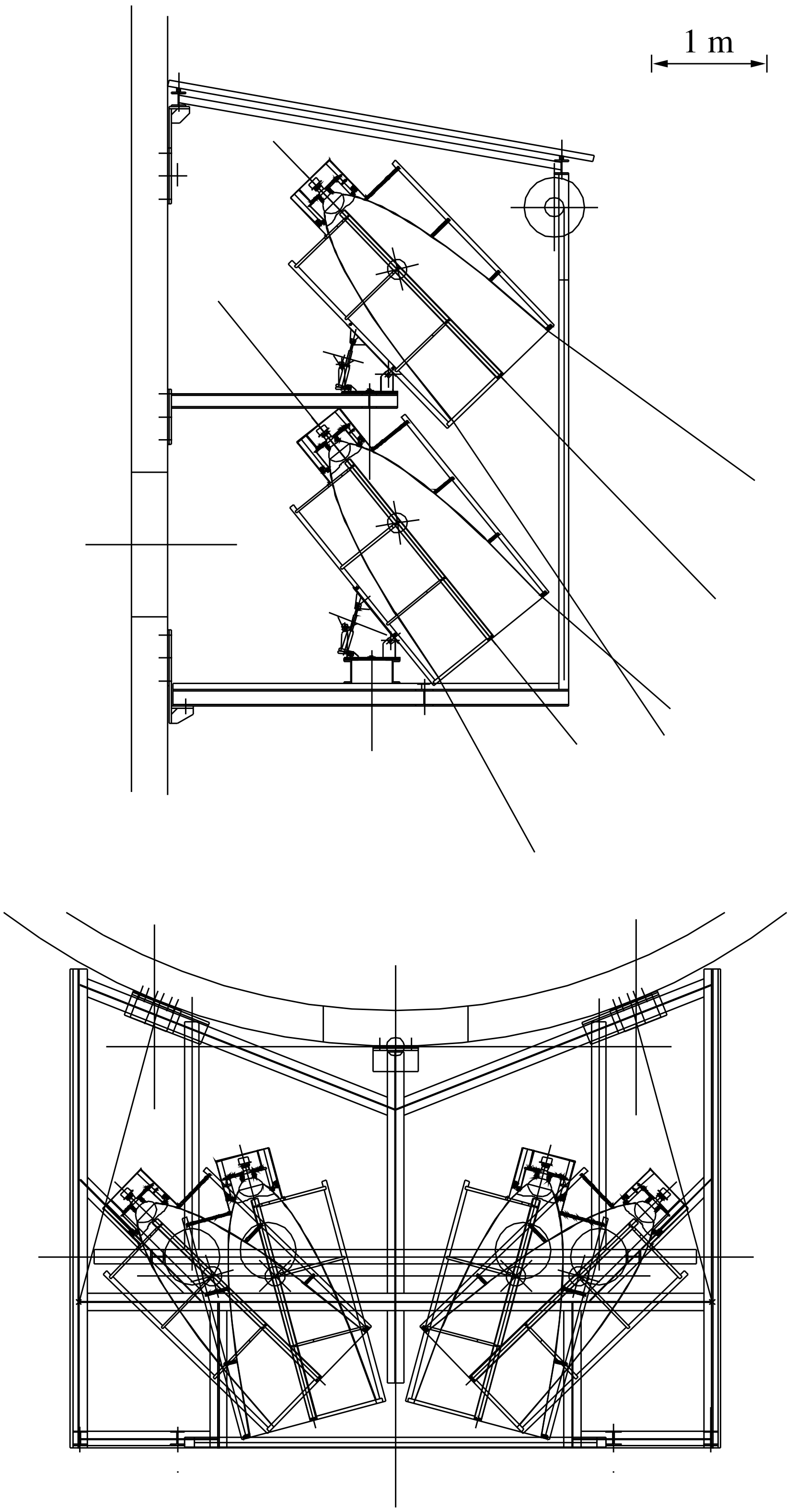

Figure 2.3: *The specially built hut is attached to the tower at the 70-meters level. The structure inside holds the four Winston Cones in position aiming at specific points on the ground.*

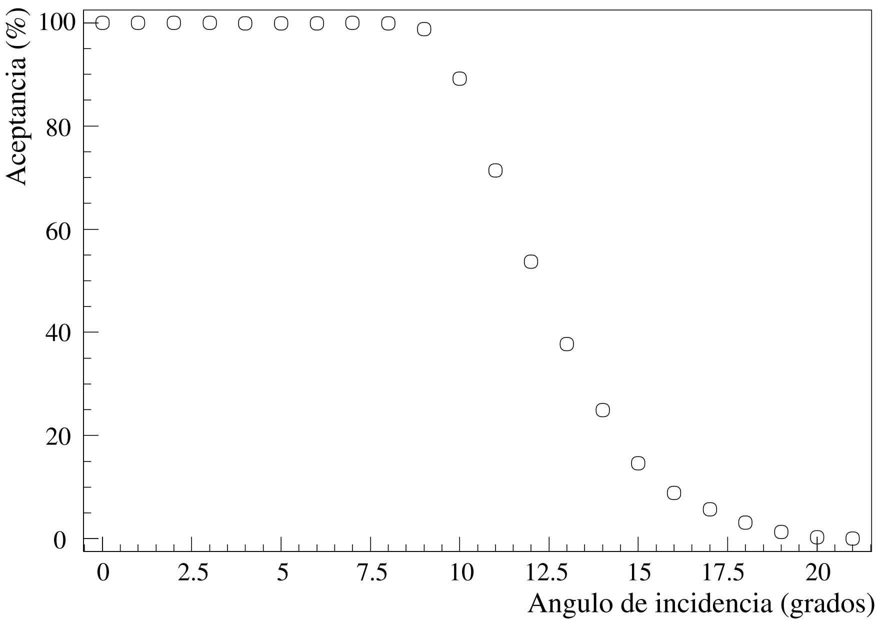

Figure 2.4: *The experimental measurement of the angular acceptance of the Winston Cones shows that the acceptance is nearly 100% for on-axis incidence and up to 10 degrees, where it falls rapidly down to zero.*

in the following way: The pulse height P of a fast Light Emission Diode (LED) with a FWHM of about 4 ns and maximum emission at about 440 nm, was measured with and without a diaphragm that stops all the light except the one that directly hits the PMT (no reflections on the mylar foil). The LED was situated as far as possible from the Winston Cone so photon incidence was almost parallel to the optical axis. In this case light collection efficiency E can be given as:

$$E = \frac{P_{without\,diaphragm}}{P_{with\,diaphragm}} \left(\frac{R_d}{R_c}\right)^2 = \varepsilon^{n_r}$$

where R_d and R_c are the radii of the diaphragm and the Winston cone respectively, n_r is the mean number of reflections until a photon hits the PMT (calculated with a Monte Carlo simulation to be 1.36) and ε is the reflectivity of the aluminized Mylar foil at 440 nm, which is $\gtrsim 92\%$ over a wide wavelength range. After correcting for the radii factor, the measurements yield an experimental value for the collection efficiency of $E = 0.89 \pm 0.04$ which exactly matches the theoretical value of 0.89 ($= 0.92^{1.36}$), confirming the good optical quality of the manufactured Winston cones.

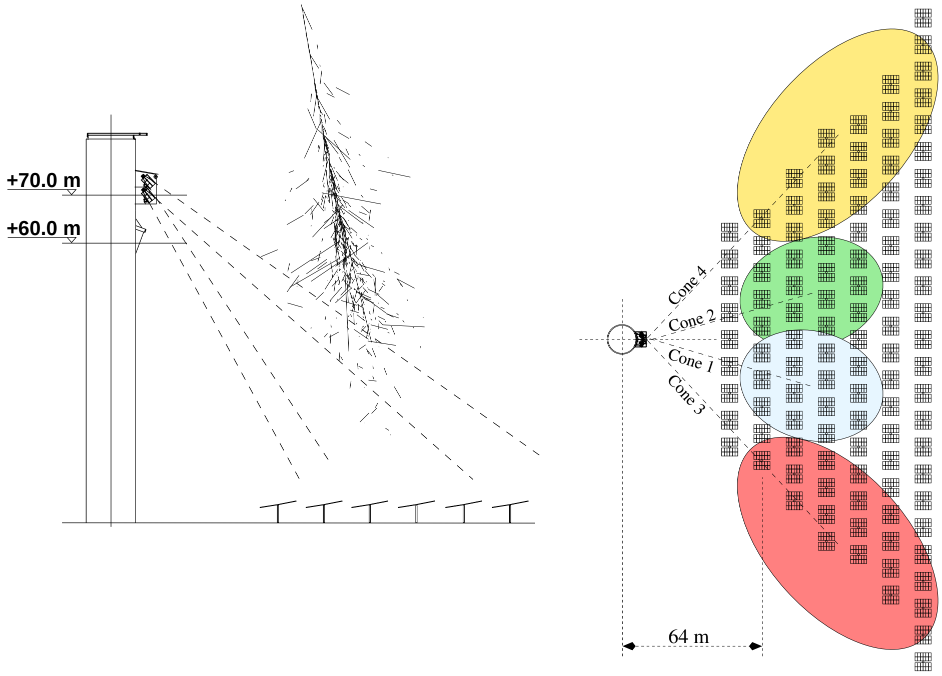

Figure 2.5: *Schematic view of the detection system. The Winston Cones at the 70 meter level see the Čerenkov light produced by an extensive air shower generated by a cosmic γ-ray, and reflected by the heliostats (left). On the right a projection of the fields of view of the four PMT's on the ground can be appreciated. Only light reflected by heliostats inside the colored regions will be detected by the corresponding PMT.*

Efficiency with incident angle The efficiency of the Winston Cone depends on the incident angle of the light with respect to the axis of the cone. This efficiency was measured, obtaining the curve shown in figure 2.4. This shape matches very well Monte Carlo simulations up to 10 degrees, where the experimental cone has a smoother shape than expected.

The field of view defined by the Winston Cones will determine which heliostats will be seen by the PMT when the cone axis is aimed at a certain point on the ground. The chosen aiming points were symmetric to the north-south axis with two cones collecting light from the nearest heliostats (each cone with 13 and 14 heliostats respectively) and another two cones collecting light from heliostats farther away and to the east-west sides of the array (with 18 heliostats each). See figure 2.5. The total number of heliostats in use is 63.

A major feature of the detector is its **field of view**, which is determined

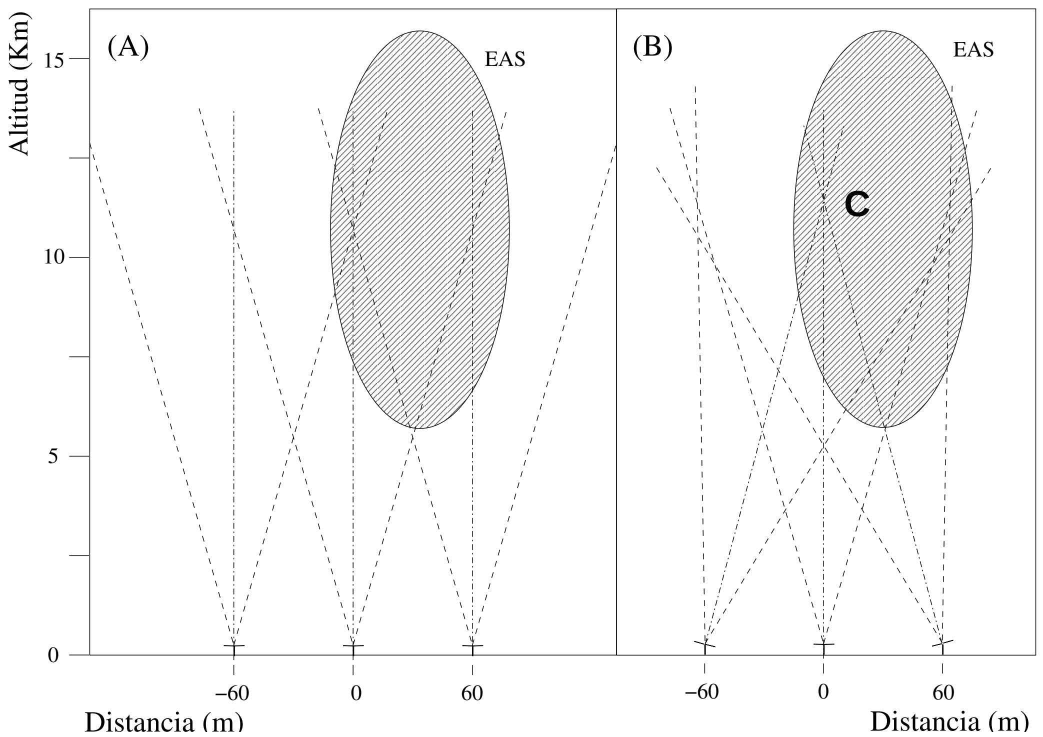

Figure 2.6: *(A) In* parallel view *all the heliostats are aiming at the source, and due to the limited field of view, the EAS is not detected by all of them. (B) In* convergent view *all the heliostats are aiming at the same point in the atmosphere (C), toward the observed source. Showers crossing near the aiming point are detected by all heliostats.*

mainly by the size of the opening of the cones and the distance from the cones to the heliostats, and thus depends on the heliostat–cone pair. Assuming a mean distance of 110 m, and knowing that the cone's outer opening is 1.2 m diameter we can roughly infer a mean solid angle of $9 \cdot 10^{-5}$ sr or a field of view of approximately 0.6 degrees.

This number is rather small if compared to the usual values of imaging air-Čerenkov telescopes (about 3 degrees). Though this field of view roughly matches the angular size of EAS's, Čerenkov-light cannot be simultaneously detected by all the heliostats, if all of them are aiming to the celestial source, in the so-called parallel view (see figure 2.6.

This is a critical problem for all the experiments that employ a solar plant for gamma-ray astronomy, as many of the heliostats are not going to contribute to the signal while still contributing to the noise background, therefore reducing the signal to noise ratio of the experiment.

As already shown by other groups [6], a solution to this problem consists

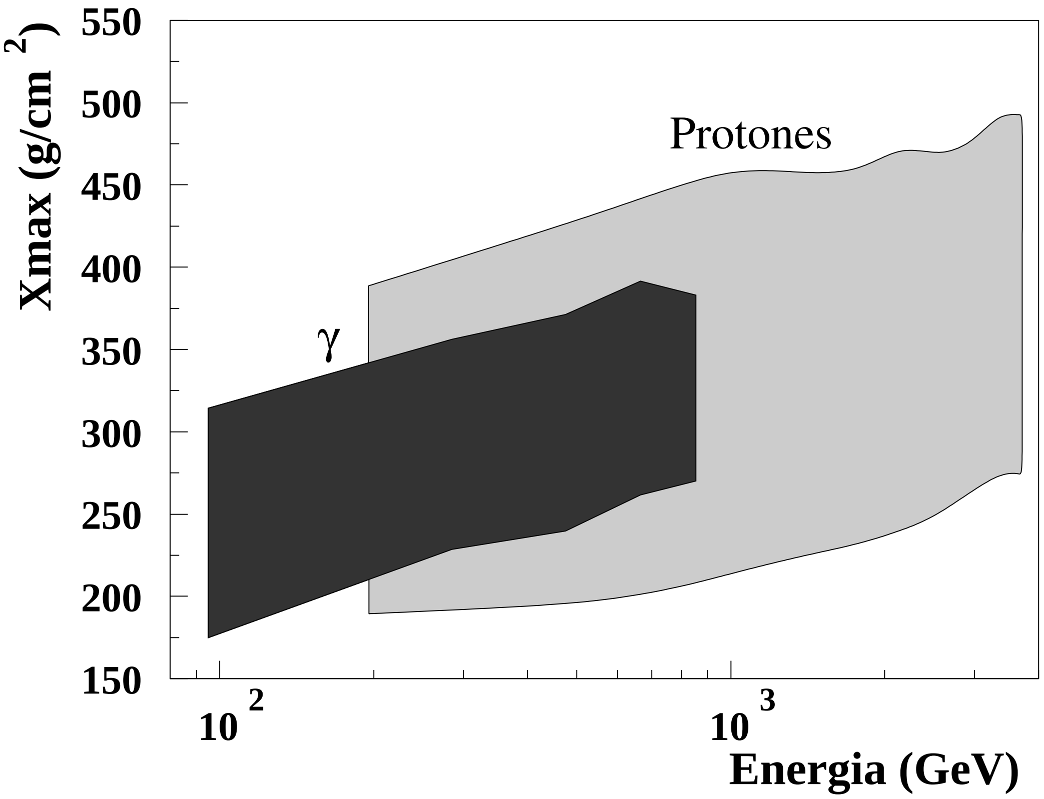

Figure 2.7: *Mean depth at which the maximum development of showers takes place, X_{max}, as a function of the energy of the primary. Error bands correspond to the width of the X_{max} distribution ($\overline{X_{max}} \pm \sigma$).*

in using the technique called **convergent view**. This technique is schematized in figure 2.6. Instead of pointing all the heliostats in the same direction (*parallel view*), they are pointed to the place in the atmosphere where the maximum of the EAS's is expected to take place. The main advantage of this technique is that in the case where the maximum of the shower takes place somewhere near the observed point, most of the heliostats are going to receive some light, allowing for a lower energy threshold of the detector. The major drawback is the fact that the effective area of the whole experiment is reduced because showers generating far away from the observed point will not be detected at all, lowering the sensitivity of the detector.

The atmospheric depth at which the convergent point is located, is determined via Monte Carlo simulations of EAS development. From the analysis of the simulated showers the mean atmospheric depth at which the maximum takes place can be plotted as a function of the energy and type of primary (figure 2.7). From that plot we can choose the **observation depth** for our experiment. At present this value is set to 230 gr/cm^2, as we intend to detect EAS's initiated by gamma-rays with energies below 200 GeV. The convergent point in Cartesian coordinates is calculated with simple formulae:

$$\begin{aligned}
\Pi &= d \cdot \cos(Z) \\
\text{If } \Pi < 230 \Rightarrow h &= (44.34 - 11.86 \cdot \Pi^{0.19}) \cdot 10^3\,\mathrm{m} \\
\text{If } \Pi \geq 230 \Rightarrow h &= (45.5 - 6.34 \cdot \log(\Pi)) \cdot 10^3\,\mathrm{m} \\
D &= \frac{h}{\cos(Z)} \\
x &= -\cos(A) \cdot \sin(Z) \cdot D \\
y &= -\sin(A) \cdot \cos(Z) \cdot D \\
z &= \cos(Z) \cdot D
\end{aligned}$$

where d is the observation depth in gr/cm^2, D the distance from the coordinate origin to the convergence point, and Z and A are the observation zenith and azimuth respectively. The simple formulae in the estimation of D are precise enough, taken into account the expected fluctuation in the shower maximum position.

The advantage of convergent view as compared to parallel view is an increase in both the number of heliostats that reflect Čerenkov light into the cones and the mean number of p.e. collected from each heliostat. Monte Carlo simulations show increments of ~60% in the number of heliostats and ~20% in the number of photons.

2.2.4 The Photo-multiplier Tubes

Due to the large reflecting area, background noise at the PMT's is very high. Therefore the model 9352KB manufactured by EMI for high-background-noise working conditions was chosen. It is a large 8-inch hemispherical photo-multiplier tube (PMT) with just 6 amplifying stages. This model has a sensitive bialkali photocathode with a peak quantum efficiency (QE) of 30% at 350 nm, falling down to 20% at 300 and 490 nm, as shown in figure 2.8.

The running voltages have been chosen in such a way that single-peak accidental trigger rates are similar in the four cones. According to the information provided by the manufacturer, the direct-current gains obtained at these voltages are expected to be:

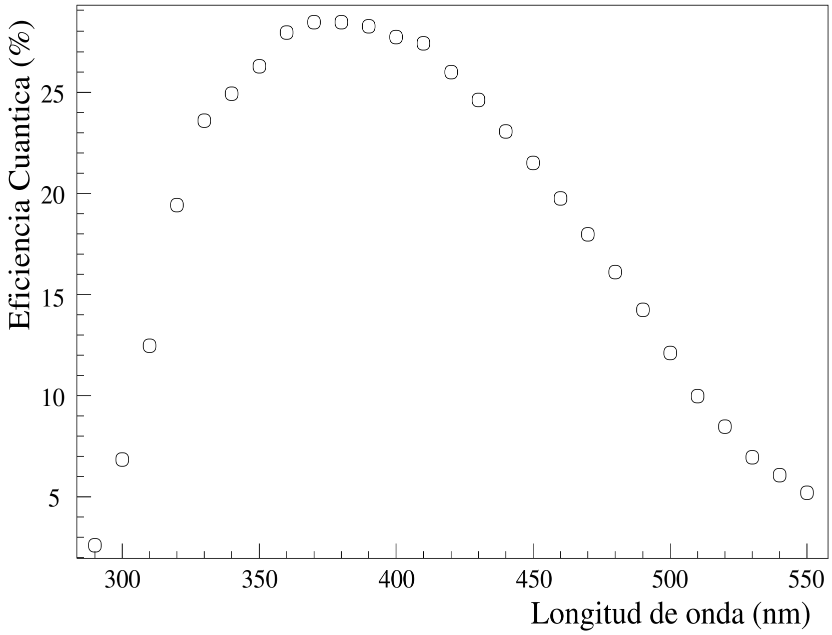

!

Figure 2.8: *Photocathode quantum efficiency versus wavelength. The peak take place at 370 nm.*

	HV (V)	Gain
Cone 1	1400.	$1.8 \pm 0.9 \cdot 10^4$
Cone 2	1400.	$1.4 \pm 0.7 \cdot 10^4$
Cone 3	1500.	$1.9 \pm 1.0 \cdot 10^4$
Cone 4	1250.	$1.0 \pm 0.5 \cdot 10^4$

With these values, background currents due to the Night Sky Background (NSB) of the order of 10-15 μA are usual.

As already mentioned the gains given in these table are valid for direct current. The gain for fast pulses may differ from these values, and will have to be fitted more precisely with a comparison between the simulation results and the real data.

2.2.5 Electronics

The electronics are divided in three main sections: the amplification phase, the trigger logic and data storage.

The whole setup is controlled by a PC (Penthium II) through a CAMAC module, and the data are read from an oscilloscope via a GPIB card.

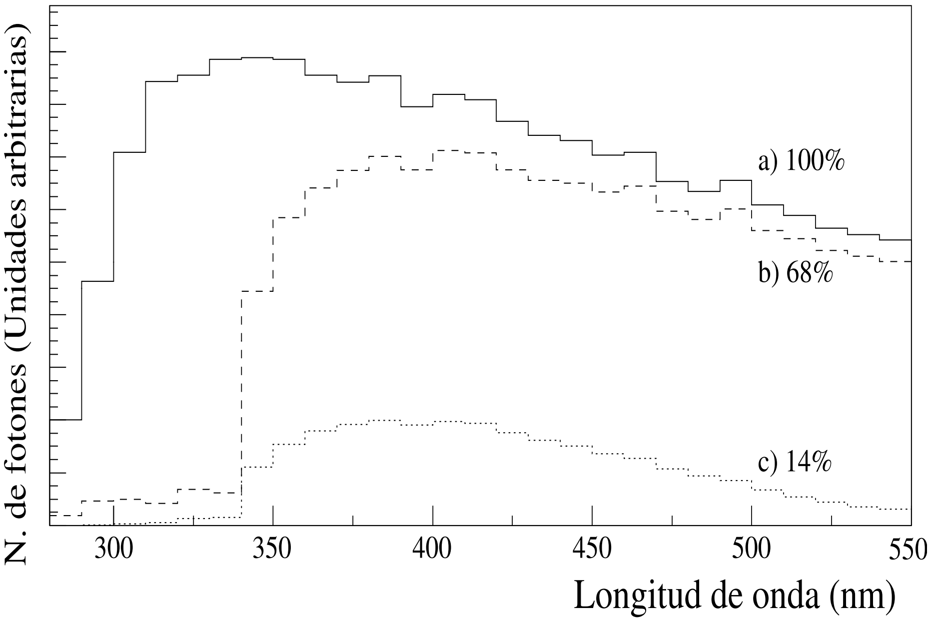

Figure 2.9: *Air-Čerenkov-light spectrum. a) Original spectrum incident on the mirrors. b) Spectrum after reflection on the heliostats. c) Spectrum as detected by the PMT. The overall fraction of photons detected is around 14%. Y-axis is normalized to the maximum of the original spectrum.*

2.2.5.1 Signal amplification

Due to the large NSB, the PMT's have to be operated at low gains. Immediately after the PMT there is one amplifier, and a second one at the end of the transmission cable to the electronics rack. These amplifiers provide a non-linear gain, such that bigger pulses are more amplified than smaller ones.

The time characteristics of these amplifiers with a rise time < 1 ns and a low frequency cutoff of 20 MHz allow for the transmission of Čerenkov pulses without any information loss.

After being amplified the signal is distributed with a power divider (see figure 2.10) and sent both to the trigger logics and the analog readout (via the oscilloscope).

Two systems have been used for the gain **calibration** of the whole electronic set-up.

The first one consists on a calibrated Light Emission Diode (LED) attached to the outer opening of each Winston cone. These LED's emit light pulses (FWHM$\approx$ 6 ns) when triggered by the electronics. Such pulses are

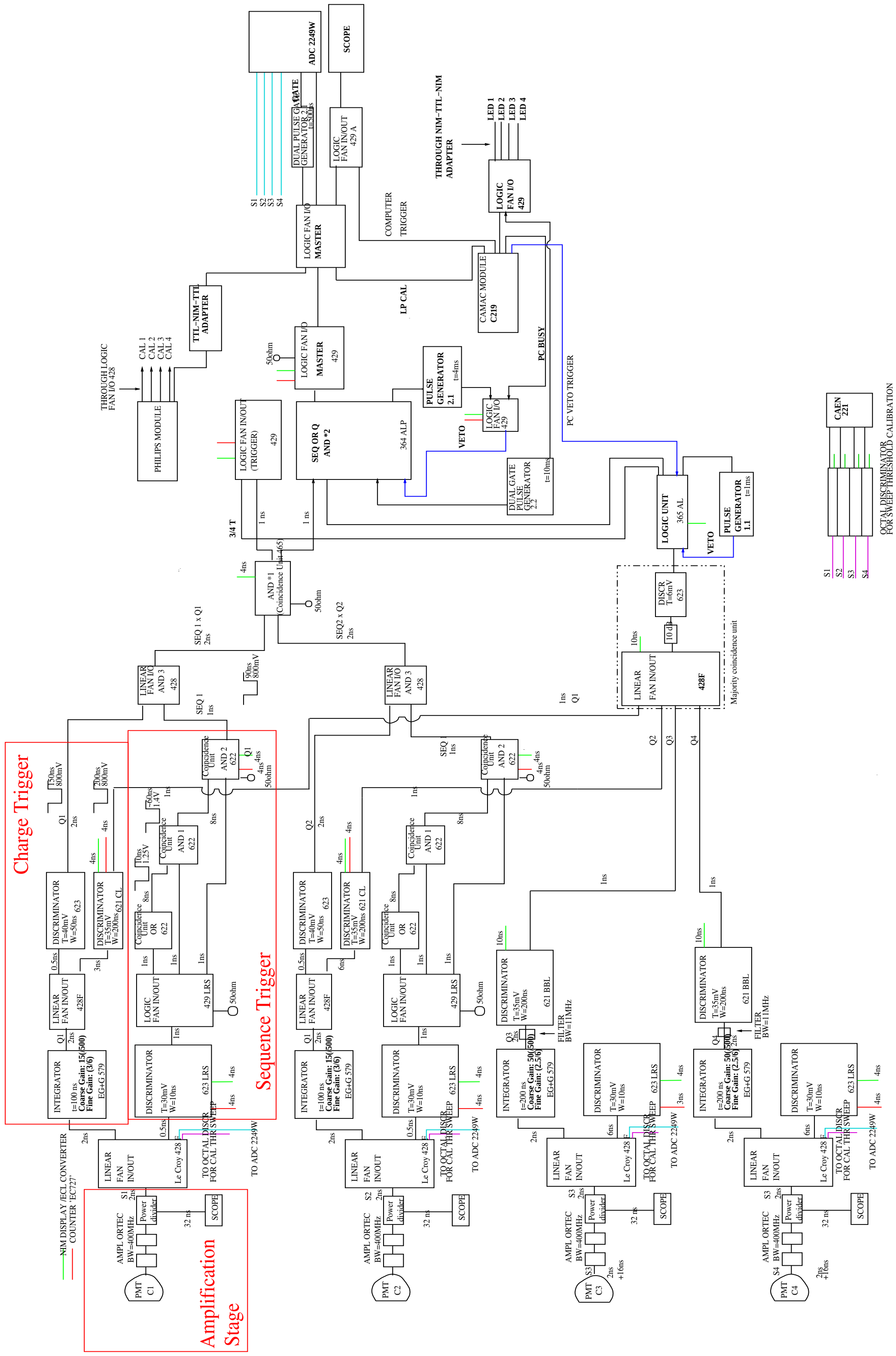

Figure 2.10: *A scheme of the electronics of GRAAL. See the text for a description of the different components.*

collected by the PMT's and recorded for calibration purposes.

Apart from being used to check whether conditions in the electronics remain stable during a night and compare conditions among several nights, these LED's can be used to obtain an absolute conversion value from a light pulse incident on the photocathode to the peak voltage measured by the electronics. The following table shows the results obtained with this method:

	LED pulse (photons)	Peak voltage (mV)
Cone 1	829	146±5
Cone 2	690	167±5
Cone 3	624	179±5
Cone 4	581	103±4

Unfortunately the use of these values for a very precise calibration of the electronics is limited. Apart from the great uncertainty in the values of the measured voltage peaks, the efficiency of the photocathode is highly dependent on the position of the LED at the entrance of the cone. Therefore there is an uncertainty in the number of photoelectrons that contribute to the measured pulse. These values can be used as good estimators of the gain curve as we will see in §3.1.2, but cannot be used to provide an accurate absolute calibration.

A second subsystem involves a Phillips pulse generator (FWHM $\approx 7\,\mathrm{ns}$). Pulses generated by this module are injected just after the PMT and before the first amplifier, so they provide us with information about the electronic chain after the PMT's. The injected charge can be modified and in this way we can obtain the non-linear gain curve of the amplifiers as a function of the injected charge. Analyzing data from the Phillips calibration we obtain the plot in figure 2.11 which represents the output maximum voltage of the peak versus the input charge. This curve can be parametrized as a second grade polynomial $V = A \cdot C^2 + B \cdot C$, where V is the output voltage in mV and C is the input charge in pC. Fitting the plot obtained in each cone to such a function yields the following results:

	Cone 1	Cone 2	Cone 3	Cone 4
$A\,(\mathrm{mV/pC^2})$	0.136±0.022	0.137±0.027	0.122±0.022	0.128±0.025
$B\,(\mathrm{mV/pC})$	2.9±0.9	3.5±1.2	2.8±1.0	2.5±1.1

The non-linear gain curves obtained here will be employed in the simulation of the electronics (see §3.1.2).

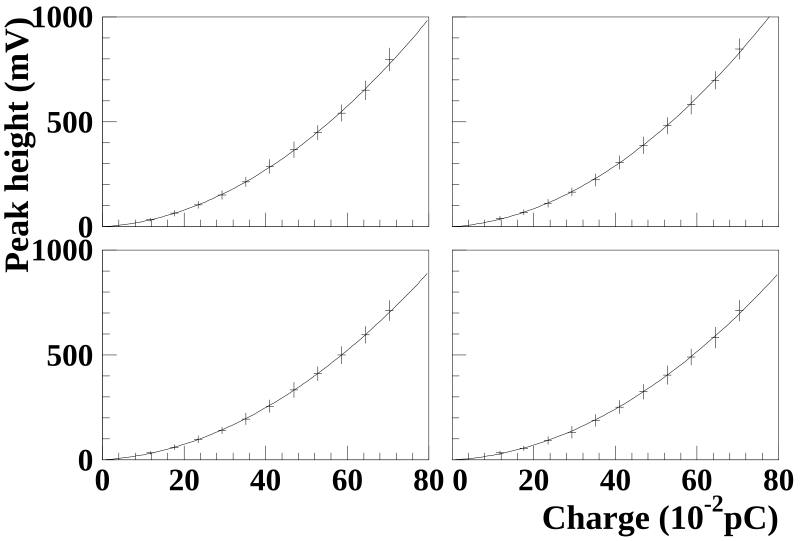

Figure 2.11: *Relative non-linear gain curve as obtained from the Phillips pulser. The maximum peak height for different charge inputs is shown.*

2.2.5.2 The trigger logic

The trigger logic is determined by the features of the expected signals from γ-ray showers. For an easier visualization, we can assimilate the Čerenkov front, with a slightly spherical shape (see §4.3), to a plane moving along the observed direction. The arrival time of the front to each heliostat and the distance heliostat–Winston Cone is different for each heliostat. Therefore, in each PMT, instead of a single pulse with light contributed by all heliostats, many smaller pulses, each from one heliostat, arriving at different times are observed. We get a *train of pulses* with the different signals separated by intervals of a few nanoseconds. The exact structure of this train of pulses depends on the observed direction, as the time delays among heliostats depends on the incoming direction of the shower (see figure 2.12). The shape of the Čerenkov front also modifies this structure, though this is a second order effect. However, since heliostats are located on a regular spatial pattern, it is not unusual for pulses from different heliostats to arrive at the same time, overlapping. In figure 2.13 the pulse-train in a cone associated to a shower incoming from a typical direction is shown, along with the theoretical arrival times of the different heliostats.

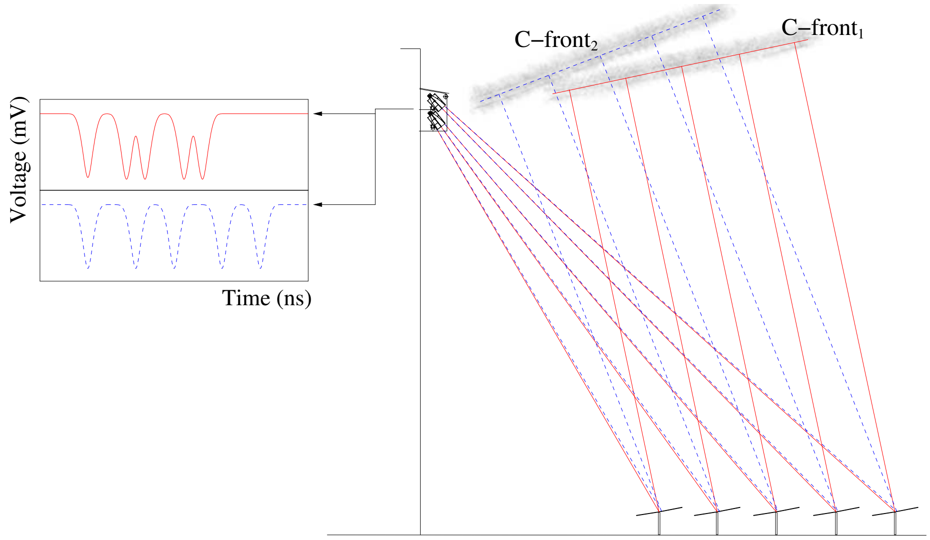

Figure 2.12: *The different heliostat-cone distances produce a signal time pattern that depends only on the spatial distribution of the heliostats on the ground with respect to the Winston Cone positions. But the detected pattern changes for showers coming with different incidence angles, as the delays among heliostats are modified. The signal pattern is very dependent on both the Azimuth and Zenith angles.*

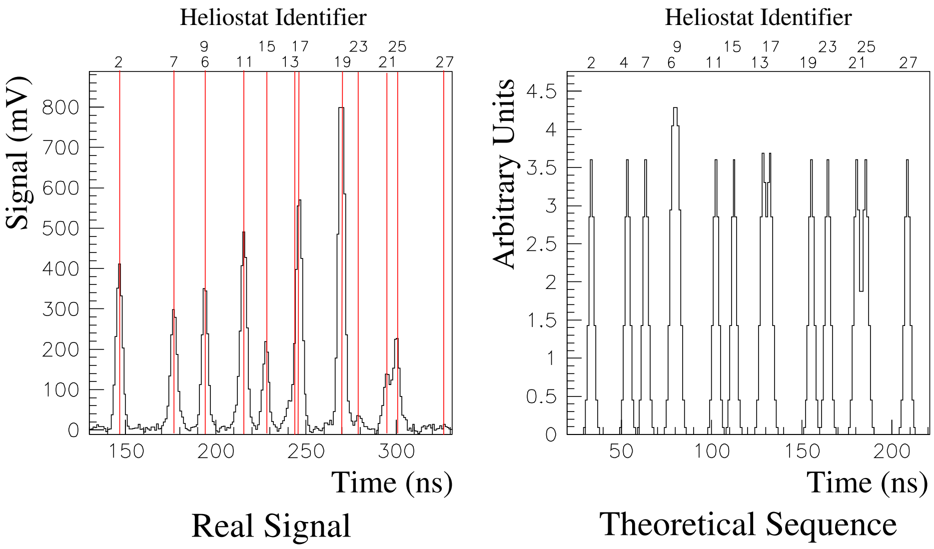

Figure 2.13: *The pulse train structure detected in a cone for a typical incidence direction is shown. The picture on the left is a real shower, and the picture on the right shows the theoretically-predicted arrival times for the different pulses coming from the heliostats. Each heliostat has been numbered with a reference identifier.*

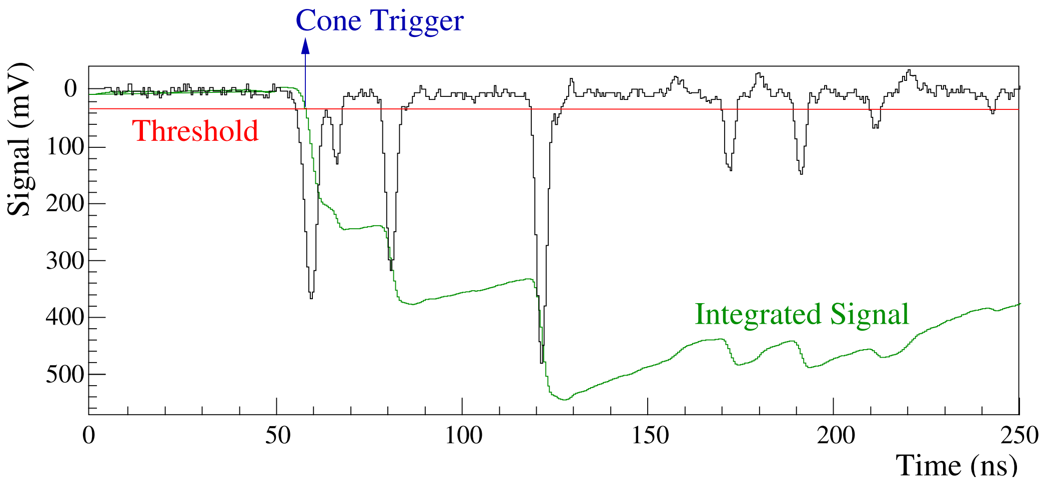

Figure 2.14: *In this simulation of the* **charge trigger** *logic, it can be appreciated how the integrator module works on the detected signal. When the integrated signal passes the threshold a trigger for the cone is given.*

It is important to note that the time structure is specific of the incoming direction of the shower. The accuracy of the pointing of the heliostats will influence on the amount of light collected, but it will not change the time structure of the shower (apart from the intensity of the pulses). This will allow for a reconstruction of the incoming direction of the shower despite a possible pointing inaccuracy, as we will see in §5.2.5.

Accounting for the fact that roughly all the pulses coming from an EAS arrive at the PMT's within a time interval of about 100 ns (200 ns) in cones 1–2 (3–4), we have devised a very simple trigger that integrates the total charge with a time constant of the order of the length of the pulse train. We call this trigger **charge trigger** or **Q-trigger** for short. The integrated signal is expected to surpass significantly the NSB fluctuations when a shower arrives at the heliostat field.

The electronic setup of this trigger is rather simple, as can be seen in figure 2.10. The signal of each cone goes through an integrator module (EG+G 579) which behaves like an amplification with a time constant of 100 ns (200 ns) for cones 1–2 (3–4). The resulting signal is tested by a discriminator with a threshold of 35 mV (see figure 2.14), which in case of being triggered generates a signal 200 ns long for coincidence with the other cones. To generate a total trigger a majority coincidence is required (three out of the four cones must trigger within the coincidence periods).

Signal parameters			Cone 1	Cone 2	Cone 3	Cone 4
Input Signal	Maximum	mV	250	290	260	250
	rise time	ns	6	6	6	6
	fall time	ns	12	12	12	12
	FWHM	ns	7	7	7	7
Output Signal	Maximum	mV	145	160	260	260
	rise time	ns	24	24	75	75
	fall time	ns	580	580	750	750
	FWHM	ns	98	98	160	160
	$1/e$ fall time	ns	104	104	200	200

Table 2.1: *Parameters of the integrator modules of the* charge trigger*.*

The response of the integrator to an input fast pulse has been measured. The values obtained in the four cones are shown in table 2.1.

Apart from this simple trigger, we could think of a more complicated one, which makes use of the time structure of the signal. The ideal trigger should demand peaks at the precise time where light from one or more heliostats is expected. Unfortunately it is extremely difficult to accomplish such a condition with a hardware trigger since the peak sequence depends on the incoming direction, and, in addition, usually a significant fraction of the peaks is missing (i.e. they are less intense than the fluctuations of the NSB). As a compromise, taking into account that the time structure shows a recursive pattern due to the spatial structure of the heliostats, with peaks located at intervals of 15–35 ns, we can devise a method to look only at certain points in the trace, where the probability of arrival of a pulse is higher. As the pattern depends on the source's altazimuth coordinates, it should change over time, leading to very complicated electronics with delays that change with time, depending on the coordinates of the observed source. Therefore a further simplification was made, calculating a *mean pattern* for the most usual observing directions, in order to set the delays and lengths of the search zones (what we call *search windows*). The result is what we call the **sequence trigger**, which can be schematized in figure 2.15: the signal is analyzed by a discriminator for a pulse higher than 30 mV. Once we have such a peak (the first peak), after a delay of 20 ns, the signal is tried again by the discriminator for 40 ns. If inside this *time window* of 40 ns a new peak higher than 30 mV is received (the second peak), the procedure is repeated. After a delay of 20 ns the signal is tested for 40 ns, looking for a third peak. If the third peak is detected a trigger for that cone is given, generating a

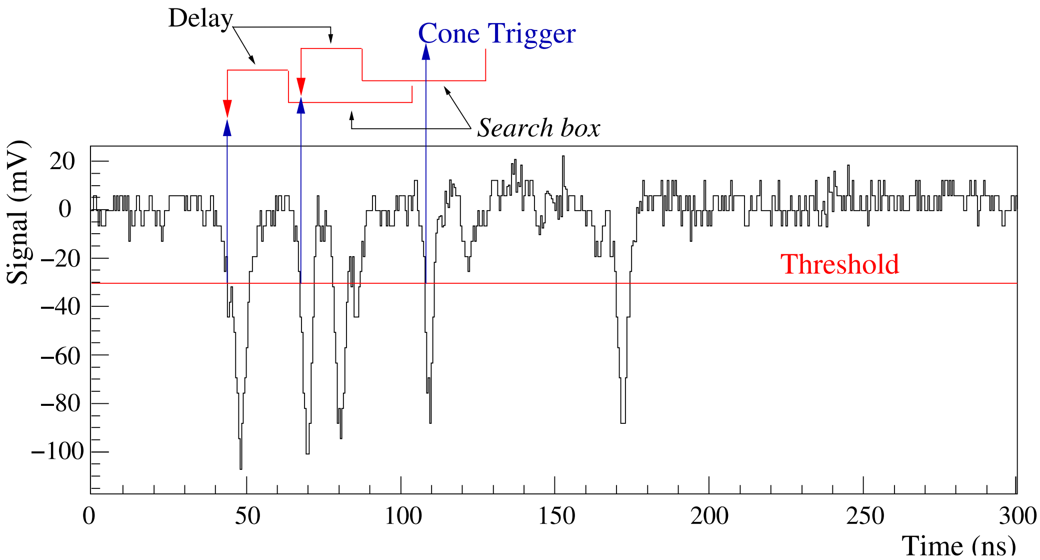

Figure 2.15: *A scheme of the* **sequence trigger** *logic can be appreciated in this plot. The signal is analyzed looking for a pattern of peaks at regular intervals. In case 3 such peaks are found a trigger for the cone is given. At present the delays are set to 20 ns and the* search box *to 40 ns.*

signal 100 ns long for coincidence with other cones.

Due to its complexity, this trigger is applied only to cones 1 and 2, while cones 3 and 4 are triggered only by the charge trigger. In order to have a total trigger both cones 1 and 2 must trigger within the coincidence times (100 ns).

2.2.5.3 Limits of the trigger logics

After correcting for the different light collection efficiency of the heliostats-cones setup for the different observation directions, the trigger efficiency still depends on the incoming direction of the cosmic-ray due to the structure of the train of pulses. This is specially true for the sequence trigger applied on cones 1 and 2, which requires a certain pulse structure.

The pattern produced by cosmic rays with certain incoming direction may help the fulfillment of the trigger condition, whereas patterns generated in other incoming directions may make it impossible for the condition to be fulfilled. In figure 2.16 we show the number of possible sequences (normalized to the maximum) that fulfill the sequence trigger condition, as a function of the azimuth and elevation of the observed source.For each observed direction, the expected pattern for a cosmic ray was generated, calculating the number of possible sequences that could take place in that pattern. Normalizing this

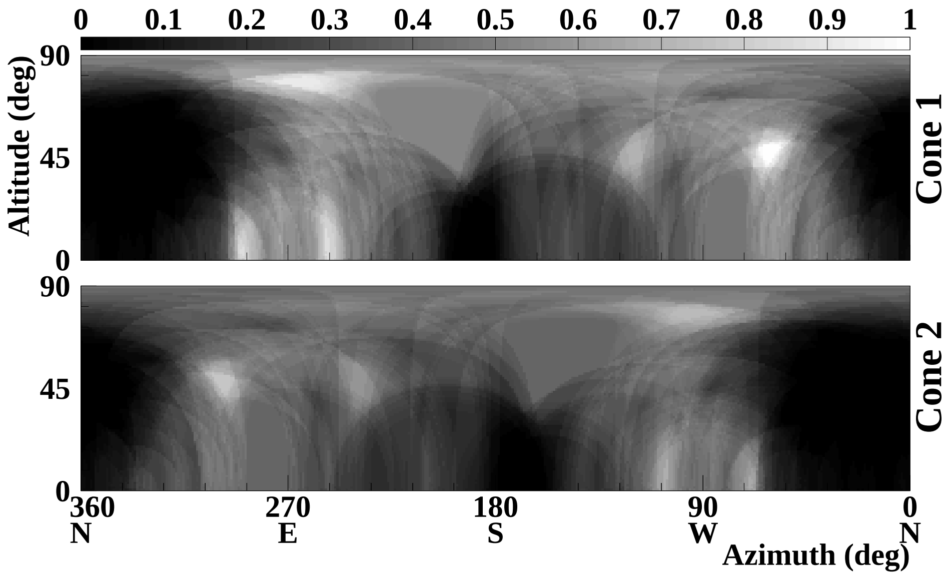

Figure 2.16: *Normalized number of possible sequence triggers (described in the text) as a function of the azimuth and elevation of the incident cosmic ray.*

number to the absolute maximum for all directions, we can generate a picture of the sky with the zones where the probability of having sequence trigger is lower or greater depending only on the structure of the pulse sequence and the trigger condition. It can be appreciated that observation toward the North, at elevations lower than 80 degrees will be almost impossible with the present sequence trigger, as the number of possible triggers is very low (for some directions it is impossible to fulfill the required condition). The same is true for observation toward the South at very low elevation. On the other hand there are certain observing directions where there are many possible sequences that may fulfill the trigger condition, marked in the plots with the lighter colors. Observation of cosmic rays with this incoming directions will produce larger rates due only to the generated sequence and the trigger condition. This fact indicates that the efficiency of the sequence trigger at use in the experiment depends greatly on the observed direction.

A similar picture can be generated for the charge trigger. In this case the trigger condition checks for charge fluctuations within the integrator time constant. Therefore the maximum efficiency of the trigger is obtained when the length of the generated pulse train is similar to the integrator time constant. In figure 2.17 the theoretical length of the pulse train for each incoming direction is plotted, along with the contour line for a value similar to the integrator time constant. Efficiency will be highest for observing directions near that line. It can be appreciated that toward North, all the pulses tend to be very close together, concentrating in a single peak for certain incoming directions which depend on the cone (due to the different geometrical configuration of each cone and its heliostat field). For southern incoming directions and at very low elevation the pulse train tends to be very long which also reduces the efficiency of the trigger. In general we can say that the chosen time constants are good for observation at high altitudes.

Due to the large dependence of the sequence trigger with the observed direction, it is used only as a secondary trigger system, with the charge trigger being the main one.

2.2.5.4 Data acquisition

As already mentioned in §2.2.5.1, after the amplifiers the signal is divided, and one of the branches takes it to the data acquisition section of the electronic.

To take full advantage of the very fast electronics employed in the transmission of the signal, we register all four pulse trains in one digital oscilloscope (LeCroy 564A) with a bandwidth of 1GHz and a time bin of 0.5 ns. In this way we are sure that the typical FWHM of the detected peaks (typically of 3.5 ns) is due only to shower properties, geometrical effects in the mirror and PMT properties, and not to effects in the transmission and record of the signal.

The oscilloscope is read out via a GPIB interface in a CAMAC crate to a PC (Penthium II). For each cone a trace of 1 μs length is read out, with a 0.5 ns time binning resolution and 1 byte per bin, for a total 8 Kbytes per event. The transfer rate reaches 130 traces per second. This means that for a master trigger rate of 5 Hz (upper limit fro the present configuration) dead time losses are around 15%. Using one byte per time bin means that our amplitude resolution is just 256 channels. This is a restriction if we intend to measure small and big pulses at the same time. Saturation is quite frequent for very intense showers. At present the maximum peak height that can be measured before saturation is 1.6 V. There are plans in the near future to add another oscilloscope which will record large showers.

Finally the data is stored in the hard disk of a PC and later transferred to magnetic tape. Not only are the traces with the signal stored, but also many data given by the electronics: the high voltages of the PMT's; currents at the different cones; single peak trigger rates; weather variables, humidity, wind-speed and pressure, and also data from the heliostat control program about the movement of the heliostats..

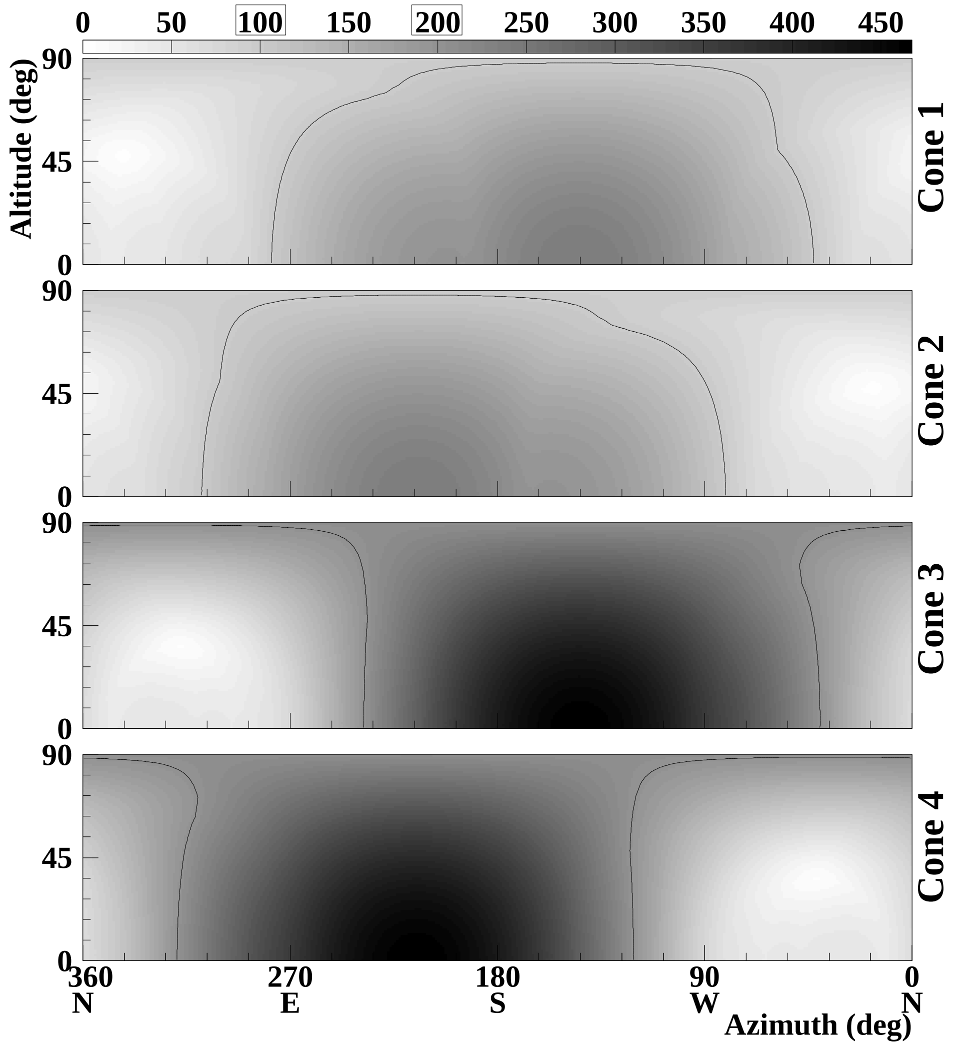

Figure 2.17: *Color scale indicates the theoretical length of the pulse train (ns) detected at the Winston Cones as a function of the azimuth and altitude of the incoming cosmic ray. The solid line of each plot shows the 100 ns (200 ns) contour line, which roughly corresponds to the integrator module time constant for cones 1&2 (3&4).*

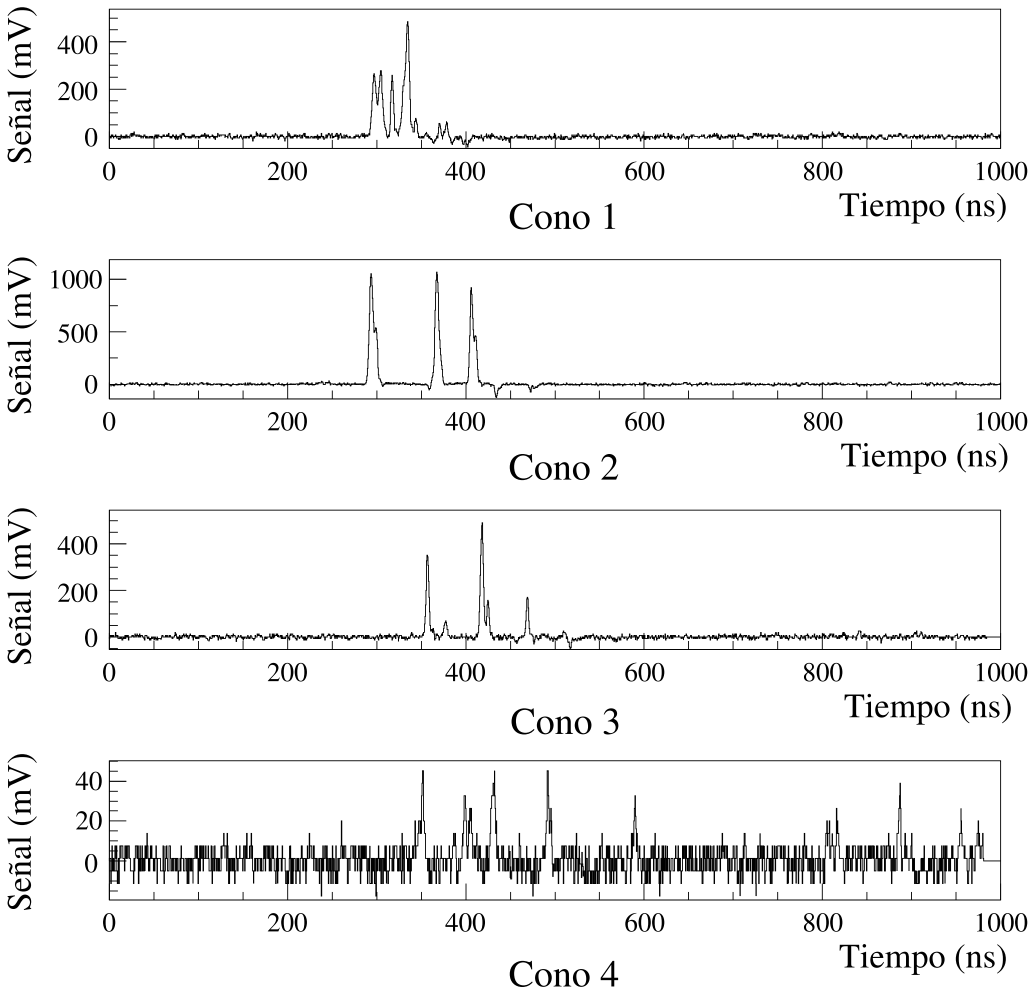

Figure 2.18: *When the signals that arrive to the PMTs generate a trigger, they are stored as four traces, one for each cone. In this picture a typical shower is shown as the voltage of the signal as a function of time (notice the different scales).*

2.2.6 Remote operation of GRAAL

One major feature of the whole setup is the possibility of remote controlling the experiment. This allows to run the experiment from Madrid or Munich, the two main research centers of the collaboration, without the need of constant displacement to the PSA. This amounts to a large reduction in travel budget and allows the person on shift to remain in contact with his everyday work.

Of course displacements to the PSA are unavoidable because from time to time it is necessary to replace some electronic modules or some upgrades and tests in the setup must be done, but the number of trips is much reduced thanks to this feature.

All the different parts of the setup have been designed with the aim of controlling them remotely via the Internet:

Control of the heliostats As already mentioned the program that controls the heliostats has a feature in which the different instructions to be followed during one night can be read from a previously written file. So during normal operation once the program is started no further operations are needed by the person on shift. In any case, it is always possible to check that the program is running smoothly exporting the display to the local machine where the person on shift is working (in Madrid or Munich). In addition a file with the positions of the heliostats is written every 3 seconds. This allows for later checks, at data analysis, to see whether something went wrong in the tracking of the heliostats. Besides, the operator at the PSA has instructions to check regularly that the program is running without problems.

In case of failure by the control system there are no severe consequences (apart from the loss of data acquisition), but in any case the heliostats have a local security system that sends them to rest position. The case of power cutoff is dealt with by a generator at the PSA that starts in case of power fail in the main line.

The hut The hut is permanently closed during the day and at night can be remotely opened. The electric door that closes the hut is connected to the CAMAC crate at the electronics, which is controlled from the main data acquisition PC. An order given at this PC, locally or via Internet, opens or closes the door.

To avoid for accidental operation several security systems were installed at this stage. A photo-electric sensor was fixed inside the hut and in case of excessive light the door is automatically closed. Additionally an infrared web camera was installed inside the hut, so at any moment it is possible to have a look at the hut to check whether the door is open or close or if there is any problem.

In case of main power failure the experiment is provided with 2 uninterrupted power systems (UPS) and a generator. The electronics, protected by the UPS's, detect the power cutoff and immediately send a signal that starts the power generator with the aim of closing the door.

The electronics The whole electronic setup is controlled by the computer through the CAMAC crate. At the beginning of data taking the data acquisition program is started, setting all the values in the electronics to the desired values. Certain values may be changed automatically during the night. Specifically the high voltages, which have to be lowered when there is moon, are set automatically at the defined hours to the desired values. Another web-cam is continuously monitoring the electronics rack, so it is possible to visually check at any moment whether there is any problem.

As a security system the electronics monitor the currents at the output of the PMT's, so in case of excessive light incident on the PMT's, the high voltage is cutoff for 10 seconds to prevent damage. In case this problems remains for a prolonged time the hut door is closed.

Weather conditions Another data that is very important to know during the night is the weather conditions, specially when the person on shift is not at the experiment site. To help in this task the operators at the PSA fill a form with the weather data during the day and also during the night. Apart from that, they give a visual confirmation of the atmospheric conditions, whether there is rain, clouds, etc. This point is also monitored with satellite images from Meteosat. Finally, we have installed a small weather station at the hut with measurements of windspeed, humidity and atmospheric pressure. These values are stored in the PC with the registered signals, and are continuously monitored by the data acquisition program so in case any of the variables gets outside security levels the hut door is closed to protect the experiment.

Security systems As we have already mentioned every important piece in the data acquisition is equipped with some security system to avoid damage. In fact, with the above described setup the control of the experiment during normal shift operation is quite straightforward. After starting the heliostat control program, the door of the hut is opened and the data acquisition program can be started. From here until the end of the night the programs control everything and the person on shift just needs to check that all the control parameters are correct. At the end of the night all the programs stop by themselves, the electronics are switched off, the heliostat field is turned down to rest position and the hut-door is closed, everything automatically.

During data taking, the acquisition program running on the main PC, continuously monitors different parameters (weather, excessive light, abnormal trigger rates, power cutoffs, ...) and in case there is any problem, not only does it close the hut door, protecting the experiment, but it also reports the error to the person on shift, with a phone call. This call also takes place if the Internet connection between the PSA and the place where the person on shift is, fails. In order to avoid this situation modems have been provided, so the person on shift can directly connect to the main acquisition PC and check whether everything is correct and shut down the experiment if necessary. As a last resort the operator has instructions on how to close the door with a remote control and in this way protect the experiment from damage.

Chapter 3

Simulation of the detector

In order to predict the behavior of the GRAAL telescope and to develop methods to analyze the gathered data, a detailed simulation of both the shower development and the experimental setup has been carried out.

First of all, the Čerenkov signal produced at observation level by an EAS generated by a cosmic ray has been simulated. This is accomplished with the CORSIKA program (§3.0.7), a series of subroutines where the different processes that take place during the development of extensive air showers are simulated. Čerenkov photons thus generated are carried through a detailed simulation of the optics and the electronics of GRAAL (§3.1), in order to obtain the expected signal at the digital oscilloscope.

Some of the parameters needed in the simulation are not known with the necessary precision, and had to be determined in an indirect way, adjusting the results of the simulation to the experimental measurements. The main values to be adjusted by the simulation, and which therefore have been employed in the determination of the unknown parameters, are the accidental rate for the sequential trigger, the single-peak trigger rate curve as a function of the trigger threshold, the non-linear gain curves obtained from the calibration with the standard pulses, and the cosmic-ray detection rate. The values measured in the previous chapter will be used in different parts of the simulation in order to set some limits to the undetermined parameters, specially the total gain and the light of night-sky background.

3.0.7 Simulation of shower development

The program that has been used for the simulation of the development of EAS's is the CORSIKA (COsmic Ray SImulation for KAskade) code, version 5.20 [7] which carries the simulation with a Monte Carlo method.

Several types of particles can be used as primaries (γ, protons, ...)

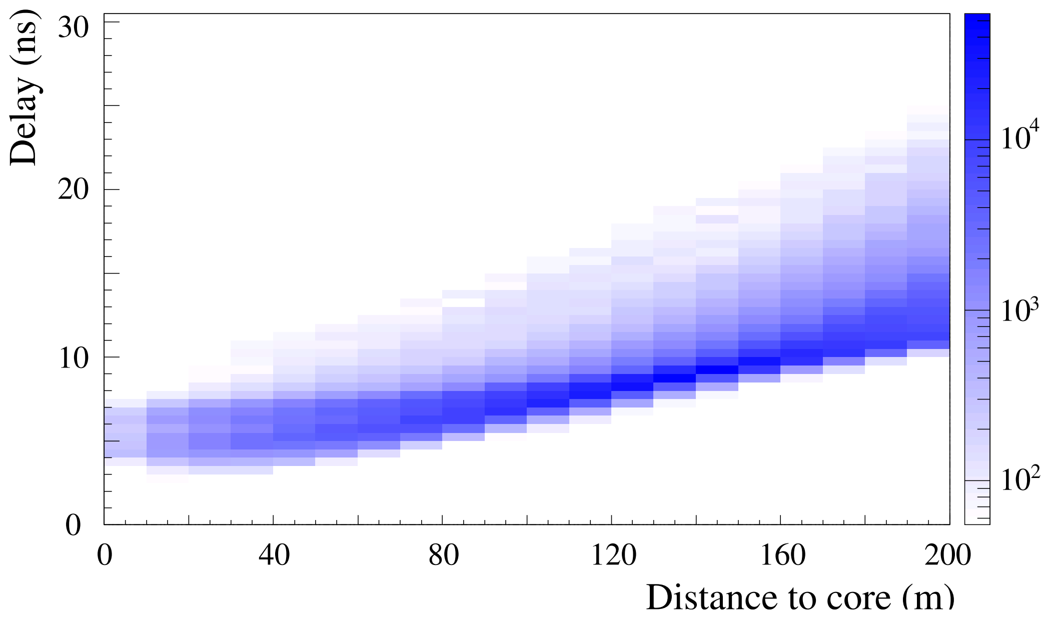

Figure 3.1: *Simulation of the Čerenkov-light front generated by a 200-GeV γ-ray incident with a zenith angle of 20 degrees. The arrival times to the observation level (origin is arbitrary) versus the distance to the core position is shown. Color intensity indicates number of photons. Note the logarithmic scale. Pulse width is of the order of 2.8 ns.*

with energies up to 10^{17}eV. The employed version includes simulation for 16 elemental particles (γ, $e^{\pm}$, π^0, $\pi^{\pm}$, $K^0_{S/L}$, $K^{\pm}$, p, n, $\overline{p}$ and $\overline{n}$) along with atomic nuclei with mass up to 56. Short lived particles as mesons η and ρ and hyperions as Λ and Σ don't appear explicitly, but are immediately substituted by their disintegration products. In the same way, π^0's are substituted by two photons and the possible disintegration $\pi^0 \to e^+ + e^- + \gamma$ is not taken into consideration, due to its low probability. Muons are transported without nuclear collisions, though the disintegration $\mu^{\pm} \to e^{\pm} + \nu_e(\overline{\nu}_e) + \nu_\mu(\overline{\nu}_\mu)$ and multiple Coulomb scattering are taken into account. Neutrons are considered stable, due to their long half-life. Besides, all charged particles suffer from loss of energy due to ionization, and modification of their travel path due to interaction with the Earth magnetic field is taken into account.

The model considered to describe hadronic interactions depends on the energy of the particle to be simulated. For energies at the mass center greater than 10 GeV a routine based in the model by Capdevielle [8] inspired on the Dual-Parton Model [9] is employed. For lower energies the Isobar Model [10] is used.

For electromagnetic interactions the EGS4 code [11] has been employed.

In this version of the EGS (Electron Gamma Shower) routines, photons may be simulated down to an energy of 1 KeV, meanwhile electrons and positrons can have energies as low as 10 KeV. The physical processes taken into account include: production of pairs $e^{\pm}$ by γ-rays; Compton scattering of photons; photoelectric effect; coherent Rayleigh scattering; bremsstrahlung radiation by $e^{\pm}$; continuous energy loss by $e^{\pm}$'s, as described by the Bethe–Block formula; Møller (e^+e^-) and Bhabba (e^+e^-) scattering; Molière multiple scattering of $e^{\pm}$'s, caused by elastic collisions with atomic nuclei; and positron–electron annihilation.

Transport of photons in the atmosphere between two consecutive interactions can be done without any computing problems as the interaction cross section is very small. But for $e^{\pm}$ it becomes impossible to simulate all interactions due to the large cross sections. Therefore only bremsstrahlung and Møller scattering are simulated in a discrete way. The rest of the inelastic collisions with energy loss and nuclei scattering are simulated by a continuous energy loss and a global change in the travel direction of the $e^{\pm}$.

The atmosphere was parametrized following the Linsley model [12], based on the standard American atmosphere, with some modifications for a better aerosol model [13]. It was divided in five parts. In the first four parts density varies exponentially with height, and in the fifth it is linear. The upper limit for the atmosphere is 112.8 Km, and above that height the density is considered to be zero. Absorption is taken into account in the form of ozone absorption, Rayleigh scattering and aerosol dispersion [13].

The final output of the program is a file with the type of particle, energy, generation height, wavelength, impact point, direction and arrival time for each particle that reaches observation level.

In figure 3.2, two examples of EAS development are shown, a 100-GeV gamma-initiated shower and a 300-GeV proton-initiated shower. Both the trajectories of particles with enough energy to induce Čerenkov light emission, and the resulting Čerenkov light distribution at sea level are displayed. The differences between both type of EAS's are evident. Electromagnetic showers preserve the general incoming direction of the primary particle, meanwhile in the proton-initiated shower the first interaction produces a fragmentation of the shower that originates several independent sub-showers. Conservation of the general direction of the original particle is less well conserved. This produces a distinct pattern in the structure of the Čerenkov-light pool on the ground. The γ-induced shower produces a Čerenkov-light pool with a high radial symmetry around the core (very similar to the theoretical pattern expected from the very simple model showed in figure **??**), and the

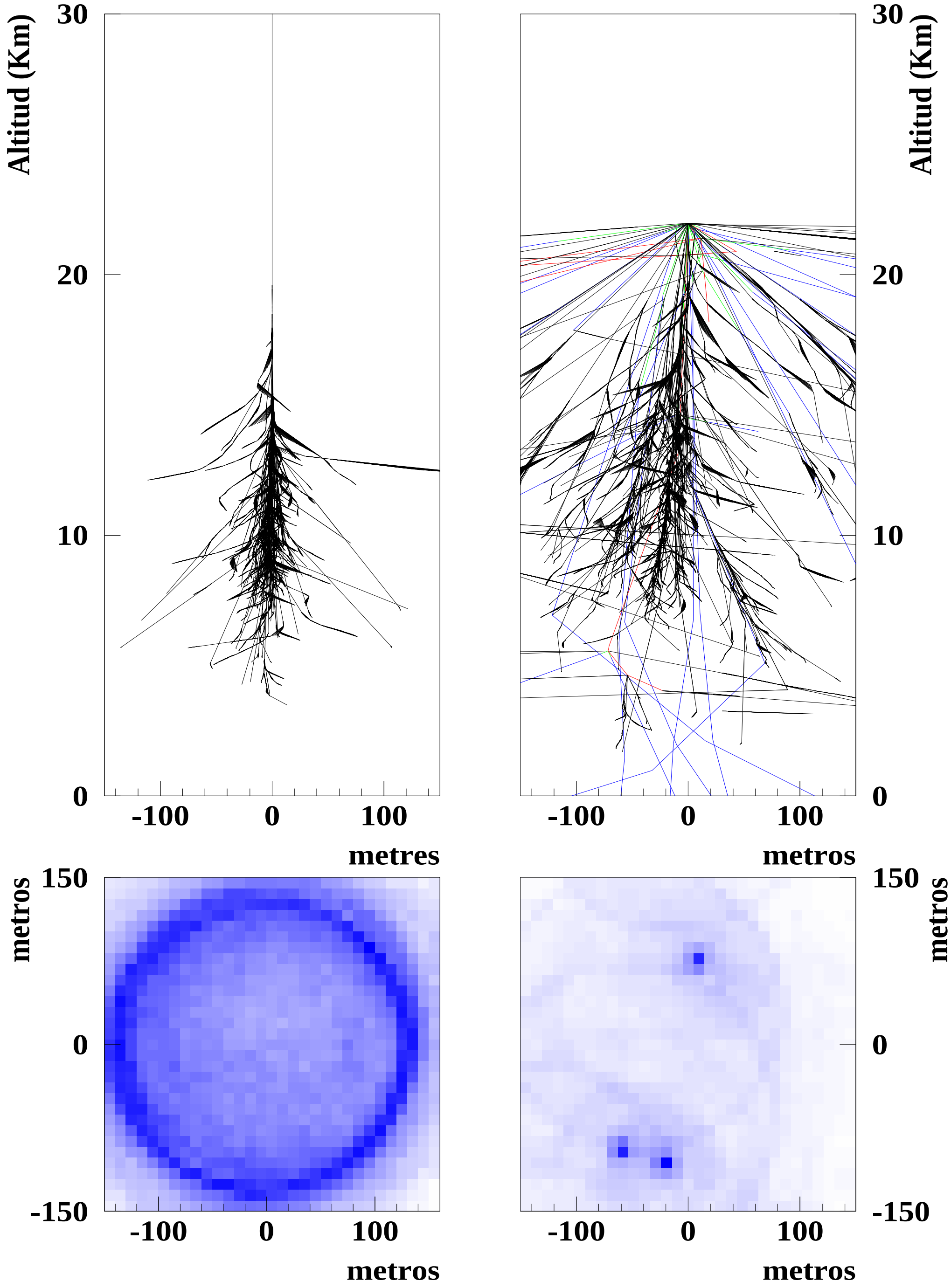

Figure 3.2: *Simulation of two Extensive Air Showers with vertical incidence generated by a γ of 100 GeV (left) and a 300-GeV proton (right). Top plots show the paths followed by particles with enough energy to induce Čerenkov light generation (black:$e^{\pm}$'s; red:hadrons; green:π's). Bottom plots show the Čerenkov light distribution at sea level.*

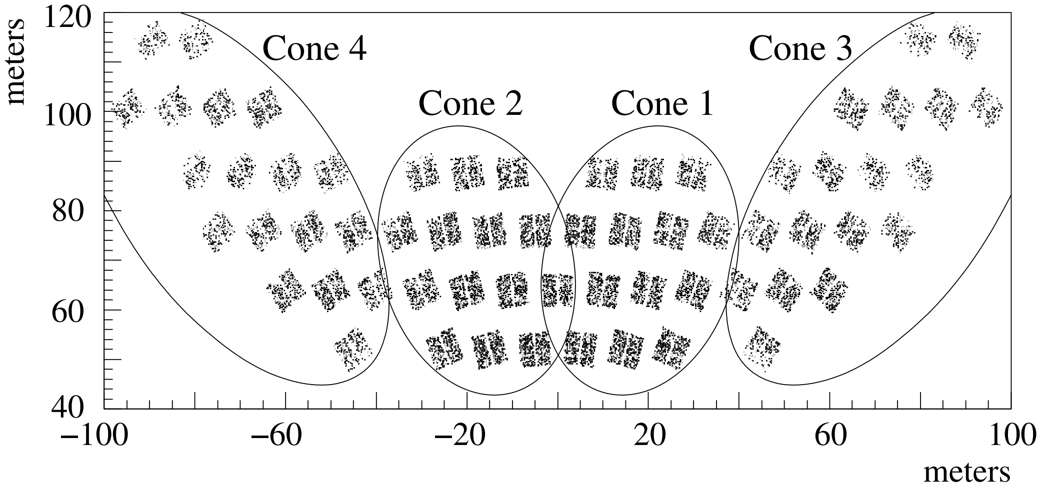

Figure 3.3: *Monte Carlo simulation of the heliostat field as seen by the four cones. Color intensity indicates number of photons collected from that position.*

proton initiated shower shows a series of *spots* without a clear pattern.

3.1 Simulation of the detector

The simulation of the shower development described in the previous section provides the necessary information on the generated Čerenkov light. Out of all the provided information, only the impact point with the observation level, the incident direction, the arrival time and the wavelength of each Čerenkov photon is employed.

The simulation of the detector can be divided in three main components: the simulation of the optics, the electronics that provide amplification and transmit the signal, and the trigger system.

3.1.1 Light collection

The light collection system comprises the heliostat field CESA-1, the Winston Cones and the photocathode of the PMT. The simulation program takes the Čerenkov photons generated in the CORSIKA code, reflects them on the heliostats, checks whether they are collected by any Winston Cone and verifies that it is not lost due to reflectivity or quantum efficiency.

The surface of the **heliostats** with its imprecisions and facets is approximated by the theoretical shape they should have. Then, this theoretical shape is blurred in order to simulate the imperfections of the real heliostat.

The chosen shape for the theoretical heliostat is a single spherical mirror divided in two big rectangular sections $6.75\,\mathrm{m}^2$. The focal length of the spherical mirror is that of the real facets of the heliostat that is simulated. Therefore the function describing the theoretical surface is:

$$x^2 + y^2 + (z - R)^2 - R^2 = 0$$

where R is twice the focal length of the facets of the considered heliostat.

For each Čerenkov photon that hits a heliostat the exact reflection point is calculated $(x_0,\, y_0,\, z_0)$. The reflection is determined by the normal plane to that point in the system of reference of the heliostat (z along the axis of the heliostat):

$$\hat{n} = \frac{1}{\sqrt{\left(\frac{\partial f}{\partial x}\right)^2 + \left(\frac{\partial f}{\partial y}\right)^2 + \left(\frac{\partial f}{\partial z}\right)^2}} \left[\left(\frac{\partial f}{\partial x}\right) \hat{\imath}, \left(\frac{\partial f}{\partial x}\right) \hat{\jmath}, \left(\frac{\partial f}{\partial x}\right) \hat{k} \right] \Bigg|_{(x_0, y_0, z_0)}$$

$$\hat{n} = \frac{1}{R}[x_0 \cdot \hat{\imath}, y_0 \cdot \hat{\jmath}, (z_0 - R) \cdot \hat{k}]$$

Imperfections in the mirror are simulated with a simple model, randomly generating errors at the point where the reflection takes place, and in its derivatives. This is done for each photon, so there is no precalculated surface, but it is being calculated for each reflection. The error in the position of the reflection point is introduced in the z axis only:

$$z_1 = z_0 + \delta z$$

where z_1 is the new coordinate and δz is a random number generated with Gaussian probability of mean zero and $\sigma = \lambda$.

Errors in the direction of the normal plane are introduced in the derivatives as:

$$\begin{aligned}
\frac{\partial f}{\partial x} \to \frac{\partial f}{\partial x} + \delta\left(\frac{\partial f}{\partial x}\right) &= \frac{\partial f}{\partial x} + \delta\left(\frac{\partial f}{\partial z} \cdot \frac{\partial z}{\partial x}\right) = 2(x + z - R) \cdot \delta\left(\frac{\partial f}{\partial x}\right) \\
\frac{\partial f}{\partial y} \to \frac{\partial f}{\partial y} + \delta\left(\frac{\partial f}{\partial y}\right) &= \frac{\partial f}{\partial y} + \delta\left(\frac{\partial f}{\partial z} \cdot \frac{\partial z}{\partial y}\right) = 2(y + z - R) \cdot \delta\left(\frac{\partial f}{\partial y}\right) \\
\delta\left(\frac{\partial z}{\partial x}\right) &= \frac{\delta z_x}{(a+b)/2} \\
\delta\left(\frac{\partial z}{\partial y}\right) &= \frac{\delta z_y}{(a+b)/2}
\end{aligned}$$

evaluated at (x_0, y_0, z_1), and where a and b are the dimensions of the two sections that constitute the simulated heliostat, and δz_x and δz_y are random errors generated with Gaussian probability, of mean zero and standard deviation σ_x and σ_y, such that:

$$|\sigma_x^2 + \sigma_y^2| \leq \lambda^2$$

Parameter λ depends on the accuracy of real heliostats to the intended theoretical shape, and was determined by comparison of the simulated image of the Sun on the tower plane with the real image dimensions. In figure 3.4 a simulated example of an image of a shower at the entrance of cones 1 and 2 can be appreciated.

In the simulation of the **Winston Cones** it is not necessary to calculate all the reflections suffered by a photon until it reaches the PMT. To save some computing time the cone can be parametrized by the dimensions of the outer opening, the angular acceptance curve and the reflectivity of the aluminized mylar foil for the mean number of reflections (89%, see §2.2.3).

Once the photon is reflected on the heliostat it is ray-traced to the cone plane. After checking that the photon hits inside the outer opening of a cone, it is tested for the angular acceptance and the reflectivity.

The last step of the photon transmission is to check that the photon that has arrived to the photocathode of the PMT is converted into photoelectron, so it is checked against the QE of the photocathode according to its wavelength.

These photoelectrons are stored in time histograms, one for each cone, divided in time bins. Each time bin contains the number of photoelectrons that arrived within t and $t + \Delta t$. The width of each time bin, Δt, is 0.5 ns, the time resolution of the oscilloscope.

3.1.2 The electronics

At this stage of the simulation we have a time trace for each cone, divided in time bins of width Δt. To simulate the electronics, from the photocathode to the trigger logic, we use a model where all the effects introduced by the PMT, the amplifiers and the cables are considered in three steps: a convolution with a widening function, a linear gain at the PMTs, and a non-linear gain at the amplifiers.

The traces are convoluted with a gaussian **widening function**. Due to the fast electronics employed in GRAAL and after the test that have been

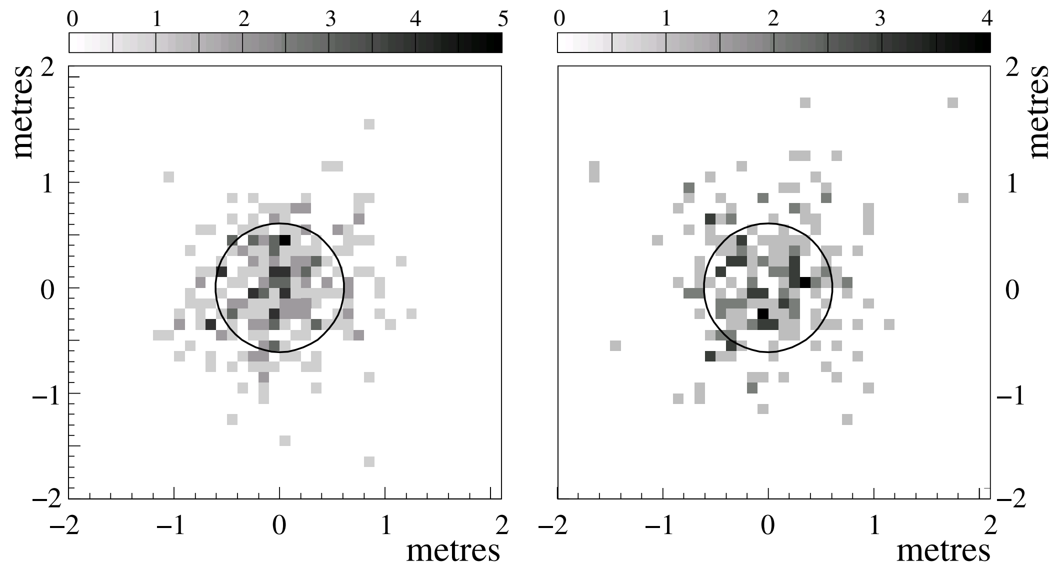

Figure 3.4: *Simulation of the reflected image of a 100-GeV γ-generated shower on the plane of cone 1&2. The shower core position was located near the center of the array (69 m North of the tower). Circles represent the cone's outer opening.*

carried out, we can say that the main focus of instrumental widening is the PMT. Any other widening that takes place at other stages of the electronic chain (amplifiers, cables) is negligible.

The value of the instrumental widening is estimated by comparison of the typical width of a detected Čerenkov pulse with the mean width of proton induced Čerenkov pulses simulated with CORSIKA at the photocathode. After correcting the real pulses for the non-linear gain, the difference in these two values is due to the instrumental widening. The measured mean sigma for real pulses es ~ 2.10 ns, while the width of simulated pulses is ~ 1.28 ns. Therefore the widening function used in the simulation is $\sigma_{instr} = 1.84$ ns.

The **linear gain** introduced by the PMT's, G, modifies the content of each time bin as $C_i = n_i \cdot G$ (Coulombs). The manufacturer provides the value of the direct-current gain, but the needed value is the gain for fast pulses, which is unknown. Therefore, the value of G will be adjusted by comparison with the real data.

The **non-linear gain** is described by the function obtained in §2.2.5.1. This function is useful only to obtain the output amplitude (in mV) for a pulse originated by a charge injected with the time characteristics of the standard pulse. Once these time characteristics are known, we can infer the output amplitude in each channel of a trace. In order to do this we assimilate the charge in each channel to the charge corresponding to the maximum channel of the standard pulse. If we consider a standard pulse with a gaussian like shape, this relationship can be described as: §2.2.5.1.

$$\frac{C_i}{\Delta t} = \frac{C_P}{\sqrt{2\pi}\sigma_P}$$

where C_i is the charge in Coulombs contained in the time bin of width Δt, and C_P is the equivalent charge of the Phillips pulse of width σ_P.

As already mentioned, the Phillips pulse is not symmetric, but we can correct for it. Let's consider the asymmetric pulse as one half gaussian to simulate the rise of the pulse, and an exponential fall:

$$\text{If} \leq t_o \Rightarrow f(t) = \frac{N_1}{\sqrt{2\pi}\,\sigma_1} \cdot e^{\frac{(t-t_o)^2}{\sigma_1^2}}$$
$$\text{If} \geq t_o \Rightarrow f(t) = M_2 \cdot e^{\frac{-(t-t_o)}{b}}$$

where t_o is the position of the maximum, M_2 is the maximum value of the exponential function, that must equal to the maximum of the gaussian:

$$M_2 = M_1 = \frac{N_1}{\sqrt{2\pi}\sigma_1}$$

Let's compare the charge injected with a asymmetric pulse like this, with the one injected in the gaussian pulse, while both have the same width and maximum. In the symmetric pulse the injected charge, maximum value, and width (FWHM) are given as:

$$\begin{aligned}
f(t) &= \frac{N_{sym}}{\sqrt{2\pi}\,\sigma_{sym}} \cdot e^{\frac{(t-t_o)^2}{\sigma_{sym}^2}} \\
\text{Max} &= M_{sym} = \frac{N_{sym}}{\sqrt{2\pi}\,\sigma_{sym}} \\
\text{Width} &= FWHM_{sym} = 2 \cdot \sqrt{2 \cdot \ln 2} \cdot \sigma_{sym} \\
\text{Injected charge} &= N_{sym} = M_{sym} \cdot FWHM_{sym} \cdot \sqrt{\frac{\pi}{4 \ln 2}}
\end{aligned}$$

In the asymmetric pulse:

$$\begin{aligned}
\text{Max} &= M_{asym} = M_1 = M_2 \\
\text{Width} &= FWHM_{asym} = \sqrt{2 \cdot \ln 2} \cdot \sigma_1 + b \cdot \ln 2 \\
\text{Injected charge} &= N_{asym} = \frac{N_1}{2} + M_2 \cdot b = M_{asym}\left(\frac{\sqrt{2\pi}\sigma_1}{2} + b\right)
\end{aligned}$$

We can define the degree of asymmetry of the function as the fraction of the total width of the pulse that is due to the gaussian:

$$x = \frac{FWHM_2}{FWHM_1} = \frac{b \cdot \ln 2}{\sigma_1 \cdot \sqrt{2 \cdot \ln 2}} \Rightarrow b = FWHM_{asym} \frac{x}{(x+1)\ln 2}$$

Therefore:

$$\begin{aligned} N_{asym} &= M_{asym} \cdot b \cdot (\frac{\sqrt{\pi \ln 2}}{2 \cdot x} + 1) = \\ &= M_{asym} \cdot FWHM_{asym} \cdot \sqrt{\frac{\pi}{4 \cdot \ln 2}} \left(\frac{\sqrt{\pi \ln 2} + 2 \cdot x}{\sqrt{\pi \ln 2} \cdot (x+1)} \right) \end{aligned}$$

Taking into account that the maximum and FWHM of both the symmetric and asymmetric pulses must me the same, we get:

$$N_{asym} = N_{sym} \cdot \left(\frac{\sqrt{\pi \ln 2} + 2 \cdot x}{\sqrt{\pi \ln 2} \cdot (x+1)} \right)$$

From the real data we get that x has a value near 8, and therefore the charges injected by both pulses are related by $N_{asym} = 1.32 \cdot N_{sym}$. We will have to take this into account before using the non-linear gain curve obtained with the Phillips pulser.

The result of the described calculi yield the conversion of the photoelectron charge of each channel to picocoulombs. Checking this value in the curves for the non-linear gain obtained in §2.2.5.1 we get the corresponding voltage for the considered bin.

3.1.3 The trigger system

Both the charge trigger and the sequence trigger, are simulated, but the approach is different, according to the modules and logic employed in the real setup.

3.1.3.1 The charge trigger

To simulated the charge trigger logic the module to be simulated is the EG+G 579 integrator. The simulation of this module takes as input value the traces after being converted to voltages (as shown in the previous section), and gives as output the integrated signal with the correct time constant.

The response of the real integrator module for fast signals coming from the four cones is parametrized in §2.2.5.2, where the characteristics of the input and output signals are given. The rise time is defined as the interval, before the maximum, where the signal rises from 10% to 90% of the maximum. In the same way, fall time is defines as the interval, after the maximum, where the signal falls from 90% to 10% of the maximum.

The input signal is reproduced with two half Gaussians, to account for the asymmetry. The parameters of each Gaussian are determined in order to have a fall time twice the rise time, while the width of the total pulse is that of the real signal. The integrator module is simulated with a convolution algorithm with an exponential function $V_{out} = A \cdot V_{in} \cdot e^{-t/B}$ where parameters A and B are adjusted until the simulated output function resembles the real one. The chosen values for the four cones, and the simulated input and output signal parameters are (errors are shown with respect to the real signal):

Simulated integrator			Cone 1	Cone 2	Cone 3	Cone 4
A parameter			0.0413	0.0394	0.0694	0.0722
B parameter		ns	115	115	200	200
Input Signal	Maximum	mV	250.0	290.0	260.0	250.0
	FWHM	ns	7.0 (+0%)			
	Rise time	ns	6.0 (+0%)			
	Fall time	ns	12.5 (+4%)			
Output Signal	Maximum	mV	145.0	160.0	260.0	260.0
	FWHM	ns	89.5 (-9%)		149.5 (-6%)	
	$1/e$ fall time	ns	117.0 (+13%)		201.5 (+1%)	
	Rise time	ns	13.5 (-44%)		14.5 (-80%)	
	Fall time	ns	531.5 (-8%)		922.5 (+23%)	

From these data it can be observed that the input signal has been correctly simulated with this simple algorithm. The output signal shows a good simulation of the response of the module. The only parameters which show large errors are rise time, which is not so important in this case, and fall time, which is difficult to determine precisely in the real case due to intrinsic difficulty in determining the end of the tail among the noise fluctuations. Important parameters as the maximum, FWHM and $1/e$ fall time are very well reproduced. An example of the way the signal is modified by the simulated integrator module can be seen in figure 3.5 where the test pulse is convoluted with the integrator function. For an example on how the integrator signal evolves when analyzing a complete trace see figure 2.14.

Once the trace has been convoluted with the integrator algorithm, it is tested to see whether the threshold set at the electronics (35 mV) is passed. If so, a cone trigger takes place. To have a total trigger at least 3 cones must

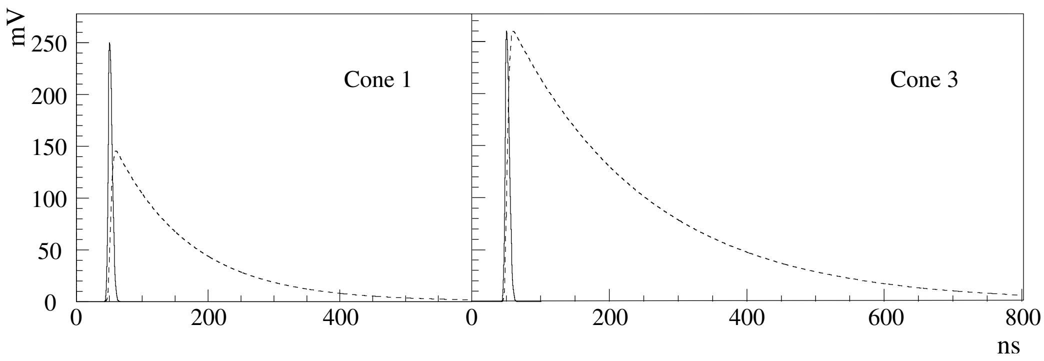

Figure 3.5: *Example of how the simulation of the integrator module modifies a simulation of the input test pulse.*

trigger within 200 ns.

3.1.3.2 The sequence trigger

The approach to simulate the sequence trigger logic is different from the one used in the charge trigger simulation. The electronics is not simulated in a module by module base, but only the logic is reproduced. In §2.2.5.2 the sequence trigger logic is described. Basically, the mechanics consist on the following: once a first peak passes a threshold (30 mV), after a delay of 20 ns the signal is tested or 40 ns looking for a peak higher than the threshold. If this second peak exists, the procedure is repeated, and if a third peak is found a trigger for the cone is given. That is exactly the way the simulation works on the simulated trace, without taking into account the exact shapes of the signals produced by the discriminators and coincidence units employed in the electronics.

To have a total trigger, both cone 1 and 2 must trigger within 100 ns.

3.1.4 The night-sky background

The contribution to the signal in each cone by the night-sky background has been determined with two different procedures.

The first method is based in the measurement of the absolute value of the night-sky background, L, in photons/m^2/s/sr. From this value the contribution of each heliostat to the number of photons N collected by each PMT in a time interval Δt can be inferred:

$$N = L \cdot S \cdot \Omega \cdot Q \cdot R \cdot \Delta t$$

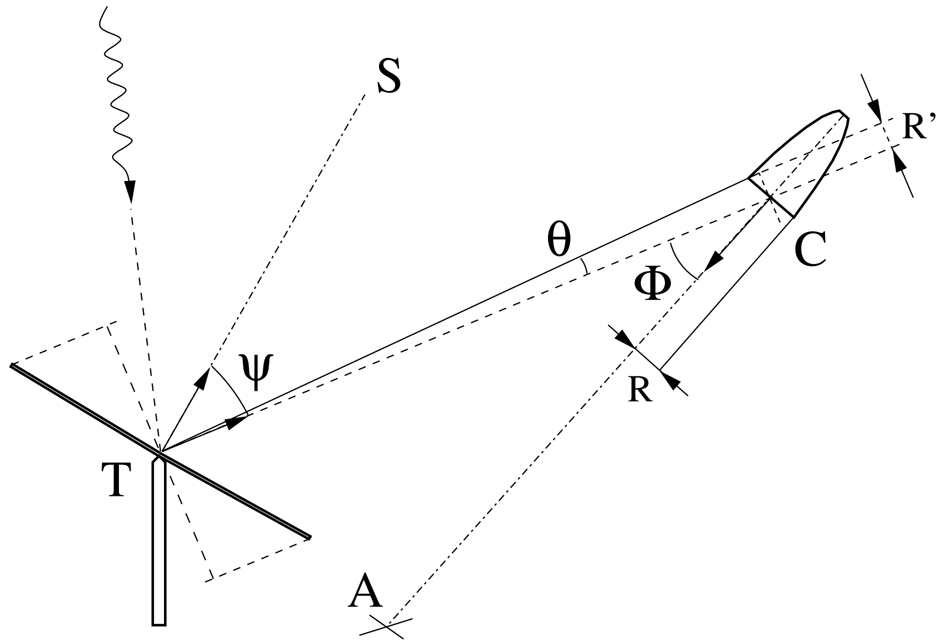

Figure 3.6: *Scheme with the relative positions of the heliostat, T, cone, C, aiming point of the cone, A, and convergence point, S, and angles to be used in the calculus of the solid angle.*

where S is the area of the heliostat, Ω is the solid angle seen by the PMT, Q is the Quantum Efficiency of the photocathode and R is the mean reflectivity of the heliostat and the aluminized mylar foil of the cone over the considered wavelength range.

While S, Q and R can be measured, we have to calculate the solid angle seen by each cone through the heliostats. A simple approximation can be done, as shown in figure 3.6. The solid angle Ω seen by a cone through heliostat i is given by the area of the outer opening of the cone projected on the cone–heliostat axis, $\overrightarrow{CT}$:

$$\begin{aligned}
\Theta &= \pi \cdot R \cdot R' = \pi \cdot R^2 \cdot \cos\phi \\
\Omega_i &= \frac{4\pi \cdot \Theta}{4\pi \cdot |\overrightarrow{CT}|^2} = \frac{\pi \cdot R^2 \cdot \cos\phi}{|\overrightarrow{CT}|^2} = \pi \cdot R^2 \cdot \frac{\overrightarrow{CT} \cdot \overrightarrow{CA}}{|\overrightarrow{CT}| \cdot |\overrightarrow{CA}|} \cdot \frac{1}{|\overrightarrow{CT}|^2}
\end{aligned}$$

where R is the radius of the outer opening of the Winston Cones, ϕ the angle formed by the axis of the heliostat and the cone–heliostat axis, and A, C, T are respectively the coordinates of the aiming point of the cone, the position of the center of the cone's entrance and the heliostat center (figure 3.6).

Then, for the N_{hels} heliostats that give light into one cone:

$$\begin{aligned}
\mathrm{N}_{cone} &= \sum_{i=1}^{N_{hels}} L \cdot S'_i \cdot \Omega_i \cdot Q \cdot R \cdot \Lambda_i \cdot \Delta t = \\
&= L \cdot S \cdot Q \cdot R \cdot \Delta t \cdot \sum_{i=1}^{N_{hels}} (\cos\psi_i \cdot \Omega_i \cdot \Lambda_i)
\end{aligned}$$

where $S'_i = S \cdot \cos\psi_i$ is the projection of the surface of heliostat i on the heliostat–cone axis, and Λ_i is the angular acceptance of the cone for heliostat i, which depends on the angle formed between the axis of the cone and the cone–heliostat axis, Φ (see §2.2.3).

Therefore the result depends on the orientation of the heliostats (through ψ). In any case the dependence is not strong and we can calculate mean values for $\sum_{i=1}^{N_{hels}}(\cos\psi_i \cdot \Omega_i \cdot \Lambda_i)$ in the four cones, which are $\sim 1.33 \cdot 10^{-3}$ sr ($\sim 0.87 \cdot 10^{-3}$sr) for cones 1 & 2 (3 & 4).

A more precise estimation of the solid angle seen by each cone can be done with a Monte Carlo simulation, yielding similar values that differ from this uncomplicated estimations in less that 5%. Therefore, and to save computing time this simple algorithm is used in the simulation.

Light intensity L was measured with a single-photon counting method (see §2.2.1) in a clear night with a result of $3 \cdot 10^{12}$ photons/m^2/s/sr. With this value it can be inferred a noise level of $\sim$13(9) photons/ns in cones 1&2 (3&4).

The second method employed is based on the measurement of the amplitude distribution of single peaks from the sky background in the traces. For a given value of N the amplitude distribution is determined by the Poisson statistics, and by the response of the electronics (PMT, cables, amplifiers, ...), and it can be easily obtained with the simulation of the detector. A realistic value of N must generate an amplitude distribution similar to the one obtained from the real data.

The main difficulty to use this method precisely is the *after-pulsing* that takes place in the PMT's. This effect is important in PMT's working under high background noise conditions and is due to the ionization of the remaining gas in the tube. When a high number of electrons cross through this gas, the probability for an electron to ionize a molecule is not negligible. Molecules ionized in this way travel toward the photocathode, colliding with it and extracting some electrons, which are detected as a pulse. This process is specially probable when a real pulse takes place, giving way to the generation of an afterpulse 100 to 200 ns after the original pulse. The PMT model

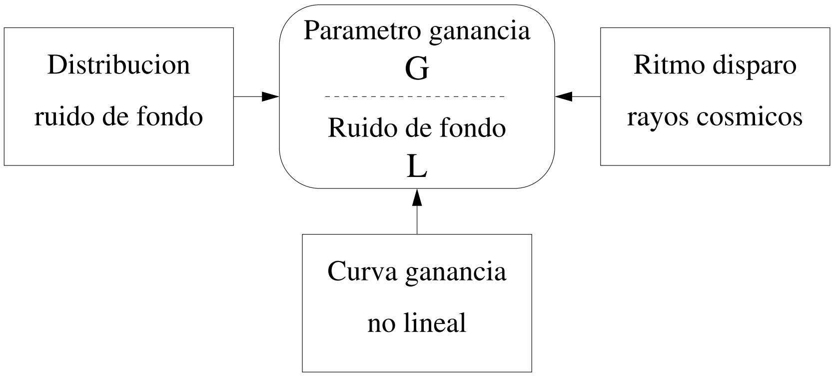

Figure 3.7: *Scheme of the method employed for the fine tuning of the parameters of the simulation.*

employed in GRAAL is studied in [14] and, according to the calculations of its authors. the expected contribution to the single-pulse trigger rate of afterpulsing for a threshold of 30 mV at a typical working background current may reach 10^6 Hz, which is comparable to the measured value.

The amplitude of the pulses induced by afterpulsing do not follow a poisson distribution, and therefore their distribution cannot be simulated in a precise way with a simple model. At low amplitudes the distribution is dominated by background fluctuations, but at larger amplitudes it is dominated by afterpulsing. Therefore it is expected that small modifications in the simulation may reproduce the experimental curves at small amplitudes, with worse reproduction for larger amplitudes.

3.1.5 Fine tunig the simulation

All through this chapter, most of the parameters necessary for the simulation have been determined. Still, and as the experiment has been taking data since July 1999, it is possible to introduce several minor corrections in some of the parameters, in order to obtain a better agreement between the results obtained from the simulation and those measured in the experiment. Some parameters were chosen with this aim: the night-sky background L and the linear gain G. In order to determine a better value for G it was of main importance the measure of the non-linear-gain curves, obtained from the calibration with the standard pulses (see 3.1.2). A further indetermination in these curves would have introduced a higher degree of freedom in the gain, which would have proven fatal. All the other values in the simulation have remained untouched from the measurements.

In the same way it is necessary to fix some reference values to be em-

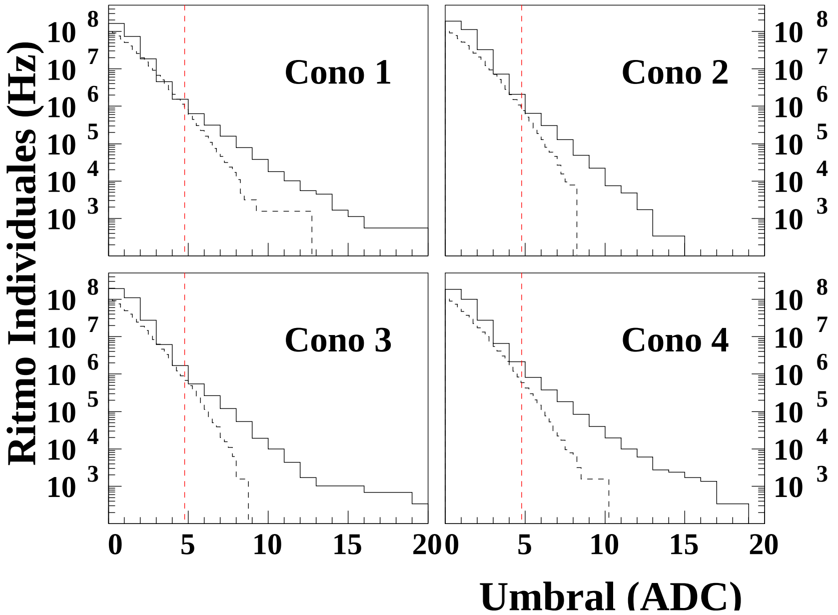

Figure 3.8: *Single trigger rate as a function of the threshold, for the four cones, obtained from the real data (solid lines) and simulation (dashed lines). An ADC count is equivalent to 6.275 mV.*

ployed in the comparison. On one side, these values should show a strong dependency with the fundamental parameters of the experiment. On the other hand, they should be easy to measure. Therefore, the values employed are the hadron detection are close to 4 Hz under good weather conditions, and the amplitude distribution of the background noise (figure 3.8).

In this way, some small modifications on the values of L and G have been carried out, in order to find those which produced in the simulation similar values to those measured in the experiment. The value of L has been fixed in 8.0 photons/m^2/s/sr, higher that the measured value of 3 photons/m^2/s/sr, which is easily explicable if we take into account that the experimental value was measured under exceptionally good conditions. In the same way we cannot underestimate the effect of afterpulsing. In order to account for this effect, in the employed model it is necessary to introduce a higher noise level. In figure 3.8 it is shown the comparison of the background noise distributions for the simulation and the experiment. As its already been said, due to the gaussian model employed in the simulation it is impossible to completely reproduce the experimental curves, specially for the highest amplitudes., where the non-gaussian contribution of afterpulsing is most important.

The final gain values applied to each cone in the simulation, obtained from the fine tuning of the simulation, are shown in figure 3.9, where the

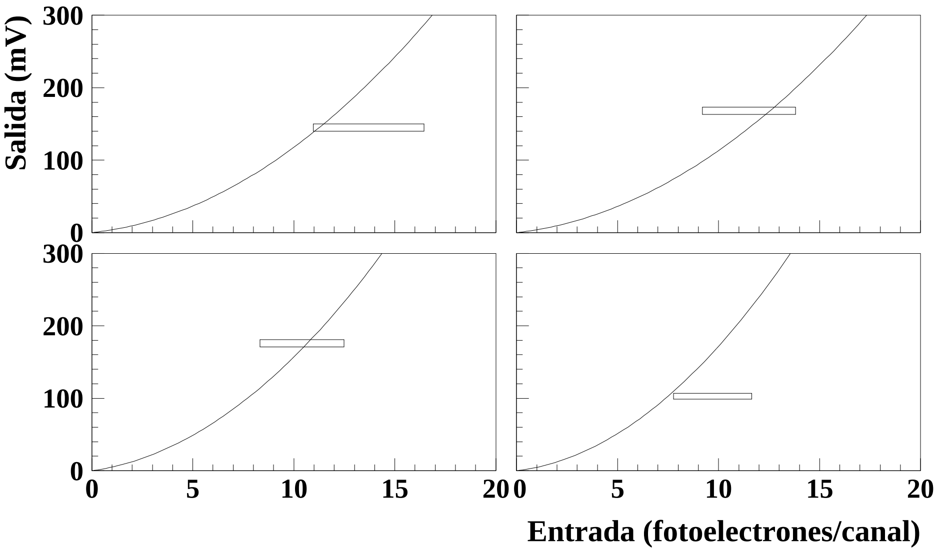

Figure 3.9: *Gain curves employed in the simulation of the electronics. Rectangles show the error boxes of the calibration values of the LED's.*

conversion from photoelectrons in one bin to voltage is shown.

Once we have obtained these values, we can do a further test, estimating the accidental rate for the sequence trigger (which is more sensible to peak fluctuations than the charge trigger). In GRAAL, accidental rate was measured to be of 0.0–0.2 Hz under good weather conditions. For the simulated accidental rate we could generate noise traces and then run the simulated trigger (see §2.2.5.2), but this would be very time consuming (it would take ∼140 days to generate and analyze 10 seconds of simulated noise on a Silicon Graphics R10000 processor). Fortunately the sequence-trigger accidental rate can be calculated with a simple algorithm:

Let R_1 be the trigger rate for peaks higher than a given threshold T, and τ the width of the *search window* as defined in §2.2.5.2. Then, the probability of having at least one peak higher than T in τ can be approximated by $P_\tau \simeq R_1 \cdot \tau$. According to the description of the sequence trigger (§2.2.5.2), two such regions must trigger in addition to a first single-peak trigger, in order to have a cone trigger. This means that the rate of a cone trigger is $R_{cone} = R_1 \cdot P_\tau^2 = R_1^3 \cdot \tau^2$. To have a total trigger both cones 1 and 2 must trigger within a coincidence period Δ, so the rate for a total sequence trigger is given by $R_{seq-trg} = R_{cone}^2 \cdot \Delta = R_1^6 \cdot \tau^4 \cdot \Delta$. Using the rate for a threshold of 30 mV from the simulation plots in figure 3.8 then:

$$
\begin{aligned}
T &= 30\,\mathrm{mV} \\
R_1 &\simeq 1.0 \cdot 10^6\,Hz \\
\tau &= 40\,\mathrm{ns} \\
\Delta &= 100\,\mathrm{ns}
\end{aligned}
$$

we get a simulated accidental rate for the sequence trigger of 0.26 Hz, quite compatible with the measured rate.

Chapter 4

Air-shower observables

In this chapter we will study some of the general properties of the Čerenkov component of air showers generated by primaries in the energy range of this work. The aim is the search for observables that may allow the identification of the parameters of the primary particle and in this way improve the telescope's sensitivity. In particular, the determination of the incoming direction and the background-cosmic-radiation rejection would greatly increase the sensitivity. With this aim a small library of events induced by primaries of fixed energies was generated. For γ showers, energies of 200 and 1000 GeV were chosen, while the energy of proton primaries was chosen in such a way that their showers would induce a similar amount of Čerenkov light at observation level. This effect is achieved with protons of approximately 500 and 2000 GeV. For each energy 100 showers were generated, with vertical incidence, dividing the total amount in two sub-samples, one with the core position fixed at the origin of the system of reference, and the other one with the core randomly located within a radius of 150 m around the heliostat-array center.

The parameters chosen for study are those directly accessible with the data collected with an heliostat array similar to GRAAL, but the results shown in his chapter are easily extendible to other experiments with solar plants. In particular, we will show the results of the analysis of the spatial distribution of the Čerenkov light (lateral development) and the time structure of the Čerenkov front that arrives to the observation level.

As in any other γ-ray telescope using a solar plant, the possibilities to use this parameters are highly influenced by the restricted field of view. Some of the limits could be altered with the use of the convergent-view technique (see §2.2.3). In order to study the possible effects introduced both by the convergent-view technique and the restricted filed of view, three cases have been taken into account:

Wide field of view configuration All the Čerenkov-light generated in the shower and arriving to the observation level, is detected, without any further limitation;

Restricted field of view in parallel view Only Čerenkov photons with and incident angle with respect to the observed axis of less than 0.5 degrees (value similar to the field of view of currently working solar plants) are detected. Detector are aimed toward the observed source (*parallel view*):

Restricted field of view in convergent view Similar to the previous configuration, with the exception that the detectors are aimed toward a convergent point located 10K̇m above the origin of the system of coordinates, in *convergent view* (see fig. 2.6).

Čerenkov photons are detected within an area of $360\times360\,\mathrm{m}^2$, in a matrix of 72×72 detectors. Each detector has an area of $40\,\mathrm{m}^2$, similar to that of a typical heliostat. In this way the fluctuations induced by the limited area of the detector are taken into account. Apart from the non-realistic configurations above mentioned, Čerenkov photons are also carried through the complete simulation if the optics of the GRAAL detector, storing the signal given by the shower at the PMT's, previous to the electronics.

It is expected that the study of the EAS's observables would help in the determination of the main parameters of the primary, as the incoming direction, the core position, and the particle type. Unfortunately, though it will be shown that the main values of the observables can be correlated with one or some of these parameters, fluctuations in the observables will limit the power of these methods. This is the reason why it will be necessary in this chapter to pay special attention to the statistical fluctuations.

4.1 Čerenkov-light lateral distribution

The Čerenkov-light spatial distribution at observation level is a characteristic that can be useful to determine the primary type. In figure 4.1 it is shown the typical patterns for the Čerenkov-light detected at observation level, generated by a 200-GeV γ-ray and a 500-GeV proton, in the three observation configurations described above.

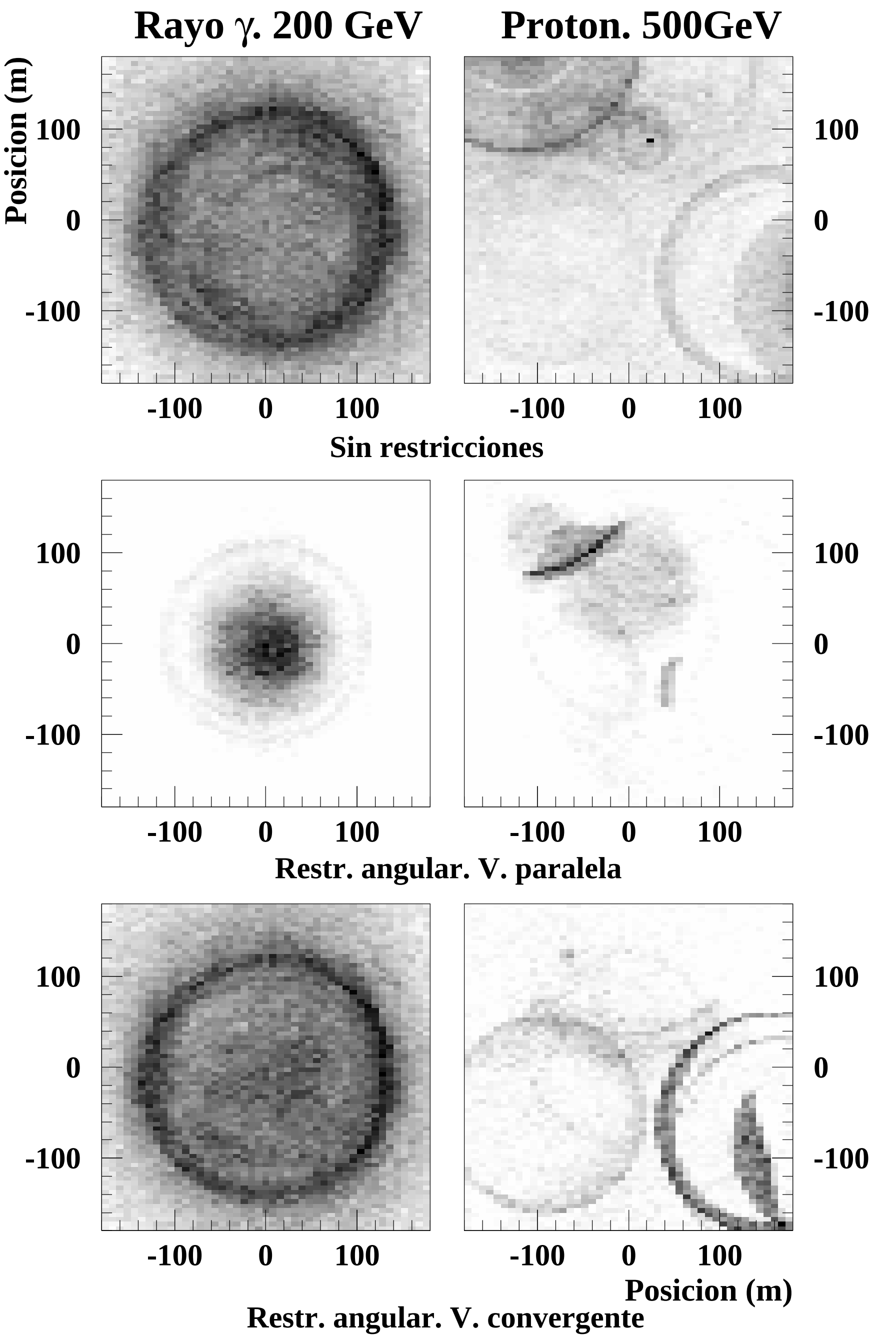

Figure 4.1: *Typical Čerenkov light distributions detected at observation level (505 m a.s.l.). Showers were generated by a γ ray and a proton with vertical incidence, and the core located on the projection of the convergence point. Results for the three configurations described in the text are shown.*

Due to the large fluctuations taking place in proton showers, it is difficult to extract a significant conclusion from the observation of just one example, apart from the irregular distribution of the detected light. On the other hand, showers initiated by γ-rays show a regular pattern.

When all the protons arriving to observation level are detected (*upper* plots) it can be observed that the Čerenkov light density is quite constant from the core ($r = 0$) to the *hump*, located at a distance r_h ~120 m. At larger distances, the detected Čerenkov-light density decreases with distance.

In the second configuration, with restricted field of view in parallel (*center*), it can be observed a distribution very different from the previous one. Detectors located near the *core* position, as they look along the shower axis, detect an important fraction of the incident light, meanwhile detectors located further away from the *core*, due to the restricted field of view, detected lower fractions of light as they are located further from the *core*.

In the convergent view configuration (*lower*), as the detectors are aiming to a point near the position of the maximum of the shower, most of the Čerenkov light generated by the showers near or above this point is detected, event at large distances from the *core*. The original pattern of the Čerenkov-light lateral distribution generated by the shower is reproduced almost exactly. This is completely true only with the maximum of the showers takes place near the convergence point. In any other case the observed distribution may be altered, as will be shown in §4.6.

Assuming that the distribution of the Čerenkov-light density ρ (photons/m^2) is symmetric with respect to the shower axis, we can define the radial distribution function $\rho(r)$, where r is the *core* distance. For shower number j, it can be defined $\rho_j(r_i)$, in the distance interval i, from r_i to $r_i + dr$, as the mean value of the Čerenkov-light density for those detector with the geometrical center located in the i interval. For each primary type and energy it is possible to obtain the mean value of $\rho(r)$ through the mean of $\rho_j(r_i)$ for all the generated showers. The width of the distribution is calculated in each distance interval as the intervals to the right $\Delta\rho_{dcha}$ and left $\Delta\rho_{izda}$ of the median, necessary to include 34% percent of the distribution (see figure 4.2). These definitions are more convinient than the usual mean and standard deviation, that can be highly influenced by the tail of the distribution. Results are shown in figure 4.3.

In the first configuration, were the Čerenkov-light is detected **without restrictions**, γ-ray showers show a value for $\rho(r)$ almost constant from the *core* to the *hump*, with a slight increment for $r \lesssim r_h$ at 200 GeV. At $r > r_h$, light density falls steeply with r. In 100-GeV γ-showers the behavior is similar, through the mean value is somewhat more constant. On the other

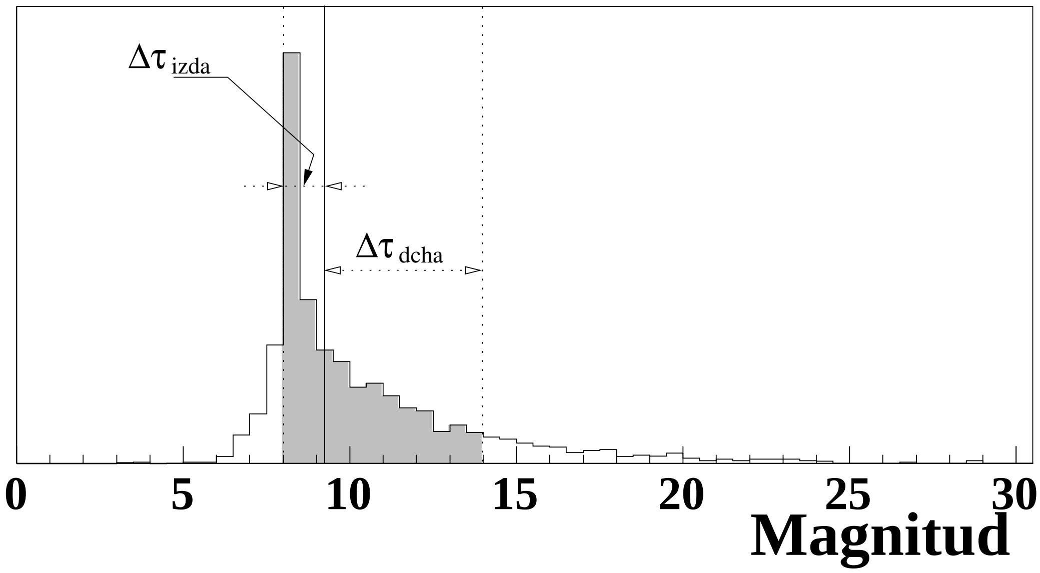

Figure 4.2: *In the case of asymmetric distributions, it is usual to use as descriptors of the width of the distribution, the interval that includes 34% of the events to the right and 34% to the left of the median value (solid vertical line).*

hand, fluctuations show a different behavior. While at lower energies they are almost independent with r, at higher energies fluctuations are quite larger near the *core*, and decrease with r to a minimum near the *hump*. For $r > r_h$ fluctuations are quite small at both energies. For proton showers it can be observed that $\rho(r)$ decreases with r, both at high and low energy, and that although fluctuations are smaller at higher energies, in any case they are much larger than in γ showers.

If the detectors have a limited field of view, in **convergent view**, those near the *core* are not much affected, but in those further away the collection efficiency for Čerenkov photons decreases a lot with r. In γshowers, detectors located at $r \gtrsim 100\,\mathrm{m}$ detect almost no Čerenkov photon. In proton showers the limit distance is somewhat larger. This is due mainly to the larger transverse momentum of hadronic interactions that produces more photons with low incident angles with respect to the shower axis at large r values. In this configuration the *hump* is not appreciated, as the lateral distribution is dominated by the angular acceptance function.

When using the **convergent view technique**, if the maximum of the shower takes place near the convergence point, the detected lateral distribution is very similar to the original one. Function $rho(r)$ is almost constant for $r < r_h$, though now γ-showers of higher energy show a maximum in $\rho(r)$ near $r = 0$, decreasing then with distance to another local maximum near

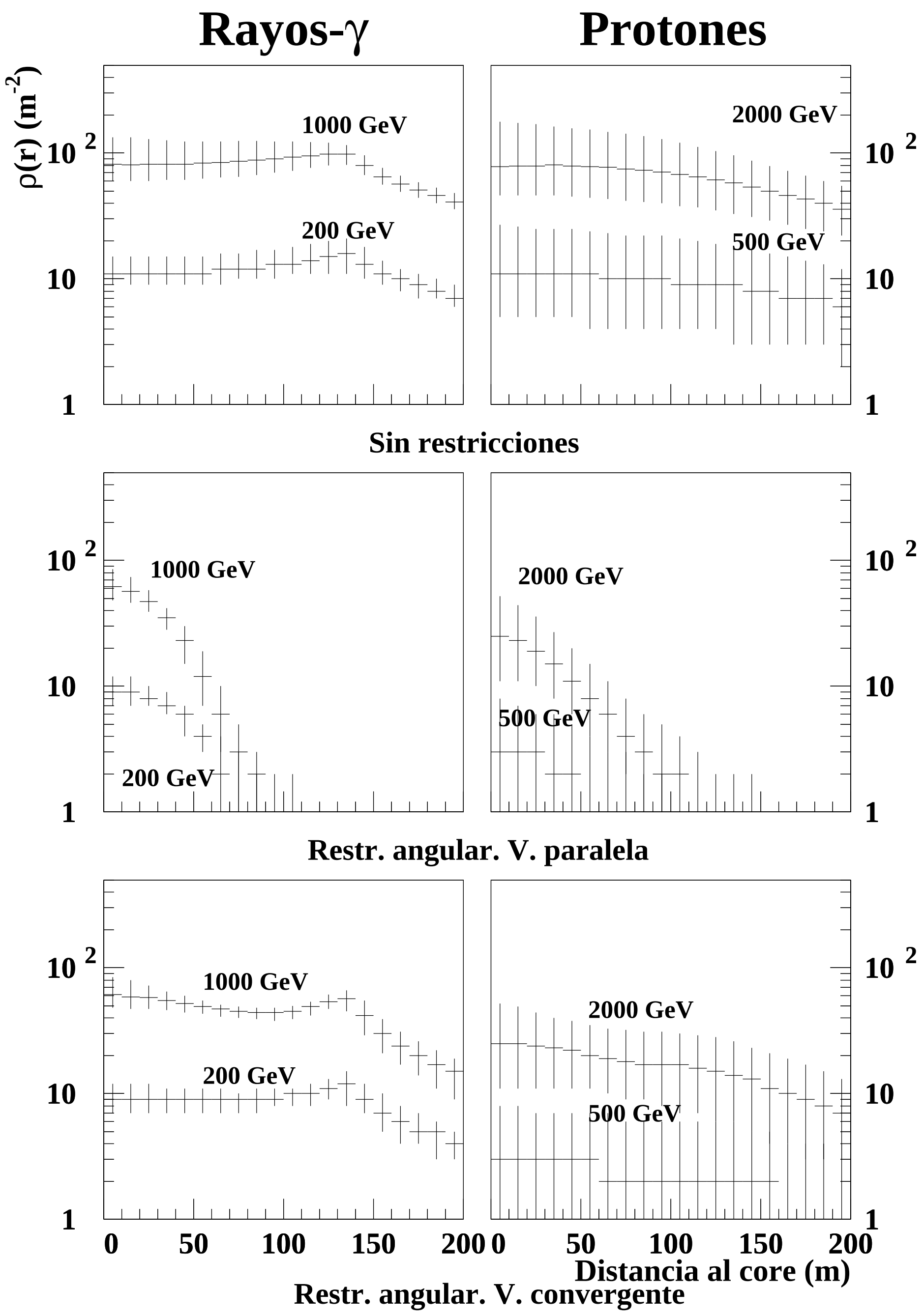

Figure 4.3: *Čerenkov-light distribution, defined as the mean of the Čerenkov-photon density detected at observation level, as a function of the* core *distance. Along with $\rho(r)$, the fluctuations for the three studied configurations are shown (see text for further explanation).*

the *hump*, decreasing again for $r > r_h$. In the post-*hump* region it can be observed that the Čerenkov-photon density decreases with r steeper than in the no-restriction setup. Fluctuations are lower than in the original shower, being minimum at $r \sim 80\,\mathrm{m}$. Proton showers show a similar behavior to the one observed in the no-restriction configuration, and though fluctuations are somewhat smaller, they are still larger than those of γ-showers.

As it has been observed that the Čerenkov-light pattern detected at observation level for showers initiated by γ-rays is significantly different form the one observed for proton showers, being the latter more irregular, a study has been carried out of the **fluctuations observed in each shower** in order to obtain a method to discriminate both primary types.

With this purpose, for each simulated shower the mean number of Čerenkov photons collected by a detector located at $r < 80\,\mathrm{m}$, N_{80} has been calculated. For each one of the detectors we calculate the deviation from this value as:

$$\delta n_i = \left| \frac{N_i - N_{80}}{N_{80}} \right|$$

where N_i is the number of photons collected by a detector. Thus, we obtained for each primary type and energy, the distribution of the values of δn_i for those detectors within $r < 80\,\mathrm{m}$. We define the typical fluctuation in the amount of light collected by one detector as the δn, in such a way that 68% of the distribution is included in the interval $[0, \delta n]$. This value is obtained for each primary type and energy. We have chosen this definition instead of the rms because, due to the large fluctuations observed in the tails of the distributions, the latter parameter shows worse stability to small changes.

The results obtained from these calculi, for the different primary types and energies can be seen in table 4.1 ($r_c = 0$). Results for parallel vision configuration have been excluded, as in the employed formulae it is assumed that N_{80} is a good descriptor of the expected value in each detector, an this is clearly inexact in this configuration, as $\rho(r)$ shows a strong dependence with r.

In this table we can see that in the studied configurations up to now, the value of δn in proton-initiated showers is much larger than in γ-showers, which is expected from the observed Čerenkov-light distributions for both primary types, and that this difference decreases at higher energies. It is observed that fluctuations are smaller in the non-restricted configuration than in the convergent view setup, which is mainly due to the lower number of photons detected in the latter configuration.

With these results it can be expected that we may be able to discriminate the primary type from the study of the Čerenkov-light-density fluctuations, as they are larger in proton-showers. Anyhow we must take into account

Core position	Configuration	γ200	p500	γ1000	p2000
$r_c = 0$	Non-restricted view	0.09	0.34	0.07	0.20
	Convergent view	0.12	0.59	0.16	0.29
	GRAAL	0.42	0.63	0.47	0.51
$r_c < 30\,m$	Convergent view	0.14	0.64	0.24	0.30
	GRAAL	0.41	0.62	0.46	0.49
$r_c < 70\,m$	Convergent view	0.31	0.74	0.35	0.47
	GRAAL	0.42	0.68	0.42	0.50

Table 4.1: *Values of the expected fluctuations for the Čerenkov light collected by individual 40* m^2 *detectors located at a core distance* $r < 80\,m$*. Results are shown for showers with the* core *located near the origin of coordinates (*$r_c = 0$*) and for the more realistic case, with a displaced* core *position (see §4.6). Along with results for the non-restricted view and convergent view configurations, results for the GRAAL configuration are shown (see¡e §4.6.*

that the results obtained for the convergent view configuration have been obtained when the maximum of the shower takes place near the convergence point. In §4.6 a more realistic case will be studied, with the shower axis randomly displaced with respect to the convergence point.

4.2 Longitudinal development

Usually the expression longitudinal development refers to the number of $e^{\pm}$ in a shower as a function of the atmospheric depth (or height a.s.l.). In this work we have studied the number of Čerenkov photons generated in a height interval, and that are detected in each of the studied configurations, as this distributions provides more information about the Čerenkov component. In figures 4.4 and 4.5 it is shown the longitudinal developments of each primary and energy, defining the mean number of Čerenkov photons generated in the height interval j, $\breve{C}(h_j)$ (photons/m), as:

$$\breve{C}(h_j) = \frac{\sum_i^{N_{\rm shw}} \breve{C}_i(h_j)}{N_{\rm shw}}$$

where $N_{\rm shw}$ is the total number of showers, and $\breve{C}_i(h_j)$ is the number of Čerenkov photons generated by shower i in height interval j, and that are detected. This result is obtained for each height interval, and for each primary type, energy and detector configuration. Fluctuations in $\breve{C}(h_j)$ are given by the rms of the $\breve{C}_i(h_j)$ values, calculated for each height interval.

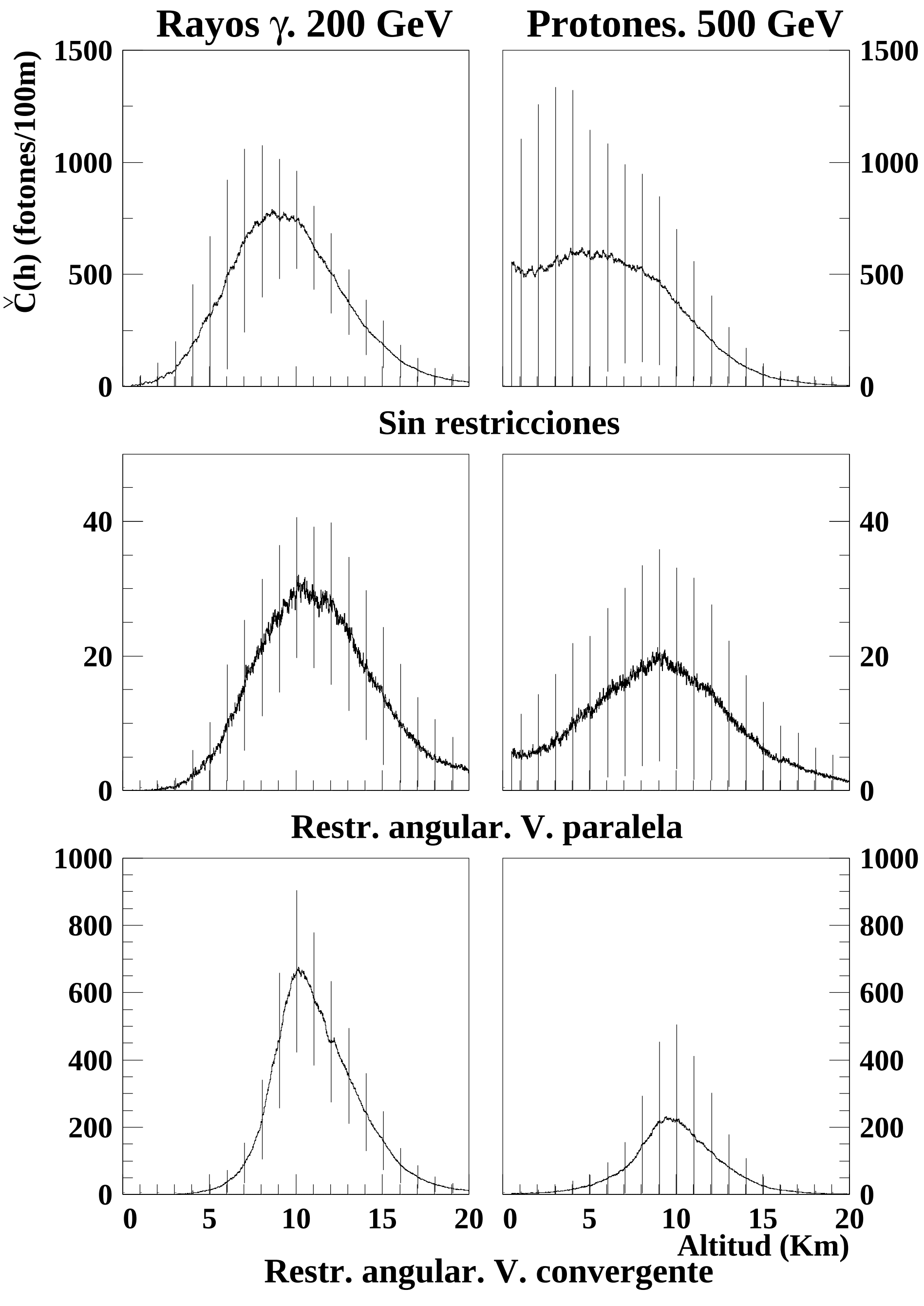

Figure 4.4: *Longitudinal development of 200-GeV γ-rays and 500-GeV protons, defined as the mean number of Čerenkov photons generated in each height interval, and that are detected in each of the three studied configurations (see text).*

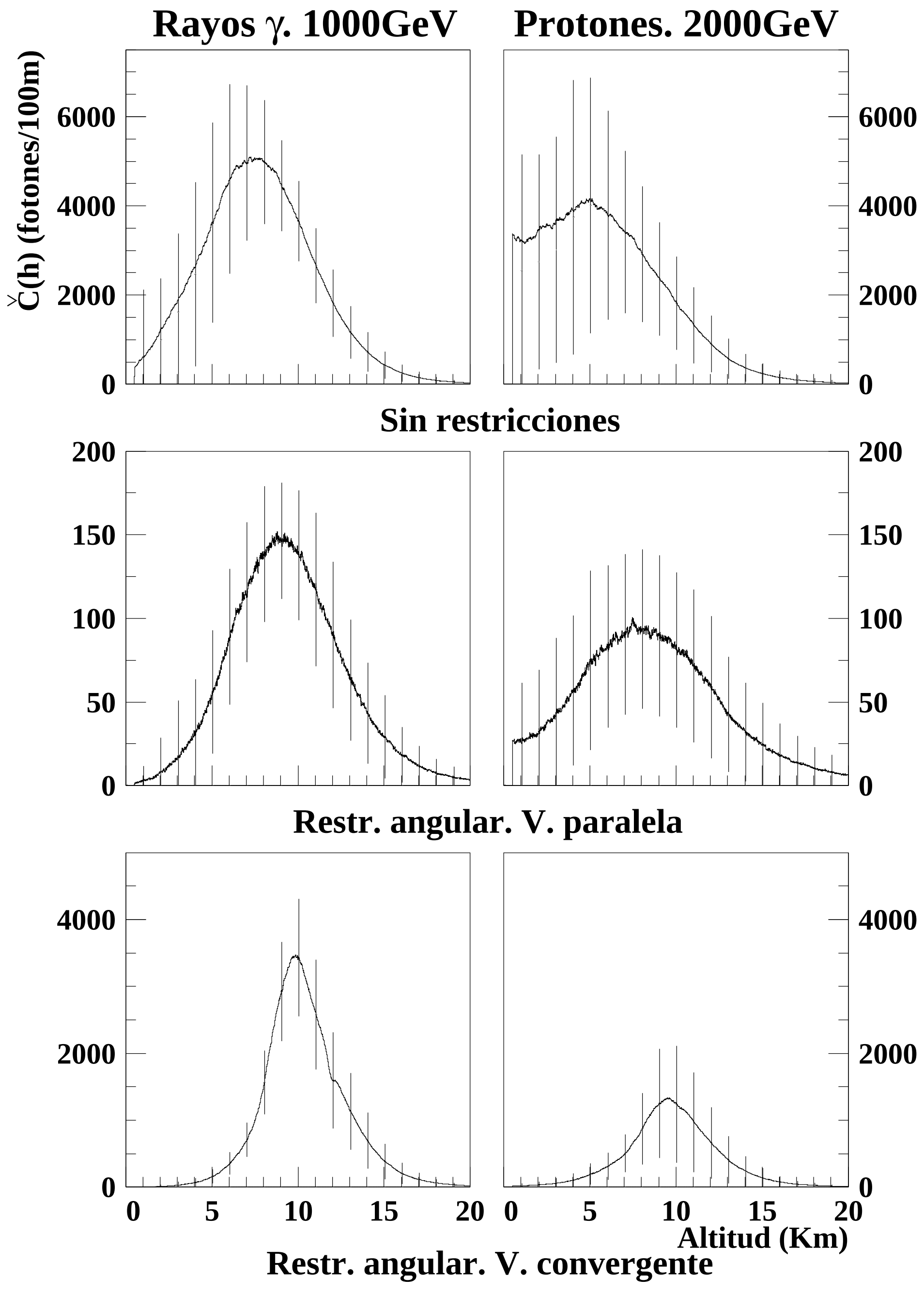

Figure 4.5: *Longitudinal development of 1000-GeV γ-rays and 2000-GeV protons, defined as the mean number of Čerenkov photons generated in each height interval, and that are detected in each of the three studied configurations (see text).*

Each one of the figures shows the results obtained for showers initiated by γ-rays and protons, with three diagrams per primary type, each for one of the configurations, as where previously described.

It can be observed that in the **no-restrictions** configuration, there is a great difference in the shape of the longitudinal development depending on the primary type. γ-showers show a better defined maximum than proton showers. As it is well known, the maximum of the shower, $X_{\max}$, takes place at higher altitudes in γ-showers than in proton showers that generate a similar amount of Čerenkov light, while $X_{\max}$ takes place at lower altitudes for higher primary energies, as was already shown in figure 2.7. It can also be appreciated that the development of γ-showers, in this energy range, takes place mainly in the upper parts of the atmosphere, and seldom are Čerenkov photons generated at observation level. This is not true for proton showers, where a significant amount of Čerenkov light is still produced at low altitudes, event at observation level.

When angular restrictions are introduced, in the **parallel view** configuration, it can be observed that the proportion of detected photons is greatly reduced, specially for photons emitted at lower heights. This is specially clear in proton showers. This is an expected effect, and is in agreement with the results obtained in the lateral distribution of the Čerenkov light. Detectors located near the shower axis detect photons emitted along the axis, while detectors located at larger r almost do not detect any photon, as photons arriving to this large *core* distances, have large incident angles with respect to the shower axis. At lower heights, the lateral development of the shower is greater, and thus the emission angle of Čerenkov photons is bigger (see also [15]), and therefore the detection efficiency is lower for photons generated at lower heights (see §4.4).

In the **convergent view** configuration, as all detectors are aiming to the expected position of the maximum, the detection efficiency is highest for heights around and above the convergence point. For lower heights efficiency decreases rapidly, as this region is outside the field of view of the detectors located farther from the *core*. Therefore the shape of the detected longitudinal development shows a steeper maximum than in the original development, located near the height of the convergence point.This is true for both primary types, which points to the fact that the convergent view technique diminishes the differences between both primary types.

Configuration	γ200	p500	γ1000	p2000
No restriction	9.0±1.6	7.5±3.0	6.9±1.4	6.8±2.4
Parallel view	6.7±2.5	8.3±4.2	4.8±1.8	7.9±3.6
Convergent view	11.0±1.1	11.9±2.7	9.9±1.1	11.3±2.6

Table 4.2: *Mean radii of the adjusted spherical functions to the Čerenkov fronts of each generated shower, as a function of the primary type and energy, for the different studied configurations.*

4.3 Temporal structure of the Čerenkov front

Apart from measuring the amount of Čerenkov light collected by each heliostat, GRAAL measures in a very accurate way the arrival times of the Čerenkov pulses to the different PMT's (and therefore, after a geometrical transformation, to the heliostats). This measurement is done precisely thanks to the fast electronics employed in the experiment. Therefore it is necessary to study the time properties of the Čerenkov front in order to gain the maximum possible knowledge.

For each simulated shower the arrival time, t_i, of each Čerenkov photon to the detectors has been measured. Mean arrival time $\Upsilon(r)$ in the core distance interval $[r_i, r_i + \Delta r]$ is defined for all the simulated showers as the median value of the distribution of t_i for all the photons collected by those detectors whose geometrical center in located within that interval. In the same way as it was done in the fluctuations of the Čerenkov-light density, we define the width of the arrival-time distribution in each distance interval as the intervals to the right $\Delta\Upsilon_{dcha}$ and left $\Delta\Upsilon_{izda}$ of the median, necessary to include 34% percent of the distribution (see figure 4.2). Results for the different primary types and energies are shown in figures 4.6 and 4.7

In the plots corresponding to the **no restriction** configuration, it can be appreciated the general properties of the generated shower. It can be seen that the shape of the front is basically a sphere, and thus can be adjusted to such a function, taken as free parameters the radius and height of the center of the sphere. The most significant parameter is the radius, which depends both of the primary and its energy, as is shown in table 4.2 with the mean values for the radii adjusted to each sphere.

In the Čerenkov front of γ-showers it can be appreciated that the fluctuations in the arrival times (figure 4.6 and 4.7) are relatively independent of the energy of the primary, showing a minimum in the region just before the *hump*. In proton-showers fluctuations are much larger at low energies, though the median front still fits a sphere quite well. In this case fluctuations are much smaller for higher energy showers, though always larger than those observed in γ-showers.

In the second configuration, with the detectors in **parallel view**, the spherical shape of the front remains, though the adjusted radii are reduced in γ-rays and increase in proton showers. This fact is due to the differences in the longitudinal and lateral development between both types of showers. In this configuration, photons from γ-showers detected far away from the *core*, are generated by particles that have suffered several scatterings, mainly in the last stages of the shower, and therefore arrive later, producing a larger curvature in the shower front (see figures 4.8 – 4.11). On the other hand, in proton showers, and due mainly t the larger transverse momentum of hadronic interactions that increase the lateral spread, and to the branching of the main shower, it is possible to detect photons at large r with small delays with respect to those photons detected near the shower axis. That is why the detected Čerenkov front shows a smaller curvature.

In this configuration, for γ showers, fluctuations near the *core*, are smaller that in the original shower, but at distances larger than $\sim$70 m increase significantly. This can be easily explained if we take into account that those photons originated by particles that have undergone great scattering are the ones arriving with larger delays. The restricted field of view eliminates those photons, thus reducing fluctuations. On the other hand, observing the lateral distribution for this configuration, we can appreciate that for *core* distances larger that $\sim$80 m the light density of detected photons is very small. Therefore fluctuations in the arrival time increase due to the lack of statistics. Moreover, detected photons must be emitted by particle suffering a great scattering, increasing the imprecision of the shower front. In the same way this effect takes place in proton showers. For this primary type, a low energies fluctuations at $r \approx 0$ are greatly reduced, though they are still quite large at $r \gtrsim 90$ m, and the cause is the same of γ-rays. At larger energies the behavior is similar, though in general fluctuations are smaller.

In the third configuration, with the detectors aiming in **convergent view**, the detected shower-front shape is modified, with larger radii for all primary types and energies. Moreover, it can be observed that fluctuations in the shower front are very similar for all primaries and energies. This fact corroborates what we already observed in the longitudinal developments of the detected Čerenkov photons in this configuration (figures 4.4 and 4.5): the mean emission height of the detected photons is higher than in the other two configurations, which yields a larger curvature, and the maximum takes place at similar heights for all primaries and energies, giving similar curvatures of

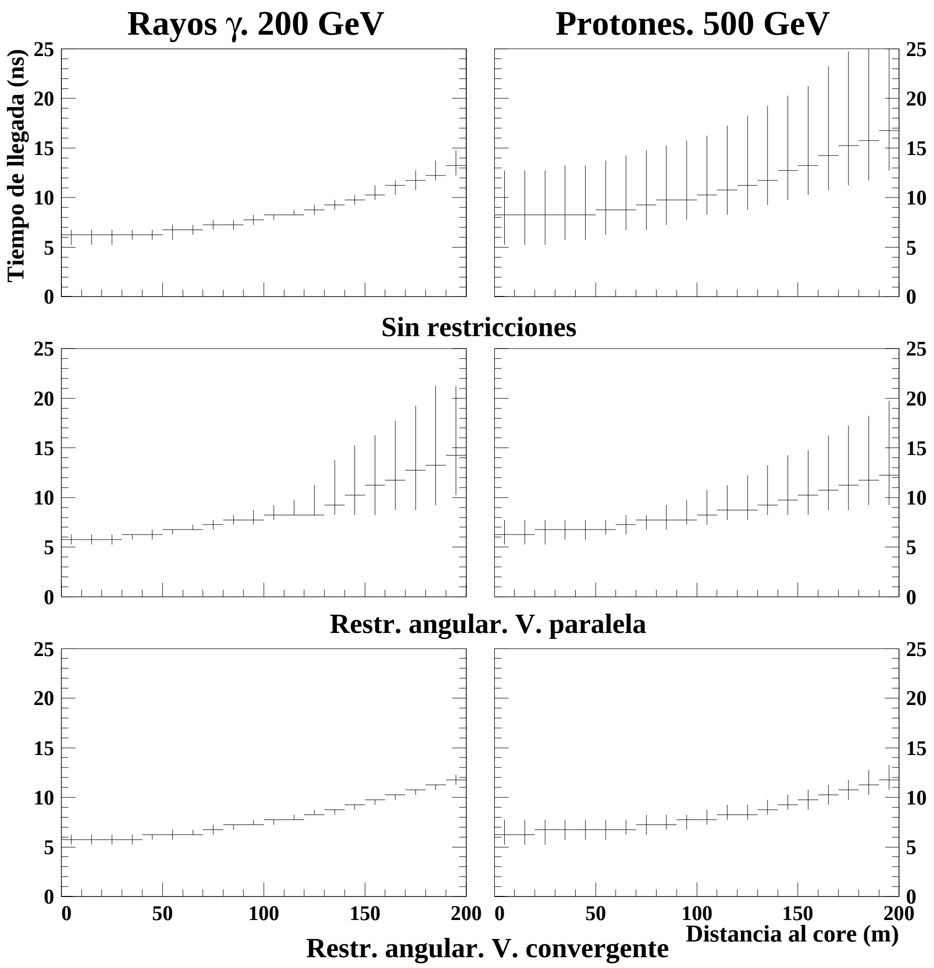

Figure 4.6: *Arrival times $\Upsilon(r)$ of the Čerenkov front as a function of* core *distance, defined by the median of the distribution of the arrival times of the photons detected in each distance interval. Results are shown for showers initiated by 200 GeV γ-rays and 500 GeV protons, in the three studied configurations.*

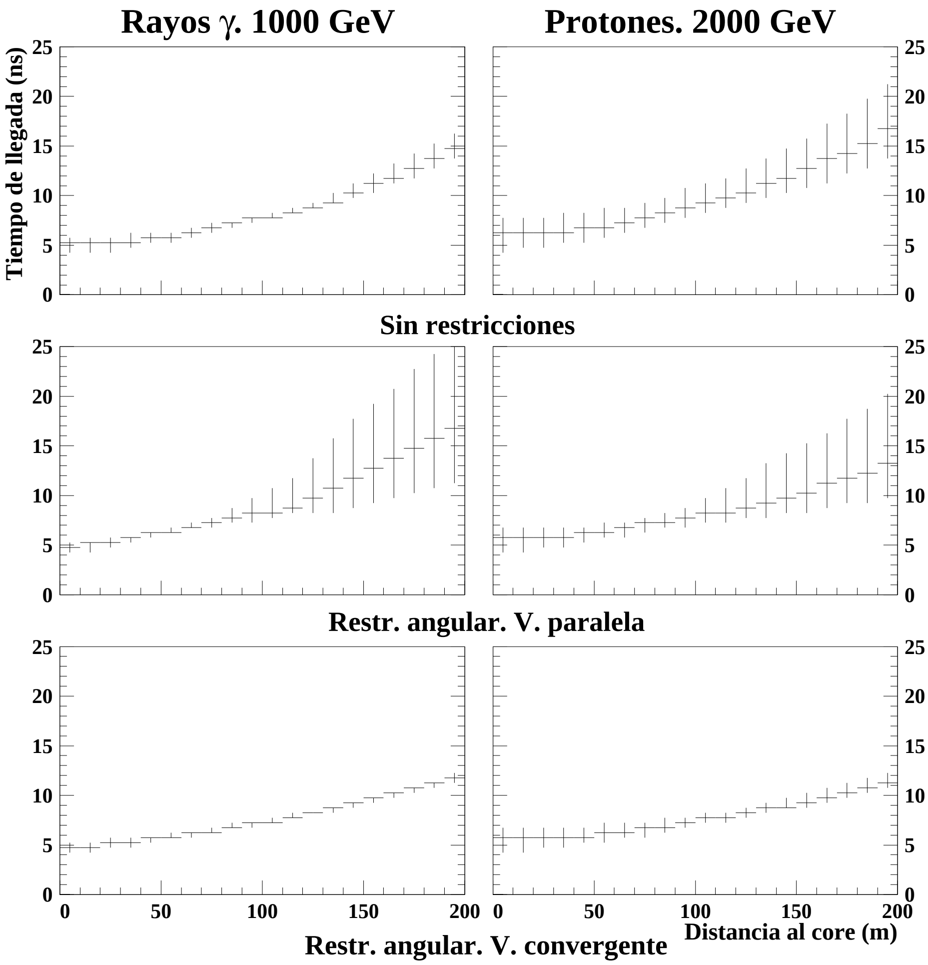

Figure 4.7: *Arrival times $\Upsilon(r)$ of the Čerenkov front as a function of* core *distance, defined by the median of the distribution of the arrival times of the photons detected in each distance interval. Results are shown for showers initiated by 1000 GeV γ-rays and 2000 GeV protons, in the three studied configurations.*

the shower front.

As we have already mentioned, in this configuration, fluctuations for all primary types and energies are greatly reduced, to values lower than those of the original shower, even for detectors located far away from the *core*, with the lowest fluctuations located near the *hump*. This results corroborate the simple model formulated in the previous section, where it was said that detectors in this configuration collect Čerenkov photons generated in the central and upper part of the atmosphere, where the lateral spread of the charged particles is still small. In that case it is expected that fluctuations are reduced, as photons from particles that have suffered great scattering are not detected (located mainly in the lower part of the atmosphere). The curvature radius of the front increases, as detected light comes from the upper parts of the shower. In this configuration fluctuations at large distances from the *core* do not increase significantly due to the lack of statistics, as the number of detected photons is still high, thanks to the convergent view.

In this case we can define **fluctuations observed inside a given shower**, in order to study the possibilities to obtained a discrimination method of the primary type. We will compare the mean arrival time of the Čerenkov pulse to each one of the detectors,t_i, with the mean arrival time, for that shower, at the *core* distance at which the detector is located, $t(r_i)$, as:

$$\delta t_i = |t_i - t(r_i)|$$

We can define the typical value of the fluctuations in the arrival times of the Čerenkov front, δt, through the distribution of δt_i, for all detectors located at a *core* distance lower than 80 m for each primary type and energy, as the value δt such that 68% of events of the distribution are included in the interval $[0, \delta t]$. Results obtained for the different primary types and studied configurations are shown in table 4.3 ($r_c = 0$).

From the results shown in this table, for the studied configurations, it should be highlighted the great decrement in the values of δt observed in proton showers with a restricted field of view. While in showers detected without restrictions, δt fluctuations are much larger in protons than in γ-rays, decreasing this difference with larger energies of the primary, when an angular restriction id introduced, even in parallel view, while fluctuations in γ-rays are not modified, those observed in protons are greatly reduced. In convergent view, there are no changes in γ-rays, but protons are modified, as the value of δt slightly decreases with respect to the previous configuration. Therefore it can be appreciated that a method based on the time fluctuations δt would be hampered due to the restricted field of view of the detectors.

Core position	Configuration	γ200	p500	γ1000	p2000
$r_c = 0$	Non-restricted view	0.19	2.31	0.19	0.94
	Parallel view	0.19	0.69	0.19	0.44
	Convergent view	0.19	0.44	0.19	0.31
	GRAAL	0.69	0.81	0.64	0.69
$r_c < 30\,\mathrm{m}$	Convergent view	0.44	0.56	0.56	0.56
	GRAAL	0.69	0.81	0.68	0.68
$r_c < 70\,\mathrm{m}$	Convergent view	0.94	0.94	1.10	0.94
	GRAAL	0.69	0.92	0.72	0.72

Table 4.3: *Values for the expected fluctuations in the arrival times of the Čerenkov front to the detectors locates at a distance r from the origin of coordinates lower than 80 m, for the different primaries and energies. There are shown results for the case when the* core *is located in the origin of coordinates ($r_c = 0$), and for the more realistic case with the* core *displaced (see §4.6). Non-restricted, parallel and convergent view configurations are described in the Čerenkov-front study (§4.3), while GRAAL configuration is described in §4.6. In the latter case, fluctuations have been obtained in slightly different way.*

4.4 Production height and arrival time of Čerenkov photons

In the previous section we have related the time structure of the Čerenkov front and its fluctuations with the production height of the Čerenkov photons. Figures 4.8, 4.9, 4.10 and 4.11 show for the three considered configurations the distribution of arrival times of Čerenkov photons to the observation level as a function of the production height of the photon. Each figure corresponds to a different primary and energy. Notice the logarithmic scale. For each figure and configuration three plots are shown, depending on the distance of the detectors to the *core*: (a) for detectors located in the pre-*hump* region ($r < 80\,\mathrm{m}$), (b) for detectors located in the *hump* region ($80 < r < 140\,\mathrm{m}$), and (c) for detectors located in the post-*hump* region ($r > 140\,\mathrm{m}$). The plots show the result of adding the data of all the generated showers for that primary and energy.

Let's consider first the properties of the generated shower **without angular restrictions**. As expected, proton showers show a larger spread in the arrival times than γ-showers in the three considered regions, and this broadening is even bigger farther from the *core*. In the region near the *core* there is an almost linear relationship between the mean arrival time and the

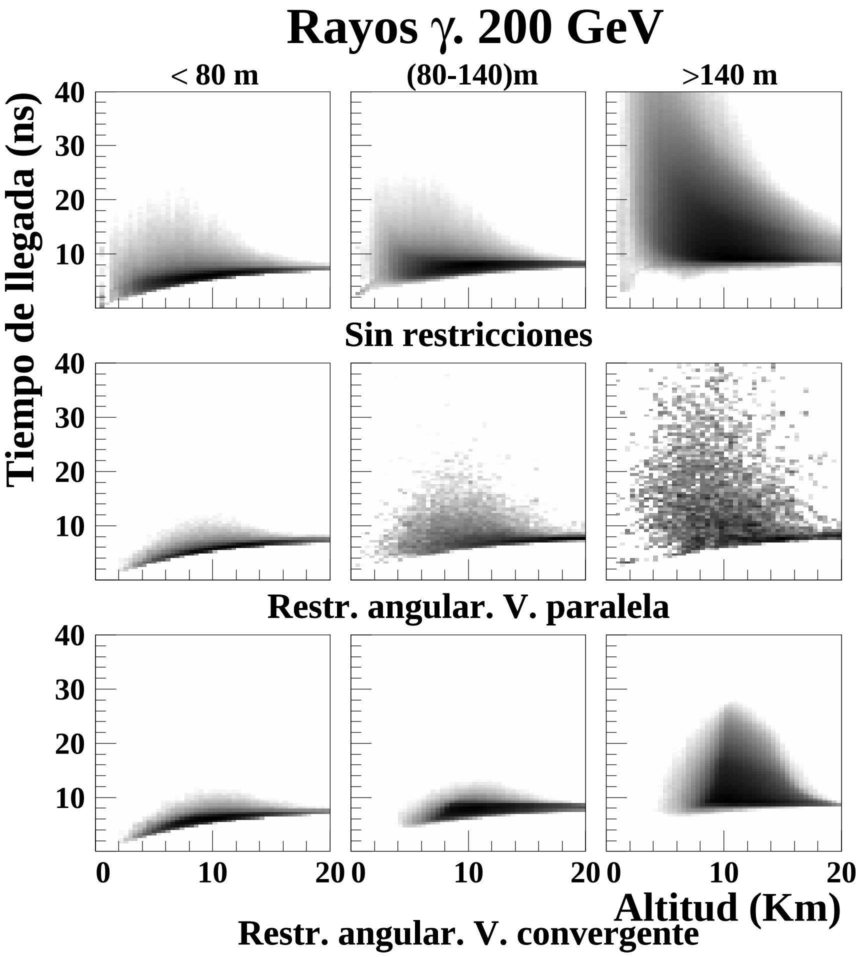

Figure 4.8: *Distribution of Čerenkovphoton arrival times as a function of generation height for 200-GeV γ-showers. Color intensity indicates, in logarithmic scale, the number of photons coming from a given height interval at the considered arrival time interval. Each column corresponds to a different* core-*distance range: pre-*hump, hump *and post-*hump *region. Each row corresponds to one of the considered experimental setups.*

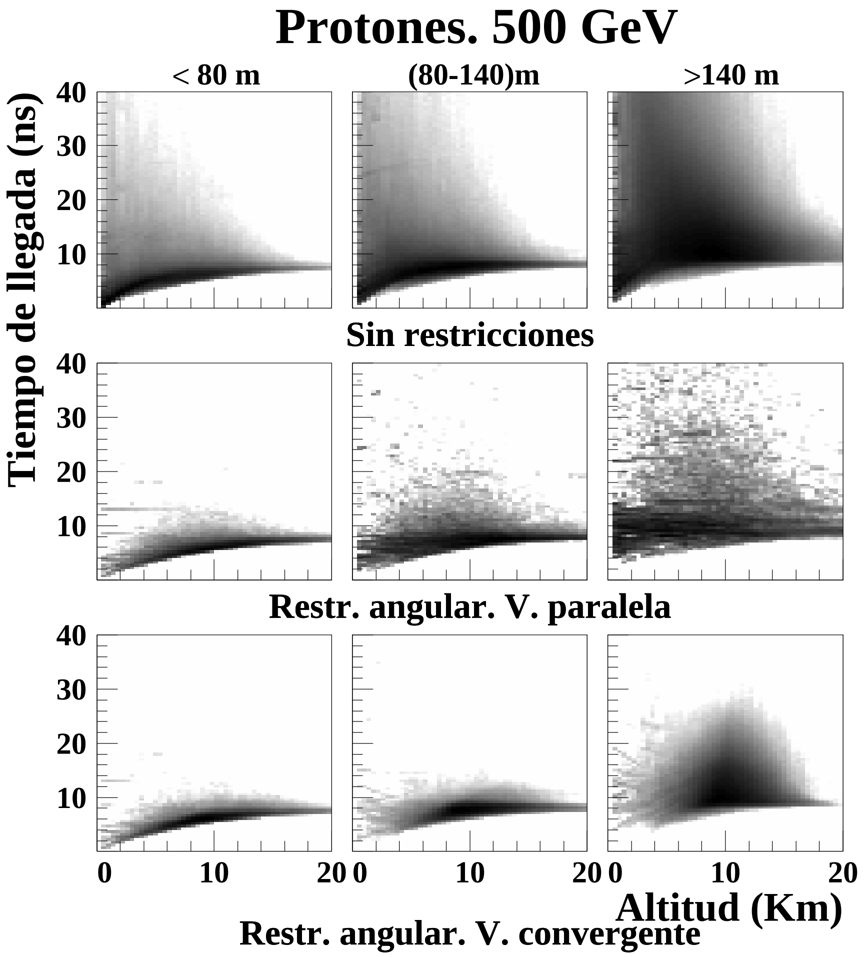

Figure 4.9: *Distribution of Čerenkovphoton arrival times as a function of generation height for 500-GeV proton showers. Color intensity indicates, in logarithmic scale, the number of photons coming from a given height interval at the considered arrival time interval. Each column corresponds to a different* core-*distance range: pre-*hump, hump *and post-*hump *region. Each row corresponds to one of the considered experimental setups.*

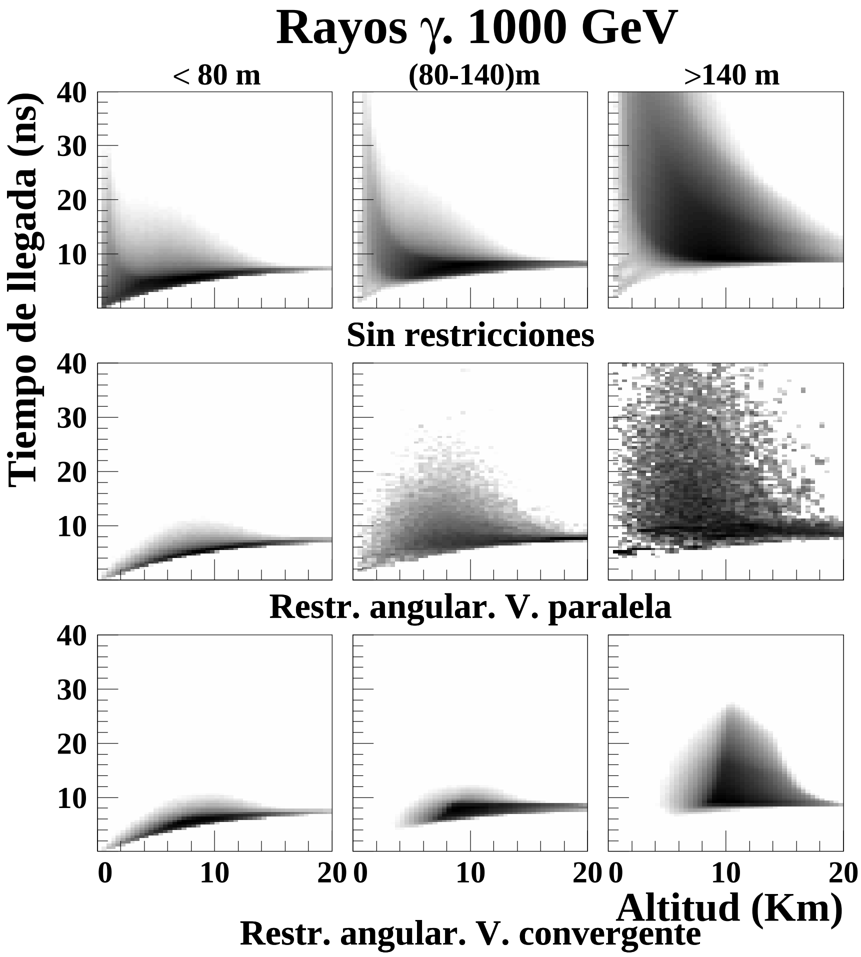

Figure 4.10: *Distribution of Čerenkovphoton arrival times as a function of generation height for 1000-GeV γ-showers. Color intensity indicates, in logarithmic scale, the number of photons coming from a given height interval at the considered arrival time interval. Each column corresponds to a different* core-*distance range: pre-*hump, hump *and post-*hump *region. Each row corresponds to one of the considered experimental setups.*

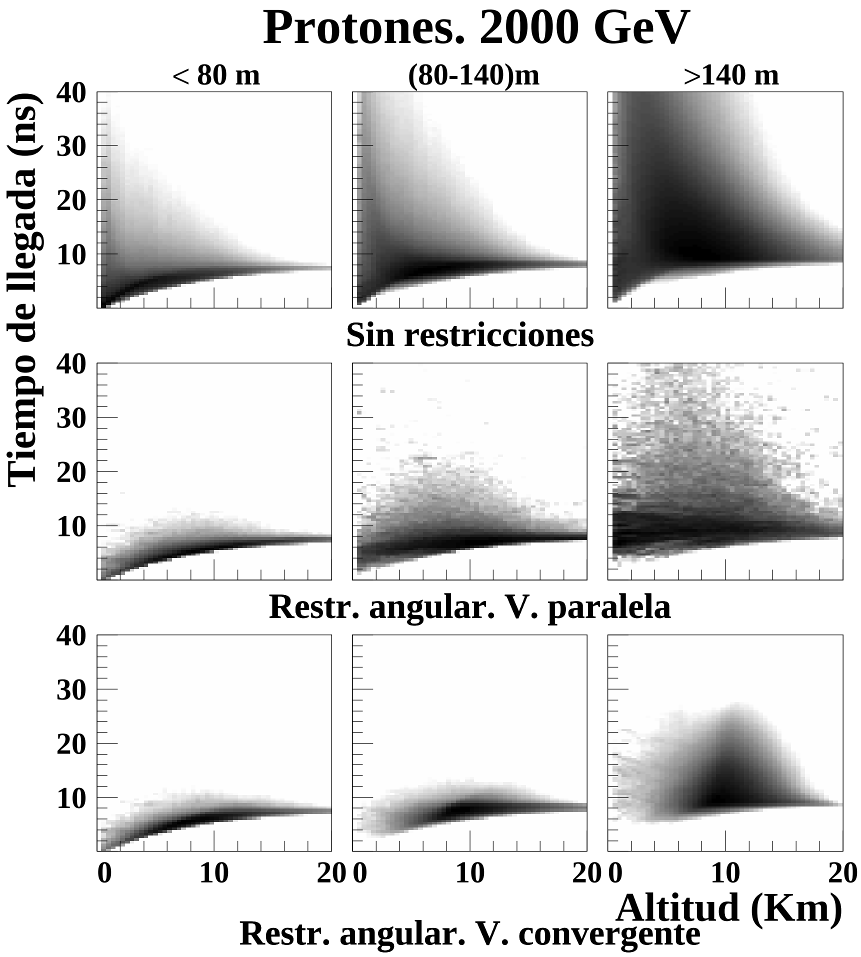

Figure 4.11: *Distribution of Čerenkovphoton arrival times as a function of generation height for 2000-GeV proton showers. Color intensity indicates, in logarithmic scale, the number of photons coming from a given height interval at the considered arrival time interval. Each column corresponds to a different* core-*distance range: pre*-hump, hump *and post*-hump *region. Each row corresponds to one of the considered experimental setups.*

production height, with Čerenkov photons generated low in the atmosphere arriving earlier than those generated in the upper part of the shower. Proton showers show this behavior in the three studied regions. But in γ-showers this relationship changes with the distance to the *core*. This difference is greatest in the post-*hump* region. While in γ-showers photons generated in the central and upper part of the shower are the ones to be detected earlier, in proton showers, though most of the detected photons come from the central part, a significant fraction come from the lowest parts, being detected at early times. These photons arrive around 1 ns after the first photon is detected near the shower axis. These photons must come from charged particles that, even in the post-*hump* region, reach low altitudes without suffering important scattering. This is possible in proton showers, where branching of the main shower is not unusual. These branches show a similar development to that of the main shower, but with its axis located far from the *core*.

In the **parallel view** configuration it can be appreciated that those photons arriving late with respect to the mean pulse, have a low detection probability in all regions, and for all primaries. Therefore the time spread of the pulse is reduced, as photons coming from particles that have suffered a great scattering, and therefore, due to the longer trajectories, arrive late with respect to the main pulse, are not detected. In any case, the behavior of the mean arrival time as a function of the generation height is similar to the one observed in the previous case. In the post-*hump* region statistics are very poor due to the lack of detected Čerenkov photons, specially in low energy showers, as they are smaller.

With the detectors in **convergent view**, those effects observed in the previous setup are remarked. Taking into account that the convergent view aims the detectors at a height of approximately 11 Km, most of the detected photons come from heights around or above that height. Due to the restricted field of view of 0.3 degrees halfwidth, the lower limit observed by the detectors is around 8 Km, with a very low detection efficiency bellow that height, as can be observed from the plots, specially in the post-*hump* region. It can be remarked the great resemblance among the plots obtained for γ-rays and protons in this configuration.

We can conclude that photons generated at low altitudes usually arrive with larger incidence angles than those generated at larger heights. This means a larger scattering in the arrival time. This effect is most important for detectors located at large *core* distances. When important angular restrictions are imposed on the detection of the Čerenkov component, most of the photons generated at low altitude are rejected, specially those with long delays (i.e. those emitted by particles with large angular scattering), and

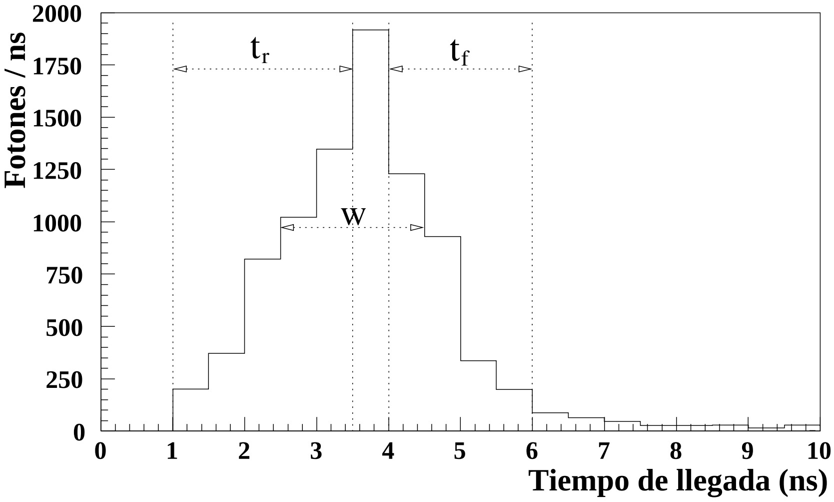

Figure 4.12: *Scheme of the shape parameters obtained from a Čerenkov pulse.*

therefore the temporal scattering is reduced. We can see then that angular restrictions diminish fluctuations in the arrival times of detected Čerenkov photons, reducing the possible γ-hadron separation.

4.5 Shape of the Čerenkov pulses

Another shower observable is the shape of the detected Čerenkov pulses. In order to accomplish this study we will analyze the signal collected by each one of the detectors, which are assumed almost ideal. The only instrumental effect that is been considered is the mirror area ($40\,\mathrm{m}^2$). The electronic odes not introduce any alteration in the shape of the pulses. The detection efficiency is 100% and no background noise has been taken into account.

As a first approximation we adjusted each one of the detected Čerenkov pulses to a lognormal function, which, according to [16] fits better than other functions, as for example the Γ function. This approximation was rejected as the results were not as good as expected, and the calculi of the shape of the pulse was carried out directly from the detected time distribution, is shown in figure 4.12. For each pulse we calculate the full width at half maximum (FWHM) w, rise time t_r (time interval needed for the signal to go from 10% to 90% of the maximum), and fall time t_f (time interval needed for the signal to go from 90% to 10% of the maximum).

In order to study the possibility to use these observables, both in the positioning of the *core* position, and in the determination of the type and energy of the primary, we show in figures 4.13, 4.14 and 4.15 the mean values for the different parameters, measured in all the detectors of all the generated showers, as a function of the *core* distance for the different configurations, for showers initiated by 200-GeV γ-rays and 500-GeV protons. Error bars correspond to the rms of the distributions of the parameters in the distance interval.

It can be observed that the behavior of the three parameters is almost invariant with the change of observing configuration. The main differences correspond to the parallel-view configuration, in which very large errors are observed at core distances farther than $\sim$80 m. Once again this is due to the very poor statistics at this large core distances for this configuration. In any case we can assert that the dependency of the detected pulse shape with core distance is very similar in both the original shower and the convergent view configuration, with fluctuations somewhat, but not significantly, smaller in the latter.

It is also evident that the behavior dependency with core distance is different depending on the type of primary. In γ-initiated showers the values of the considered parameters fall with core distance, up to the *hump* region. In the post-hump region all the parameters increase, indicating broader pulses. This behavior is quite marked in the fall time of the pulses, but much smaller in the FWHM and rise time, which indicates that the modification of the pulse shape is due to longer tails, there are a larger number of photons arriving with delays with respect to the position of the pulse maximum. On the other hand, for proton showers, it can be seen a behavior almost constant of the parameters. Parameters are almost independent from the *core* distance, with a slight tendency to increase with r. As expected, fluctuations in γ-showers are smaller than in proton showers.

For larger-energy showers, results are similar, though parameter fluctuations are smaller, and pulses are slightly broader. In figure 4.16 we can observe the results obtained for convergent view configuration. We should remark the behavior of γ-showers near the *hump*, where fluctuations in the pulse width are greatly reduced, and that the dependence of t_f with *core* distance is stronger. On the other hand, fluctuations in proton shower are significantly reduced, and start to show a behavior similar to that of γ-rays.

We can conclude for these results that, under the conditions of this study (almost ideal detectors with a 100% efficiency, completely covering an area of $300\times300\,\mathrm{m}^2$, with the maximum of the shower near the convergent point), it is possible to observe a dependency of the pulse shape with the primary type and the *core* distance, though the latter is only possible in γ-showers. In any case, a great temporal resolution is needed to observe these dependen-

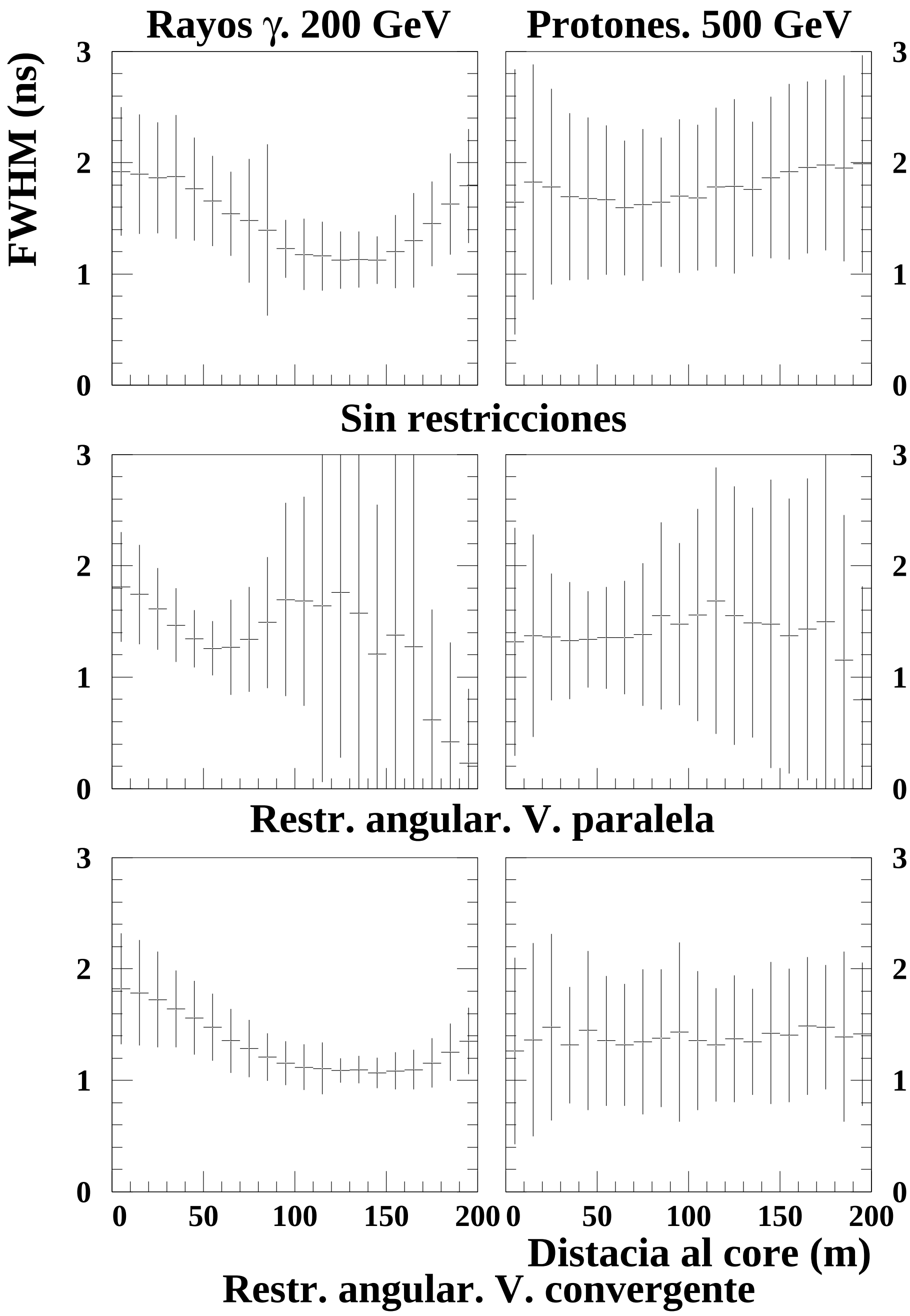

Figure 4.13: *FWHM of the detected Čerenkov pulses, as a function of the heliostat-*core *distance. the mean value is obtained form the pulses collected in all detectors in a area of 300×300* m^2, *for showers generated in vertical incidence, and* core *located on the projection of the convergence point. Error bars correspond to the rms of the obtained-values distribution in the distance interval considered. In this plots results for showers initiated by 200-GeV γ-rays and 500-GeV protons are shown, in the three described configurations.*

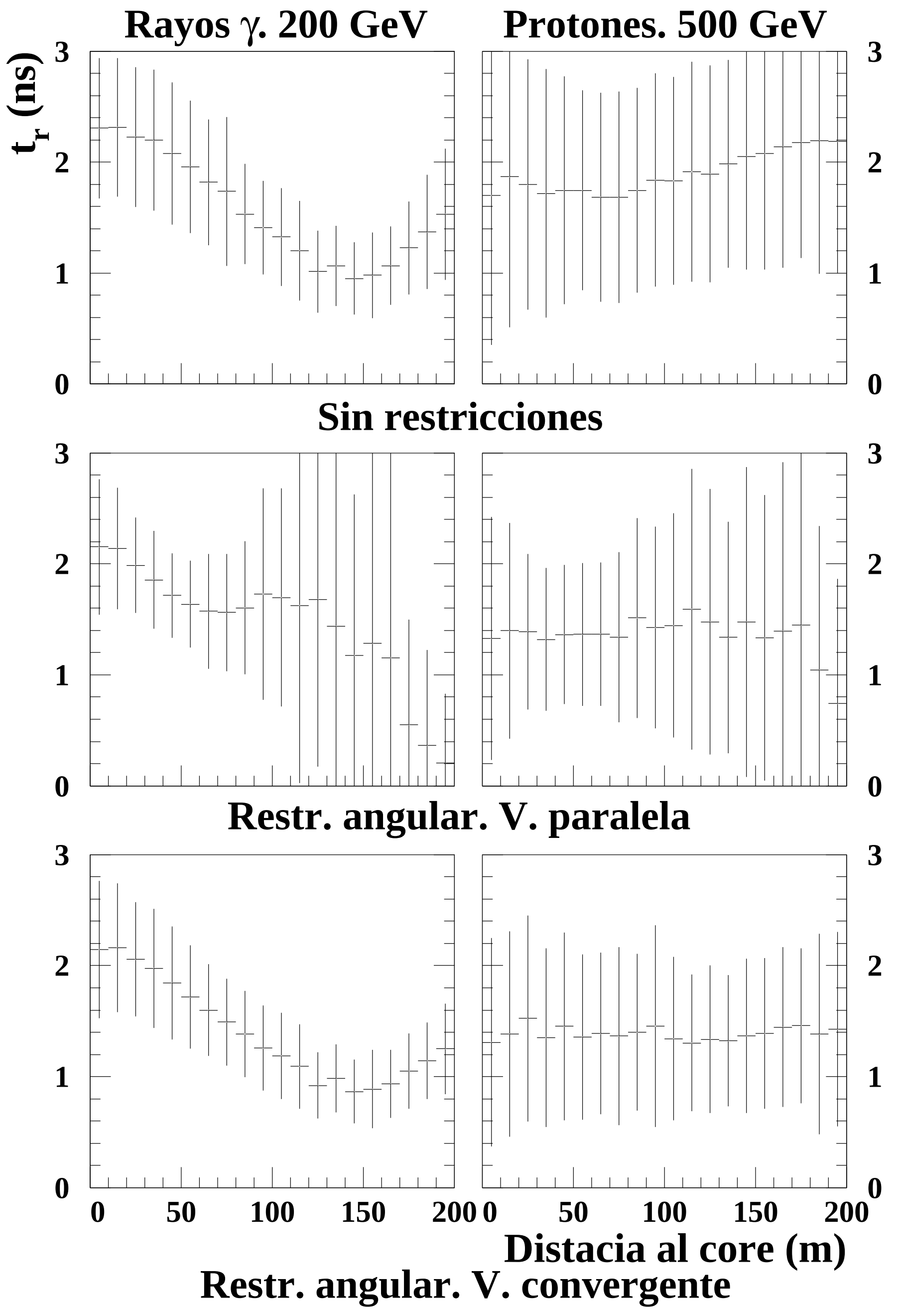

Figure 4.14: *Rise time (10%–90%) of the detected Čerenkov pulses (t_r) as a function of the heliostat-*core *distance. the mean value is obtained form the pulses collected in all detectors in a area of 300×300 m^2, for showers generated in vertical incidence, and* core *located on the projection of the convergence point. Error bars correspond to the rms of the obtained-values distribution in the distance interval considered. In this plots results for showers initiated by 200-GeV γ-rays and 500-GeV protons are shown, in the three described configurations.*

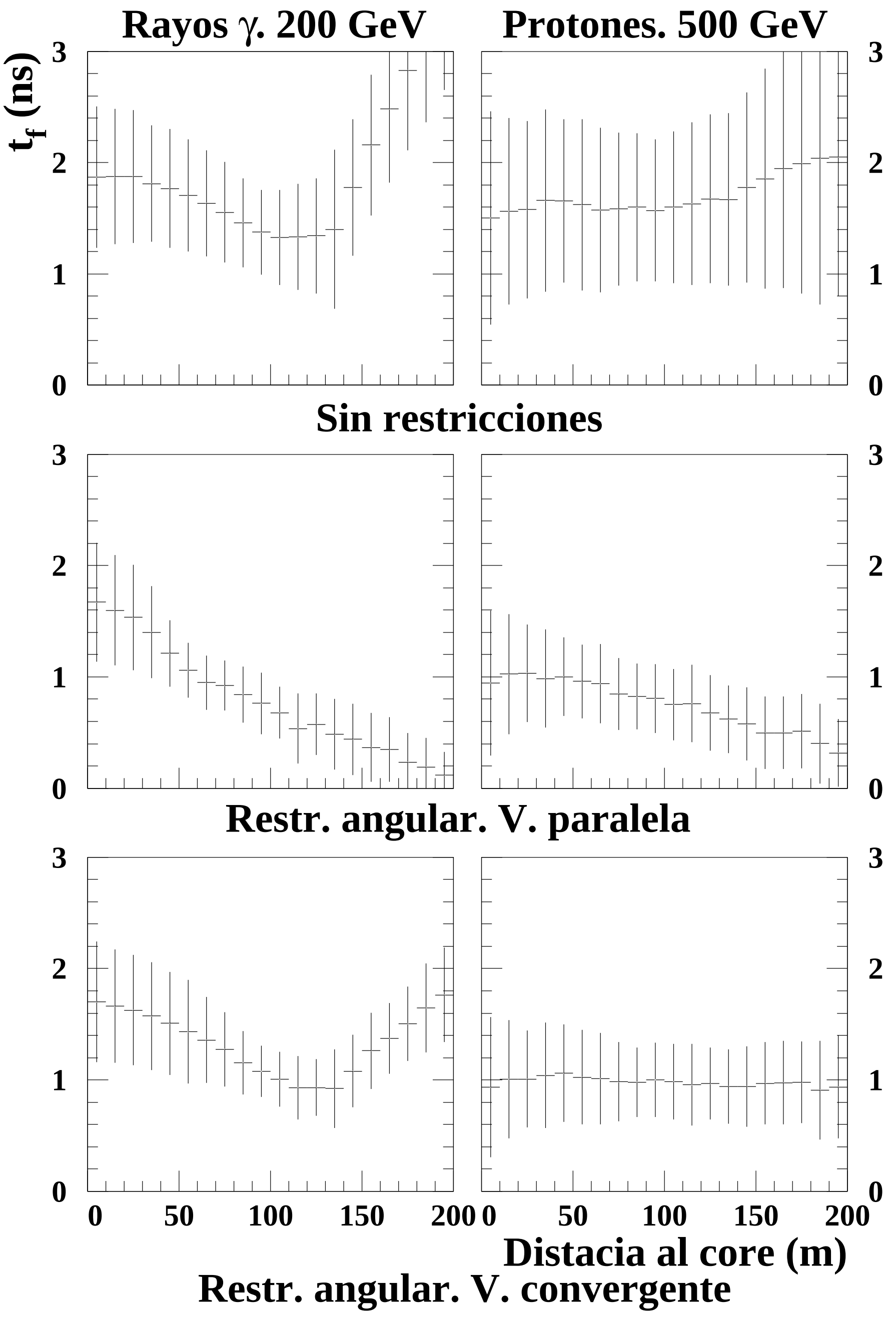

Figure 4.15: *Fall time (90%–10%) of the detected Čerenkov pulses (t_r) as a function of the heliostat-*core *distance. The mean value is obtained form the pulses collected in all detectors in a area of 300×300* m^2*, for showers generated in vertical incidence, and* core *located on the projection of the convergence point. Error bars correspond to the rms of the obtained-values distribution in the distance interval considered. In this plots results for showers initiated by 200-GeV* γ*-rays and 500-GeV protons are shown, in the three described configurations.*

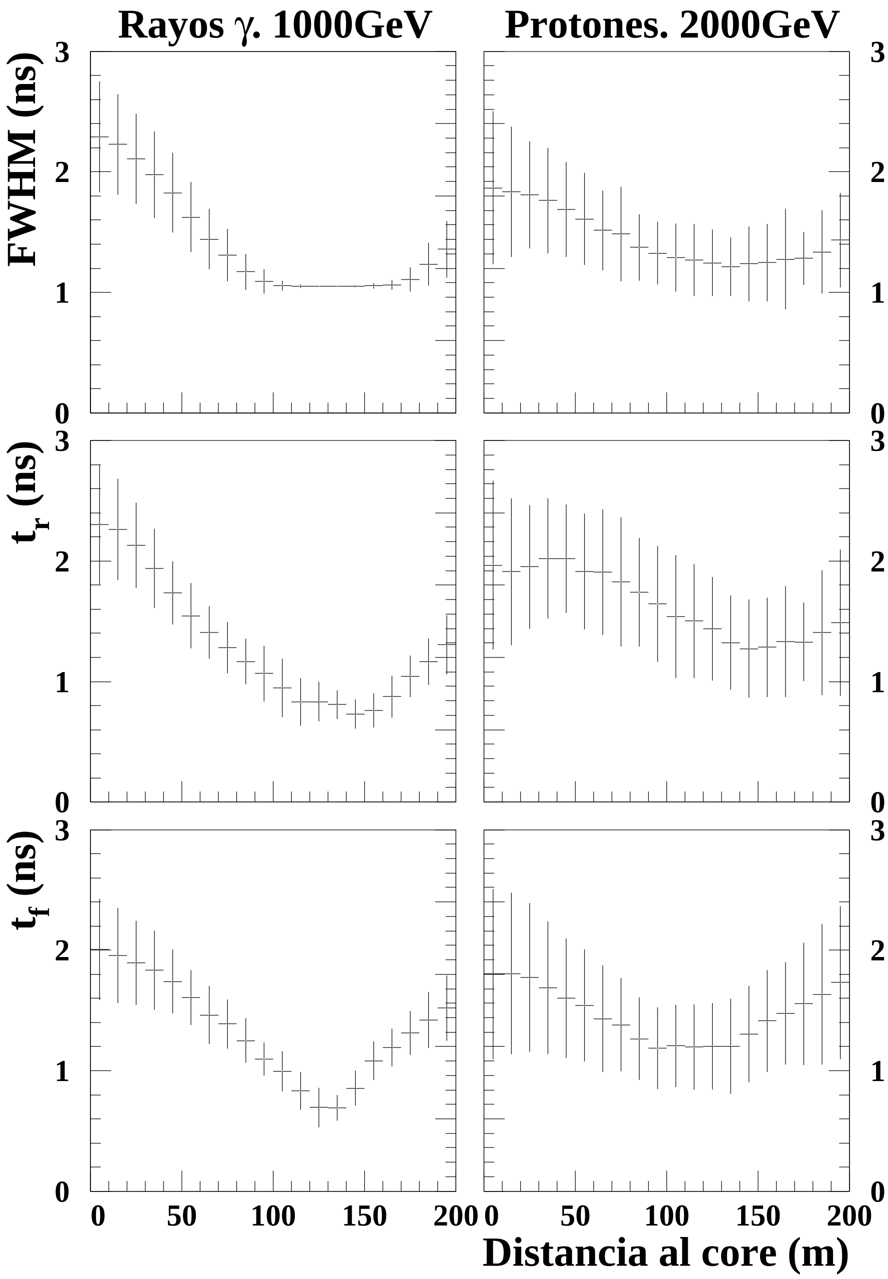

Figure 4.16: *Dependence of the shape parameters of the detected Čerenkov pulses in the* **convergent view** *configuration. The mean value is obtained form the pulses collected in all detectors in a area of 300×300* m^2*, for showers generated in vertical incidence, and* core *located on the projection of the convergence point. Error bars correspond to the rms of the obtained-values distribution in the distance interval considered. In this plots results for showers initiated by 200-GeV* γ*-rays and 500-GeV protons are shown, in the three described configurations.*

cies, which is almost impossible to achieve in any present-day experiment. On the other hand, with larger primary energies, the behavior of proton-showers resembles that of γ-rays, and therefore, the possibility to accomplish an effective discrimination among both primary types decreases.

4.6 Random *core* position and limited sampling

In figure 4.17 the light distribution on the ground for a 200-GeV γ-shower and a 500-GeV proton with vertical incidence and with the *core* randomly displaced from he vertical projection of the convergence point, H. As expected, neither the non-restricted nor the parallel view configuration show significant differences from the distributions shown in 4.1. There is only a displacement of the center of gravity of the distributions. That's not the case of the convergent view configuration, which shows important differences with respect to the case were the *core* is located near H (fig. 4.1), where the light distribution was very similar to the one detected in the non-restricted configuration. In the present case, the light distribution shows important differences, specially in the γ-ray. The light distribution shows larger fluctuations, which is due to the fact that the Čerenkov-photon detection efficiency of each detector depends on the orientation of its optical axis with the shower axis. The radial structure that dominated the light distribution is not so clearly seen. For example, the *ring* is not fully detected (only segments). The case shown corresponds to a displacement of 40 m of the *core*. For large displacements the modifications in the distributions are more important, losing completely the radial symmetry.

This example clearly shows that in the realistic case where the *core* position is randomly distributed, the results given in the previous sections can not be fully applied. In order to study this effect quantitatively, we have generated 150 showers of each primary type and energy, with the *core* randomly located within a radius of 80 m around H. The other characteristics are kept constant with respect to the showers employed in the previous sections.

As in the previous chapters we will study the fluctuations in the amount of Čerenkov light collected by each detector from a given shower, δn, and the time fluctuations δt. Both parameters are defined in the same way as it was before, and are calculated for detectors located at less than 80 m from H. In this moment we must take into account that the probability to detect a shower is not independent of the distance *core*–H. As is shown in the

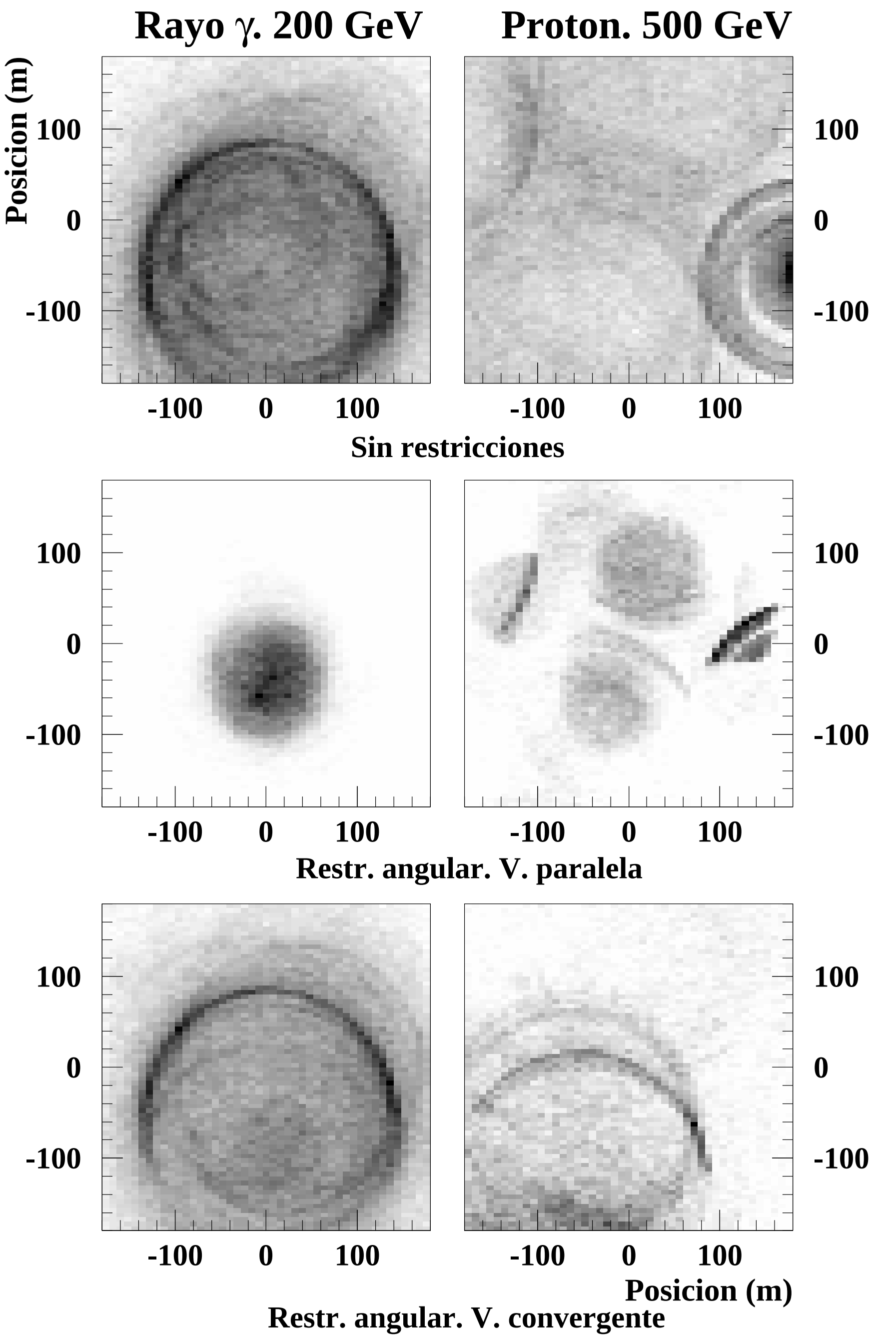

Figure 4.17: *Typical Čerenkov-light distributions detected at observation level (505 m a.s.l.). Showers were generated by a γ ray and a proton with vertical incidence, and the core displaced from the convergence point. Results for the three configurations described in the text are shown.*

next chapter, from the effective area plots we can estimate that the low energy showers here simulated have a detection probability almost zero for $r_c \gtrsim 30\,\mathrm{m}$. In the same way, for larger energies, the maximum radius is larger $r_c \lesssim 70\,\mathrm{m}$. Results are shown in tables 4.1 and 4.3 under entries $r_c < 30\,\mathrm{m}$ and $r_c < 70\,\mathrm{m}$.

Form the results shown in table 4.1 for the fluctuations in the detected Čerenkov light, δn, it can be inferred that at low energies, and with both radial limits, it is possible to discriminate between both primary types from the observation of this parameter, but at higher energies the differences attenuate and the method would not be so good. On the other hand, in table 4.3 where the fluctuations of the arrival times of Čerenkov photons to the different detectors, δt, it can be appreciated that the values for γ-showers increase to values comparable to those of proton showers. It can be concluded that the observation of the fluctuations in the arrival time of the Čerenkov front to the different detectors is very improbable to give a good discrimination method.

In the same manner it is possible to study the modifications that a random *core* position introduces in the **Čerenkov-pulse shape**, and observe the dependency of the shape parameters with the primary type and energy, and the distance detector–*core*, under the new conditions. In figures 4.18 and 4.19 it is shown the mean value of FWHM, rise time t_r, and fall time t_f in the convergent view configuration. The maximum distance from the *core* to H point id limited at low energies to $r < 30\,\mathrm{m}$, and at high energies to $r < 70\,\mathrm{m}$. The definitions of the mean values and fluctuations are the same ones as described in section 4.5.

It can be appreciated that in both energy ranges the behavior is not much different from the one in which the *core* is located at H. Only at higher energies, when the *core* may be at a greater distances, fluctuations are larger, which is specially true for γ-rays. According to the results here shown, a detector with enough time resolution to appreciate differences of less than 1 ns in the pulse-shape parameters, would be able to discriminate the primary type, and for γ-ray shower it would be possible to locate the *core* position. With present-day electronics this is not feasible, due for example to the PMT's in use, which introduce a widening in the signal of the order of 3–4 ns. Moreover, it should also be taken into account the possible imperfections introduced in the pulse shape by the fluctuations of the background signal, and that real quantum efficiency, which is lower. Both effects limit the ability to determine in a precise way the pulse shape.

In the results shown up to now, we have not taken into account several

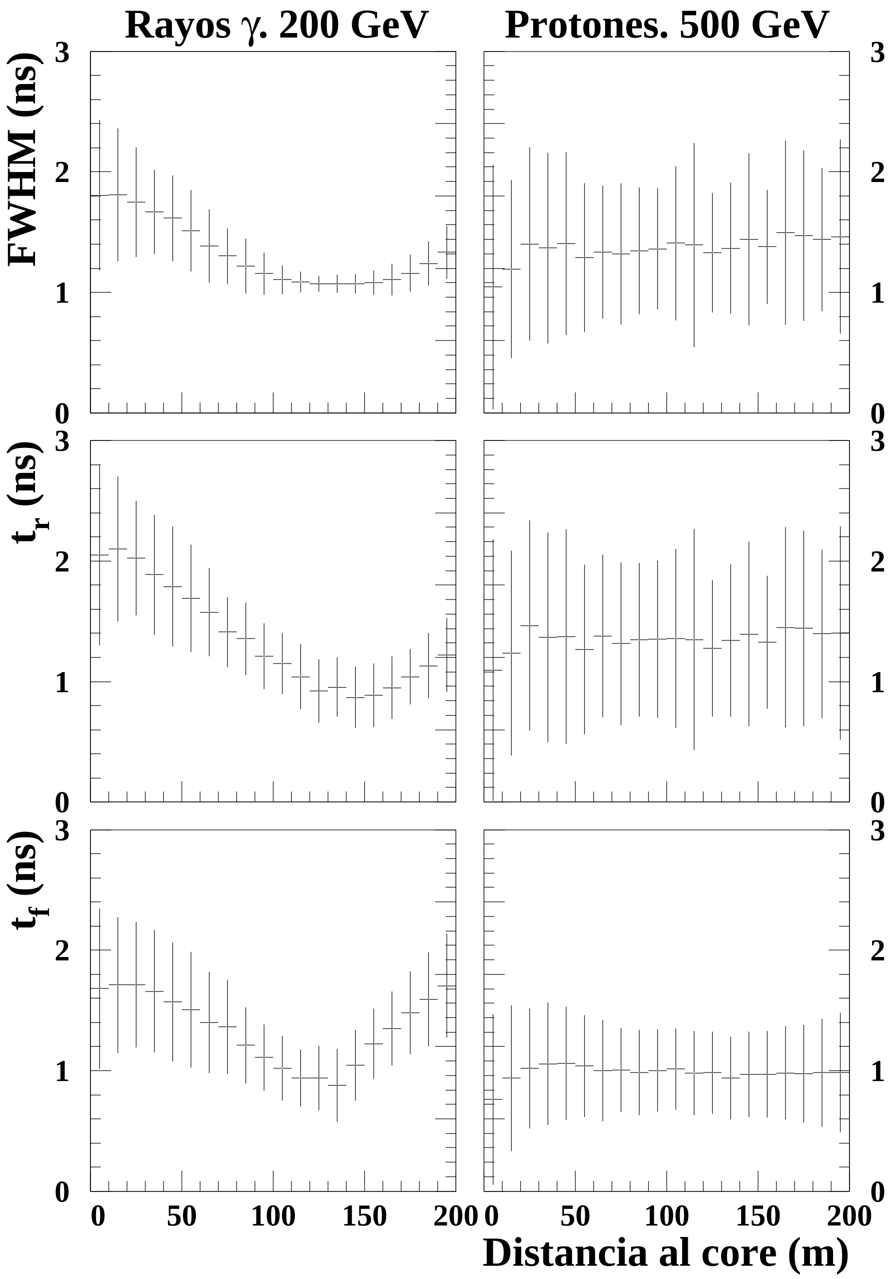

Figure 4.18: *Dependence of the shape parameters of the Čerenkov pulses detected in* **convergent view**. *Mean values is obtained from the pulses collected in all detectors in an area of* $300\times300\,m^2$*, for shower generated in vertical incidence, and the* core *position located randomly at a distance of less that 30 m of the projection of the convergence point. Error bars correspond to the rms of the distributions obtained in each distance interval.*

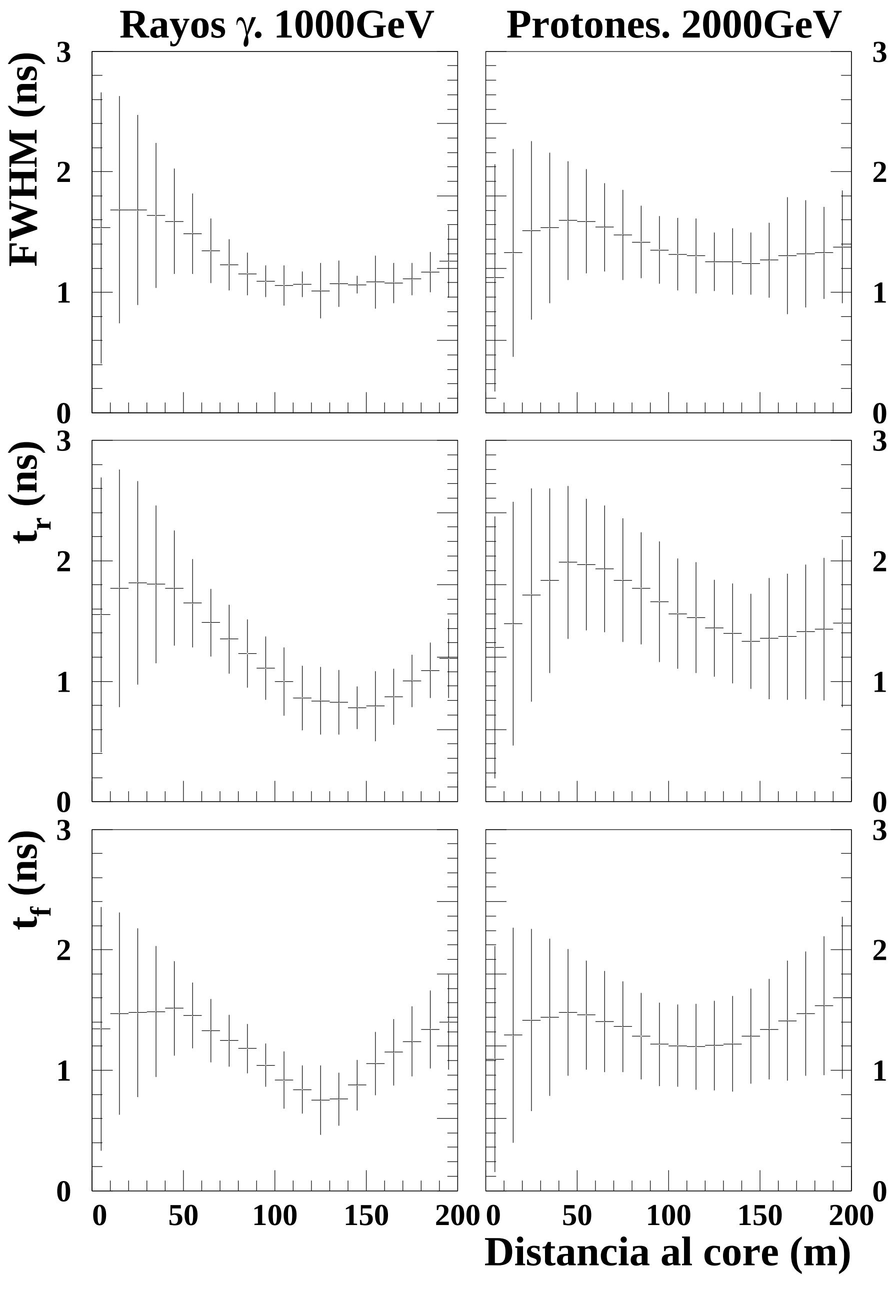

Figure 4.19: *Dependence of the shape parameters of the Čerenkov pulses detected in* **convergent view**. *Mean values is obtained from the pulses collected in all detectors in an area of 300×300 m^2, for shower generated in vertical incidence, and the* core *position located randomly at a distance of less that 70 m of the projection of the convergence point. Error bars correspond to the rms of the distributions obtained in each distance interval.*

effects that take place in a real experiment, as the background-light fluctuations, the alteration of the signals due to the electronics, the lower detection efficiency of a realistic optics, and the quantum efficiency of the PTM's, with a maximum value of $\sim 30\%$. Additionally, up to now we have employed all the information collected in an array of 3249 detector spread over an area of $300 \times 300\,\mathrm{m}^2$, while in a real detector the accessible information is much less. In GRAAL we employ just 63 heliostats spread over a area of $\sim 200 \times 70\,\mathrm{m}^2$, which imposes an important limit in the capability to correctly sample the Čerenkov front.

In order to determine the γ/hadron separation capability in a more realistic detectors, we have carried out an study similar to the ones shown up to now, but limiting the available information to that collected by the GRAAL heliostats. In this study we will include the reduced collection efficiency due to optics and the PMT's. We will not include the background light fluctuations, and we have kept the information collected from each heliostat apart from the other signal. This allows us to extend these results to any other γ-ray telescope using a central-tower solar plant.

In this case the calculi to obtain the fluctuations in the amount of Čerenkov light collected we the heliostats from a given shower, δn, is done from the expected value in each heliostat, given as the mean value of the amount of light collected in all heliostats in a shower, $\overline{N}$. Fluctuations are defined:

$$\delta n_i = \left| \frac{N_i - \overline{N}}{\overline{N}} \right|$$

where N_i is the number of photons detected by the PMT's from heliostat i. Typical fluctuations for each primary type and energy is given by δn, the mean value of δn_i over all heliostats and shower of the considered type. Results are given in table 4.1 under *GRAAL* entry. We can conclude that though fluctuations in proton showers are still larger than in γ-rays, the difference is greatly reduced. Results obtained when the *core* is displaced do not differ significantly from the ones obtained at $r_c = 0$, which indicates that fluctuations due to the limited sampling dominate over the fluctuations proper of the γ-shower, and slightly increment the fluctuations detected in proton showers.In any case the differences between the values of the fluctuations for both primary types is not big enough to give hope in the development of a method to discriminate the primary type based on the study of δn, specially if we take into account that the background light fluctuations have not been taken into account.

In the same manner, we can define the fluctuations in the arrival times of the Čerenkov pulses to each heliostat. In this case we assume that the real *core* position is known (which is not true in the real case). Thus we calculate the distance from each heliostat to the *core*, which corresponds to a time of arrival of the Čerenkov front. The distribution of arrival times as a function of the distance to the *core*, for all the heliostats in a shower, can be adjusted to a circumference $T_{\text{fit}}(r)$ (assuming a spherical front shape). Fluctuations of the arrival time of the Čerenkov pulses are defined for each heliostat as:

$$\delta t_i = |T_i - T_{\text{fit}}(r_i)|$$

where T_i is the measured arrival time of the photons to heliostat i, and $T_{\text{fit}}(r_i)$ is the value of the adjusted function at the *core* distance at which the heliostat is located. From the distribution of the values of δt_i for all the heliostats of all the showers of a given type and energy, it is possible to obtain the value of δt which includes 68% of the events in the interval (0,δt).

In table 4.3 the values of δt are shown under entry *GRAAL*. It can be appreciated that in this case more realistic, the limited sampling limits the separation power of this parameter. There are almost no differences in the values of δt for the different primary types. The value of δt is slightly larger in the showers initiated by protons, but the difference is too small to be of any use. Last, there is no significant difference of this values within the energy of the primary.

Last, in the study of the shape of the detected Čerenkov pulse in the case with limited sampling and realistic efficiency ($\sim 15\%$), the changes in the signal increase the fluctuations and the indetermination of the obtained parameters, which, in addition to the difficulties previously appreciated in this method, dissuades from the use of this parameters in the determination of the parameters of the detected shower.

4.7 Conclusions

From the results shown in this chapter we can conclude:

- From the observables detected without restrictions from the original showers, it is possible to discriminate the primary type. Therefore, it seems feasible the development of efficient methods, based on the fluctuations of the arrival times of the Čerenkov pulse and on the amount of collected light in each detector, or in the pulse shape, with the purpose of discriminating the primary type and *core* position.

- The introduction of angular restrictions in the detectors drastically reduces the differences detected between showers of different primary types.

- In principle, without knowledge of the effects introduced by a more realistic study that takes into account the effects introduced by the fluctuations in the background noise and the limited quantum efficiency, a study of the Čerenkov-pulse shape would be able to get information on the *core* position and the primary type, but the required temporal resolution is beyond the present day technology.

Chapter 5

Characteristics of the telescope and methods of analysis

In this chapter it will be shown the most significant characteristics of the GRAAL detector, obtained from the Monte Carlo simulation described in chapter 3. It will also be shown the method of analysis developed to work on the signals collected in the real detector.

One of the most fundamental parameters that the Monte Carlo simulation can provide is the sensitivity for the detection of γ-rays out of the cosmic-rays background, as well as the energy threshold of the telescope. In order to do this, first we need to determine the effective area of the detector, which depends on the energy, incoming direction and type of primary, and on the trigger system employed. All the results shown in this chapter have been achieved with the charge trigger, as in the real experiment, where both trigger systems work at the same time, it was seen that almost all events that activate the sequential trigger, also activate the charge trigger, and in this case, the latter was the one that determines the characteristics of the telescope.

Once the effective area of the detector is known, it is possible to calculate the expected trigger rate for each primary type (assuming a known flux) which allows us to establish a lower limit for the sensitivity of the telescope.

The sensitivity thus obtained can be optimized, in principle, with the analysis of the signal. Due to the unique characteristics of the GRAAL experiment, no analysis method had been developed, and thus it has been necessary to develop a completely new one. In this chapter we will describe the method employed in the identification of the Čerenkov pulses among the noise fluctuations in the traces, and in its assignment to the heliostat they come from, which will allow us to spatially sample the Čerenkov front. As we will show, this process is closely linked to the reconstruction of the incoming direction of the primary, as the time structure of the pulse train depends on it. This information should allow us to increase the sensitivity of the telescope, though in a limited way, as shown in chapter 4.

In order to do these calculi and to develop the analysis methods, a library of more than 10^5 showers has been generated, initiated both by protons and γ. The generation of these events was done over several processors, with a total generation time of over 275 CPU days on a Silicon Graphics R10000 processor (equivalent to about 1 year of CPU time on a Penthium III (500 Mhz)).

The energy of each primary was randomly chosen within the interval 50 GeV–1 TeV for γ-showers. For protons the interval is 250 GeV–4 TeV. The energy spectrum follows a power law e^{-1}, and not the real, much harder, spectrum, as in this way it is possible to obtain better statistics at low energies (where fluctuations are larger), while keeping enough events of high energy.

As it was shown in §2.2.5.3, the efficiency of the trigger system varies with the observed direction, specially the sequential trigger. Therefore the properties of the detector must be studied for different incoming directions. As there is a North–South symmetry, and as most of the observed sources are located in southern directions, six observing directions were chosen, $\vec{S}(\phi,\theta)$, which correspond to values of the zenith angle θ of 10 and 30 degrees, and the azimuth angle ϕ of 180º (South), 225º (Southeast) and 270º (East).

In the generation of the incoming directions $\vec{I}$ of the showers it was taken into account that γ-rays come from a point source (with respect to the angular resolution of the experiment this is true for all known sources in this energy range) located along the observation axis ($\vec{I}\|\vec{S}$), while protons were generated with random incoming directions around the observing direction. In this way the isotropic cosmic-ray background is simulated. In any case, and in order to optimize the CPU time employed in the shower generation, in the genration of the random directions, a flat probability distribution was chosen for ω, the deviation angle of $\vec{I}$ with respect to $\vec{S}$. ω has a maximum value of 4 degrees, enough to consider negligible the probability of detecting showers with $\omega > 4^{\circ}$. In this way we don't spend much time generating showers with high incidence angles, as they have a very low detection probability.

In order to improve the effectiveness of the CPU time employed on the generation of one shower, each one of them is employed 5 times, each time changing the *core* position with respect to the centre of the heliostat field H. This proceeding is quite commonly employed to increase statistics without increasing the process time, as the generated event is reproccessed several times under conditions which are quite different, at least enough to consider each event almost independent from the rest. In our case, fluctuations due to the displacement of the core position are large enough. For each shift, the core position was randomly chosen within a circle of 300 m radius around H, which is located 76 m to the North of the tower basement, and the probability distribution was generated constant with distance to the core, in order not to generate may events at large distances, were the detection probability is low.

last, it is important to observe that the generated distributions of energy, incidence angles, and core position don't correspond to the real ones. This has been corrected with the applycation of the proper wheights to the generated events.

5.1 Detection efficiency

5.1.1 Effective area

The effective area of a γ-ray telescope, for the detection of a primary Z of energy E, is described by:

$$A_e(Z,E) = 2\pi \int_0^\infty P(Z,E,r) \cdot r \cdot dr$$

where $P(Z,E,r)$ is the detection probability of a shower whose core is locate in the distance interval to the heliostat array $(r, r+dr)$. Ax it will be shown this value also depends on ω and $\vec{S}$.

Due to limitations in the available computing time, the core position was generated within 300 m of H. The detection probability for showers further away is almost zero, event at very large energies. In order to estimate the error thus induced, the following criteria was chosen:

$$\begin{aligned} \forall r / \,(300\,\mathrm{m} < r < 500\,\mathrm{m}) \;&\Rightarrow\; P(Z,E,r) = P(Z,E,300\,\mathrm{m}) \\ \forall r / \,(500\,\mathrm{m} < r) \;&\Rightarrow\; P(Z,E,r) = 0 \end{aligned}$$

In this case, effective area can be expressed as:

$$A_e(Z,E) \;=\; 2\pi \left(\int_0^{300\,\mathrm{m}} P(Z,E,r) \cdot r \cdot dr + P(Z,E,300\,\mathrm{m}) \cdot \int_{300\,\mathrm{m}}^{500\,\mathrm{m}} r \cdot dr \right)$$

Dividing the energetic range of the generated showers in J intervals, and the core distance range in I intervals, the effective area can be expressed for each energy interval j as:

$$A_e(Z,j) = 2\pi \cdot \sum_i P(Z,j,i) \cdot r_i \cdot \Delta r \;+\; \pi \cdot 1.6 \cdot 10^5 \cdot P(Z,j,300\,\mathrm{m})\,\mathrm{m}^2$$

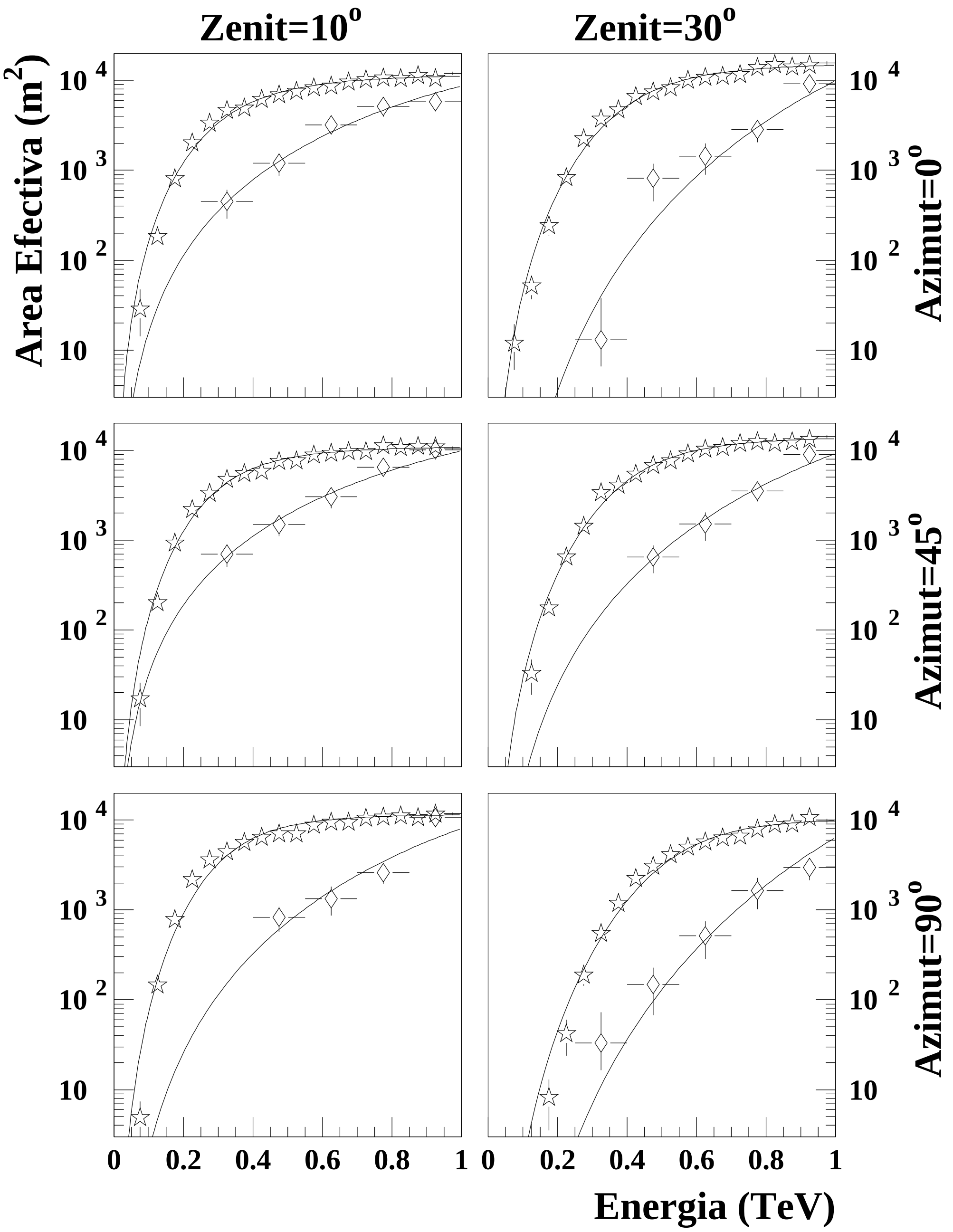

Figure 5.1: *Effective area of the GRAAL experiment for γ-rays (stars) and protons (diamonds) incident along the observation direction ($\omega = 0$), as a function of the primary. Results for the six simulated directions are shown. Solid lines show results for fittings done using function 5.1.*

where r_i takes the value of the center of the i interval of distance to H. The value of $P(Z,j,i)$ is calculated from the total number of showers S_{ij} generated in the energy interval$j$ and distance interval i, and the number of detected showers s_{ij}, as:

$$P(Z,j,i) = \frac{s_{ij}}{S_{ij}}$$

The statistical error associated to the effective area, due to the limited number of generated showers in each energetic and distance interval, can be expressed as:

$$\Delta A_e(Z,j) = \sqrt{\sum_i (2\pi \cdot r_i \cdot \Delta r \cdot \Delta P(Z,j,i))^2}$$

where $\Delta P(Z,E,r_i)$ is the error associated to the detection probability of each of the distance intervals, which, from the error of the binomial function, is:

$$\Delta P(Z,j,i) = \sqrt{\frac{P(Z,j,i)\cdot(1-P(Z,j,i))}{S_{ij}}}$$

In figure 5.1 it is shown the results obtained for each one of the directions in which showers were generated, with GRAAL in convergent view. Each one of the plots shows the value of the effective area a s function of the energy of the primary, for γ-rays and protons, in the six simulated directions. For protons, the sample was limited to those events with $\omega \leq 0.5^{\circ}$. The significance of this function for protons is quite limited, as in reality the distribution of incoming directions is isotropic (see 5.1.2). In any case, figure 5.1 clearly shows that the detection efficiency of the telescope for γ-rays is significantly better than for protons of similar energy. For energies of about 1 TeV for γ-rays, and 2 TeV for protons, the effective area reaches a saturation value which depends mainly of the detector characteristics (p.e. it is modified by the convergent view) and the properties of the shower, given by the primary type. Thus this value varies for γ-rays and protons, being $\sim$12000 m^{2}and $\sim$30000 m^2 respectively. The value is greater for protons due to the larger transverse momentum of hadronic interactions, which allow for its detection at larger distances.

5.1.2 Efficiency with the deviation angle, ω

The detection efficiency of Čerenkov showers shows a strong dependency with ω, that is, with the deviation angle of the incident direction of the primary, $\vec{I}$, with respect to the observed direction, $\vec{S}$.

$\overline{\omega}$ (degrees)		Zenith=10^o	Zenith=30^o
Azimuth	0^o	0.78	0.68
	45^o	0.68	0.67
	90^o	0.67	0.72

Table 5.1: *Mean deviation angle $\overline{\omega}$ with respect to the observed direction for detected proton showers. Results are shown for the six simulated direction.*

This effect is specially important when determining the detection efficiency of the isotropic cosmic-ray background, but also in the search for sources whose coordinates are not so well known, as is the case of non-identified EGRET sources, or in the identification of new γ-ray sources.

Plots in figure 5.2 show the dependence of the detection efficiency of proton showers as a function of ω, for the six simulated directions.

In order to correctly calculate the effective area of protons in isotropic incidence, we must take into account this fact. The results obtained are shown in figure 5.3,for protons generated with $\omega \leq 4^o$. Figure 5.2 shown that detection efficiency for $\omega > 4^o$ is negligible, and therefore the results obtained with the generated events contain all the necessary information for the correct calculation of the effective area. Though a large number of events was generated, due to the low detection probability, statistical errors are rather large. With this results it can be easily calculated the expected proton-detection rate, with the incident flux (as described in the following section §5.1.3).

In table 5.1 for the detected protons, the mean values of ω are shown, and its dependency with $\vec{S}$. Detection efficiency is practically constant for $\omega \lesssim 0.7$ degrees, and falls rapidly to zero for values of ω greater than ~ 1.5 degrees. This behavior is practically independent of the observed direction.

These results show that the width of the detection field of the telescope is slightly larger than its field of view (FWHM ~ 0.5 degrees).

5.1.3 Detection rate

Once calculated the effective area of the telescope as a function of the energy of the incident cosmic ray, we can determine the detection rate for each primary type. In order to do this it is necessary to know the value of the incident differential flux for each primary. For the isotropic proton background the differntial flux at Wiebel et al. [17], obtained from the results gathered by different experiments in the energy range 0.01 TeV–1000 TeV, has been

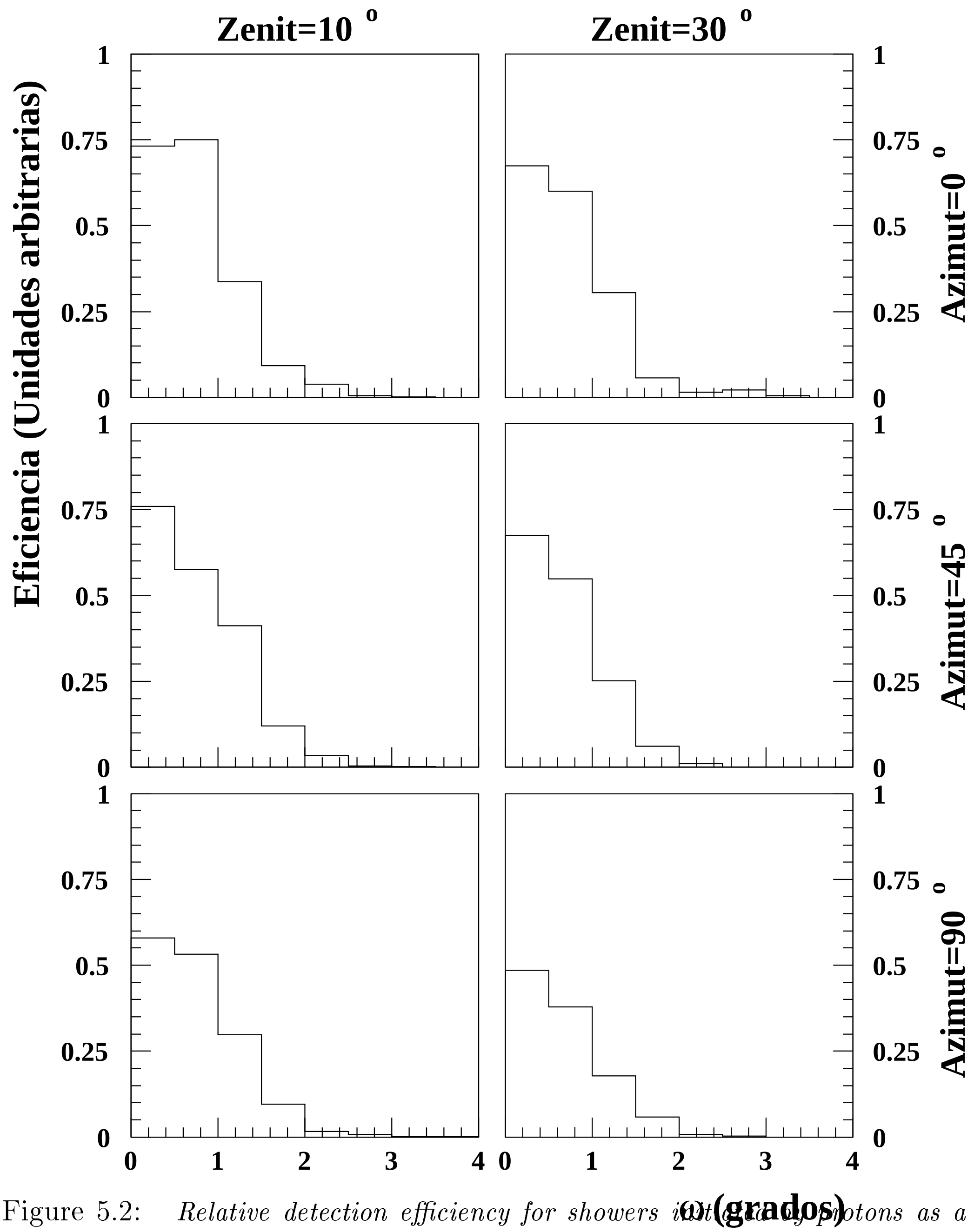

Figure 5.2: *Relative detection efficiency for showers initiated by photons as a function of the deviation angle of the incoming ray with respect to the observation direction, ω. Results for the six observed directions are shown.*

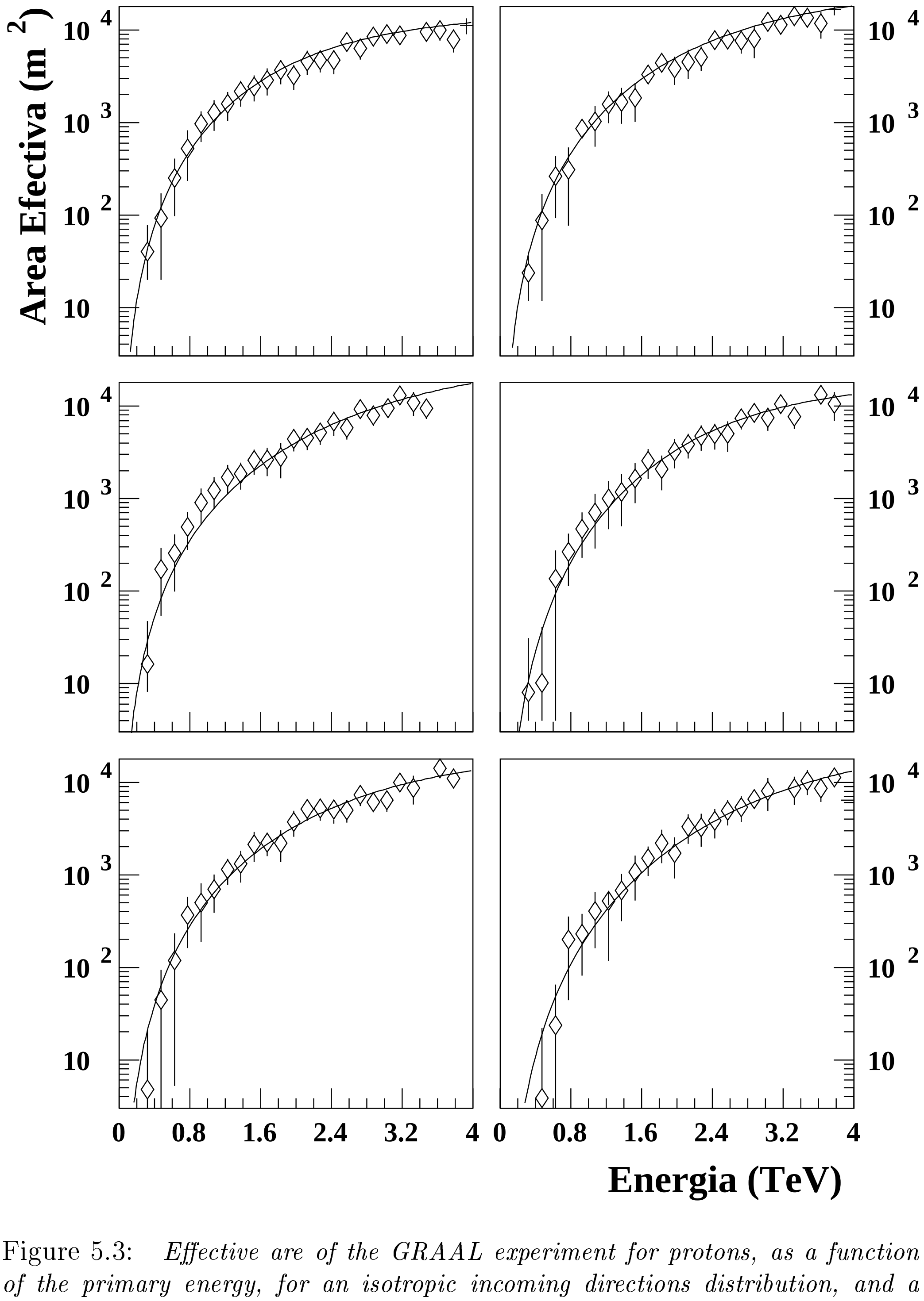

Figure 5.3: *Effective are of the GRAAL experiment for protons, as a function of the primary energy, for an isotropic incoming directions distribution, and a maximum deviation with respect to the observed direction of 4 degrees. Results are shown for the six simulated directions. Solid lines show the results from a fit using function 5.1.*

Rate		Zenith=10^o			Zenith=30^o		
		γ (mHz)	p (Hz)	α (Hz)	γ (mHz)	p (Hz)	α (Hz)
Azimuth	0^o	11.5±0.2	4.0±0.2	0.8±0.1	9.6±0.7	4.1±0.3	0.9±0.1
	45^o	11.9±0.4	3.7±0.2	0.8±0.1	8.1±0.2	2.6±0.1	0.6±0.1
	90^o	11.4±0.5	2.9±0.2	0.7±0.1	3.5±0.2	1.8±0.1	0.4±0.1

Table 5.2: *Estimations of the detection rate of atmospheric showers for the GRAAL experiment, as a function of the primary type and observed direction.*

empoyed:

$$\frac{d\Phi_p}{dE\,d\Omega} = 10.91 \cdot 10^{-2} \left(\frac{E}{\mathrm{TeV}}\right)^{-2.75} (\mathrm{m}^2 \cdot \mathrm{s} \cdot \mathrm{sr} \cdot \mathrm{TeV})^{-1}$$

The expected proton trigger rate R_p is:

$$R_p = \int_0^\infty \frac{d\Phi_p}{dE\,d\Omega} \cdot \overline{A_e}(p, E) \cdot \Omega_p \cdot dE$$

where Ω_p is the incident solid angle of the protons, and $\overline{A_e}(p, E)$ is the mean effective area associated to Ω_p. The value of Ω_p is arbitrary, as long as it is large enough to be sure that protons with incidence angles not included in Ω_p have an almost zero detection probability. In our case $\Omega_p = 0.0153\,\mathrm{sr}$ ($\omega \leq 4^{\mathrm{o}}$). The results obtained for R_p as a function of the observed direction $\vec{S}$ is shown in table 5.2. Errors shown in this table are of statistical origin, and have been estimated by comparing the results obtained after dividing the total sample of events in two independent subsamples. It can be expected that systematic errors are larger, due to the inaccuracies of the simulation (see §3.1.5), and to the variable experimental conditions, not taken into account in the simulation, as the heliostat reflectivity variations with time, or the changing atmospheric conditions.

As protons are nearly 90% of the cosmic radiation in this energy range, these results are a good estimator of the trigger rate expected at the experiment. In any case, it has been estimated the contribution of He nuclei, the second most abundant component of cosmic radiation, with about 9%. Assuming that the effective area is basically function of the Čerenkov radiation on the ground, and taking into account that α-initiated showers generate about half the Čerenkov light of a proton shower of the same energy [18], we can estimate the effective area of α particles as:

$$\overline{A_e}(\alpha, E) = \overline{A_e}(p, E/2)$$

Knowing the differential α-particle flux in the energy range 0.01 TeV–1000 TeV [17]:

$$\frac{d\Phi_\alpha}{dE\,d\Omega} = 6.6 \cdot 10^{-2} \left(\frac{E}{\mathrm{TeV}}\right)^{-2.62} (\mathrm{m}^2 \cdot \mathrm{s} \cdot \mathrm{sr} \cdot \mathrm{TeV})^{-1}$$

We obtain the values shown in table 5.2, which show that the expected trigger rate at the experiment is about 20% higher than that due to protons. The rest of the hadronic component is negligible, specially taking into account possible systematic errors.

The expected trigger rate for a point source of γ-rays is:

$$R_\gamma = \int_0^\infty \frac{d\Phi_\gamma}{dE} \cdot A_e(\gamma, E) \cdot dE$$

that depends on the energetic spectrum of the observed source. It is possible to calculate it dot the Crab Nebula, considered the main source in this energy range. Assuming a differential spectrum like:

$$\frac{d\Phi_\gamma}{dE} = 3.25 \cdot 10^{-7} \left(\frac{E}{\mathrm{TeV}}\right)^{-2.44} (\mathrm{m}^2 \cdot \mathrm{s} \cdot \mathrm{TeV})^{-1}$$

measured by the Whipple telescope for energies above 300 GeV [19], and using the results of $A_e(\gamma, E)$ from our simulation, we obtain the values shown in table 5.2.

5.1.4 Energy threshold

The energy threshold of a Čerenkov telescope is not clearly defined. Due to the large statistical fluctuations, low energy particles can activate the trigger system. The low probability of these detections is compensated by the strong increase of the flux for low energies, and therefore, the contribution of detections bellow the "energy threshold" can be significant. The definitions of energy threshold most commonly employed are:

- The energy threshold is defined as E'_{th} that:

  $$R_\gamma = \int_{E'_{th}}^\infty \Phi_\gamma(E) \cdot A_{max} \cdot dE$$

  where R_γ is the value of the γ-ray-shower detection rate, $\Phi_\gamma(E)$ is the spectrum of the incident γradiation, and A_{max} corresponds to the saturation value of the effective area. This method is similar to assuming that the $A_e(E)$ function behaves like a step function, with a value of zero to E'_{th}, and then a value equal to the maximum effective area.

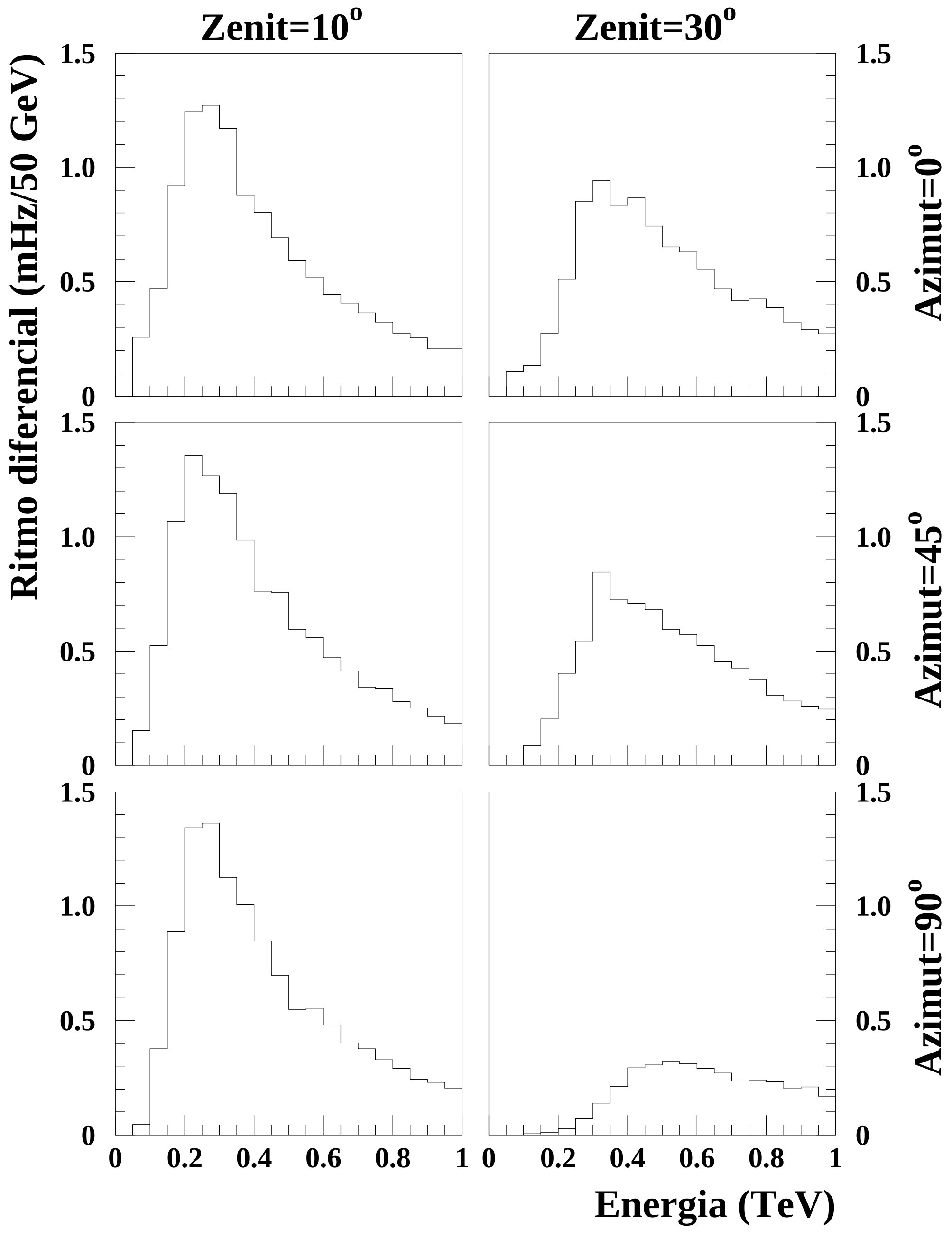

Figure 5.4: *Differential γ-ray trigger rate. Results for the six simulated directions are shown.*

Energy threshold γ (GeV)		Zenith=10^o			Zenith=30^o		
		E'_{th}	E''_{th}	E'''_{th}	E'_{th}	E''_{th}	E'''_{th}
Azimuth	0^o	340±30	360±50	275±50	380±30	470±50	325±50
	45^o	330±30	360±50	225±50	430±40	470±50	325±50
	90^o	340±30	360±50	250±50	770±60	580±50	550±50

Table 5.3: *Energy threshold for the detection of γ-rays, as a function of the observed direction. Values for the three methods described in the text are shown.*

- In a second definition the energy threshold is given by parameter E''_{th} that fits the effective area distribution with function:

$$A_e = \frac{A_{max}}{1 + \left(\frac{E''_{th}}{E}\right)^{\Gamma}} \tag{5.1}$$

  where A_{max} and Γ are the other two parameters of the fit. The chosen fit function is arbitrary, with no physical justification. The value of A_{max} corresponds to the saturation value of the effective area. In this approximation, the value of the energy threshold is that energy at which the effective area is half the maximum. As parameter Γ increases, the result obtained by this method resembles more the result obtained with the previous one.

- In a third definition, the Energy threshold E'''_{th} is obtained from the differential trigger-rate curve, where the contribution of each energy interval to the total trigger rate is shown. The shape of this curve depends both on the effective area function and on the spectrum of the incident radiation, and therefore is the best indicative of the energy interval that provides the large contribution to the measured rate. Once this curve is obtained, the energy threshold is given by the maximum of this function. In figure 5.4 the differential-rate curve obtained from the simulation is shown, taking the Crab Nebula spectrum for the incident flux.

Results obtained from the three methods are shown in table 5.3. We can observed that the values differ depending on the employed definition.

5.2 Identification of the Čerenkov pulses. Incident direction reconstruction.

5.2.1 Introduction

Each time the trigger system activates, the temporal traces collected in the four cones are recorded. These traces contain the information necessary to reconstruct the incoming direction of the primary* and identify the heliostat associated to each pulse. This information is basic in order to develop other methods to improve the sensitivity of the experiment, and to proceed to the discrimination of the primary type. In fact, the method employed to extract the γ signal from the hadronic background fluctuations is based on the comparison of the data collected when observing the candidate γ source (ON observation) with data collected under similar conditions of a region where no γ source is expected (OFF observation). In a first approximation, the γ signal would be obtained as the difference ON-OFF, but due to the fact that the observing conditions may change between both observing periods (for example, the noise background level may not be the same), this simple method would originate artificial signals or anti-signals. It is thus convenient to have some additional information to realize a normalization of the events collected in both periods, in such a way that the events become independent of the observing conditions. Therefore it is clear the necessity for an analysis method that provides both a calibration value for the search of γ signals and the bases for future primary-type discrimination methods.

5.2.2 Analysis method

The first objective of the analysis of the detected traces is the identification of the Čerenkov pulses from the noise fluctuations. This task is rather complex due to the nature of the detected signal. On one side the time structure of the detected train of pulses depends on the incident direction of the shower and on the shape of the Čerenkov front. On the other side, it is very probable, specially in low energy showers, that light is not detected from some of the heliostats, or that the collected light is insufficient to generate a pulse large enough to be distinguishable from the background fluctuations. Last, it is possible that the times at which the Čerenkov pulses are detected do not correspond to their position in the theoretical expected sequence for the incoming direction of the shower. This can be due, not only to the time

*More precisely, and due to the imprecision in the location of the core, it is possible to determine the center of the sphere that fits the detected Čerenkov pulse (see fig. 5.5) fluctuations of the Čerenkov front, but also to the slight displacement in the position of the maximum of the pulses due to the background fluctuations. This last effect is specially important in small pulses.

Therefore it is necessary to develop an algorithm to analyze the detected traces that, from the theoretical structure of the train of pulses, is able to identify the Čerenkov pulses in the real trace, and assign them to the heliostat they come from.

This work is closely linked to the determination of the incidence direction of the shower, and on second approximation, to the shape of the Čerenkov front. In order to calculate the theoretical pattern, and after the results shown in §4.3 the chosen shape for the Čerenkov front is that of a sphere locate near the convergence point.

The method employed to accomplish the analysis is based on the comparison of the relative arrival times of several pulses, chosen in the four traces, with the relative arrival times expected from the theoretical sequence. The theoretical sequence depends strongly on the incoming direction of the shower, and it is possible that the measured positions of the pulses are compatible with several incoming directions, or that there is more than one way to adjust the theoretical pattern to the detected one. In this case it will be necessary to develop a method to chose the most probable identification (see figure 5.5).

First, we choose, from the traces of the four cones, those peaks that will be employed in the comparison. The election of these peaks is very important, because if one of them is not generated by the Čerenkov front, but by a fluctuation in the noise background, it could lead to a wrong identification. On the other hand, if the condition required is very hard, we would have a small number of pulses, and therefore the information to accomplish the reconstruction would be scarce. The method employed to choose the peaks is based on the analysis of the background fluctuations. Due to the configuration of the electronics, it is expected that in the first 50 ns of the traces no Čerenkov pulse arrives, and therefor an analysis of this interval provides us with information on the value of the typical noise fluctuations, σ. In order to minimize the probability to choose peaks induced by the noise fluctuations, we choose as Čerenkov pulses those whose amplitude is larger than $n_1 \cdot \sigma$ $(n_1 > 1)$.

As we don't know the incidence direction of the shower, and in order to calculate the theoretical pattern, we define a grid of possible directions. This grid is $\eta_1 \times \eta_1$ degrees^2 wide, with $(\eta_1/\zeta_1 + 1)^2$ *nodes* around the observed direction (see figure 5.5). We calculate the theoretical pattern for each of the

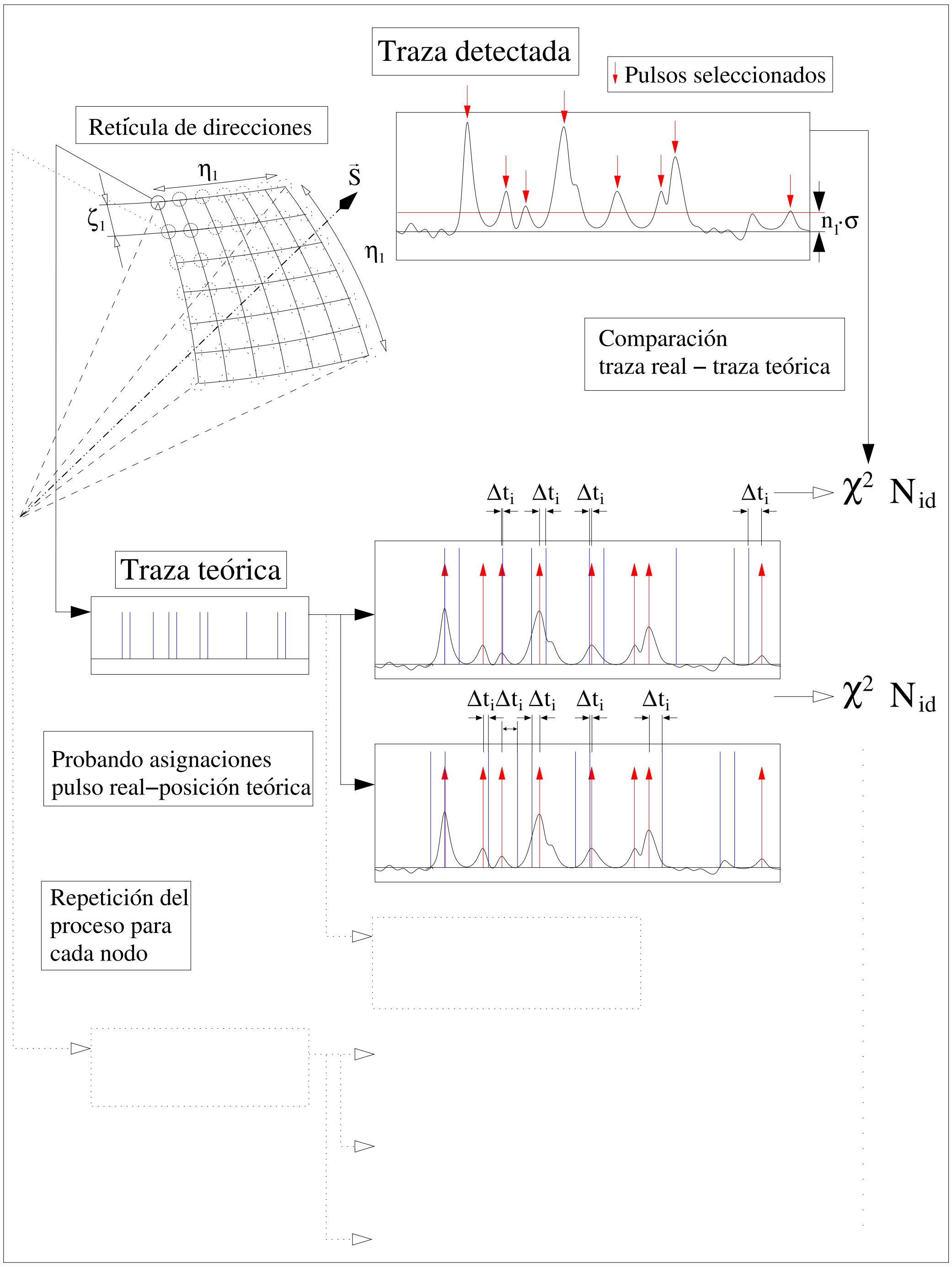

Figure 5.5: *Scheme of the method employed to identify the Čerenkov pulses in the real traces. Once chose, in the real trace, those pulses that fluctuate from the mean more than $n_1 \cdot \sigma$, a grid of possible directions is defined around the observed direction, $\vec{S}$. For each point in the grid the theoretical sequence is calculated and compare to the real sequence. As the heliostat from which each of the pulses comes is not known, we proceed to assign each real peak to one theoretical, determining for each one, the number of identified peaks ($\Delta t_i < \delta$) and the value of χ^2. For sake of simplicity only one trace has been shown, but in the process information from th e four traces is employed.*

nodes of the grid, repeating in each one of them the following comparison process between the theoretical pattern and the pulses located in the real trace: As we don't know which heliostat each one of the peaks in the real trace (real peaks) comes from, we try *assigning* the arrival time of one of the real peaks to the arrival time of one of the theoretical ones, repeating the process for all the real peaks. In each one of this *assignations* we compare the positions of the rest of the peaks with the positions of the theoretical peaks, considering that an *identification* real peak–theoretical peak takes place when the time difference is lower than δ ns. For each *assignation* we count the total number of *identified* peaks in the four cones, N_{id}, and we define:

$$\chi^2 = \sum_i (\Delta t_i)^2 / N_{id}$$

where Δt_i is the time difference between the real peak and the nearest theoretical peak.

One this operation is accomplished, for all the possible *assignations* of real peaks to theoretical ones, and for all the *nodes* in the directions grid, we choose the correct identification with the following criteria:

1. we choose that with the highest number of identified peaks, $N_{\max}$;
2. in case there is more than one solution with $N_{\max}$ identified pulses, we choose that with the lowest χ^2.

In this way we determine the position of the pulse train in the traces of the four cones, and we can proceed with the identification of the pulses with their heliostats. For each position in the trace, where the theoretical pattern predicts the existence of a real peak, we define a region $2 \cdot W$ ns wide. We fit this region to a gaussian function. In case the maximum of the gaussian is larger than $n_2 \cdot \sigma$, we consider that a peak has been found, and it is identified with the heliostat that generates the theoretical peak in this position. The possibility exists of having pulses from several heliostats arriving very close in time, so that an overlapping among them may take place (see 2.2.5.2). In case the theoretical sequence predicts this overlapping, the region is defined so it includes all the possible overlappings, and the fitting is done to a function product of adding as many gaussians as peaks are expected in the region, leaving the identification heliostat-peak to a later stage of the analysis. The result of the fittings provides the positions of the peaks, along with their width and amplitude.

In order to accomplish a better fitting to the incoming direction, and be able to assign the peaks found in overlapping to their heliostats, we proceed in a similar way as we did in the identification of the real pulses, defining a new grid $\eta_2 \times \eta_2$ wide, divided in intervals of ζ_2 degrees, around the direction where the identification has been done. As values for the arrival times of the detected pulses we use those obtained from the previous fittings. Again, for each node in the grid we calculate the value of χ^2, pairing each real peak with the corresponding theoretical peak. In case of overlapping we try all the possible combinations of the found peaks with the theoretical peaks, choosing the configuration with the lowest χ^2.

This is the last step of the identification and reconstruction of the incoming direction, and the direction corresponding to the node with the lowest χ^2 value, is chosen as the reconstructed direction, and the identifications heliostat-peak are those determined for that node.

The method here described depends on a number of parameters whose values must be determined. In order to do this we have carried out a number of tests, checking the values that optimized the identification and reconstruction method. The values employed in the analysis of the results presented in this work are:

$$\begin{aligned} n_1 &= 5 \\ n_2 &= 3 \\ W &= 3\,\mathrm{ns} \\ \eta_1 &= 8^{\mathrm{o}} \\ \zeta_1 &= 0.2^{\mathrm{o}} \\ \eta_2 &= 1^{\mathrm{o}} \\ \zeta_2 &= 0.1^{\mathrm{o}} \end{aligned}$$

As it can be appreciated in the previous process we have not taken into account the core position of the shower. This does not mean that this value is not important in the determination of the incoming direction of the shower, nor that the method is independent of the core position. On the contrary, the fact that the Čerenkov front is spherical means that it is impossible to find the core from the analysis of the arrival times of the front to the heliostats. In fact, in the previous process it has been assumed the position of the core in the center of the heliostat field. In this way the direction reconstructed with this method is directly related to the center of the reconstructed sphere, P (see figure 5.6). Deviation angle of the reconstructed direction ξ with respect to the observed direction, corresponds to the angle between the segment that joins H and P, and the observation axis. This limit is unavoidable in this point of the analysis, as any method to locate the core must be based on

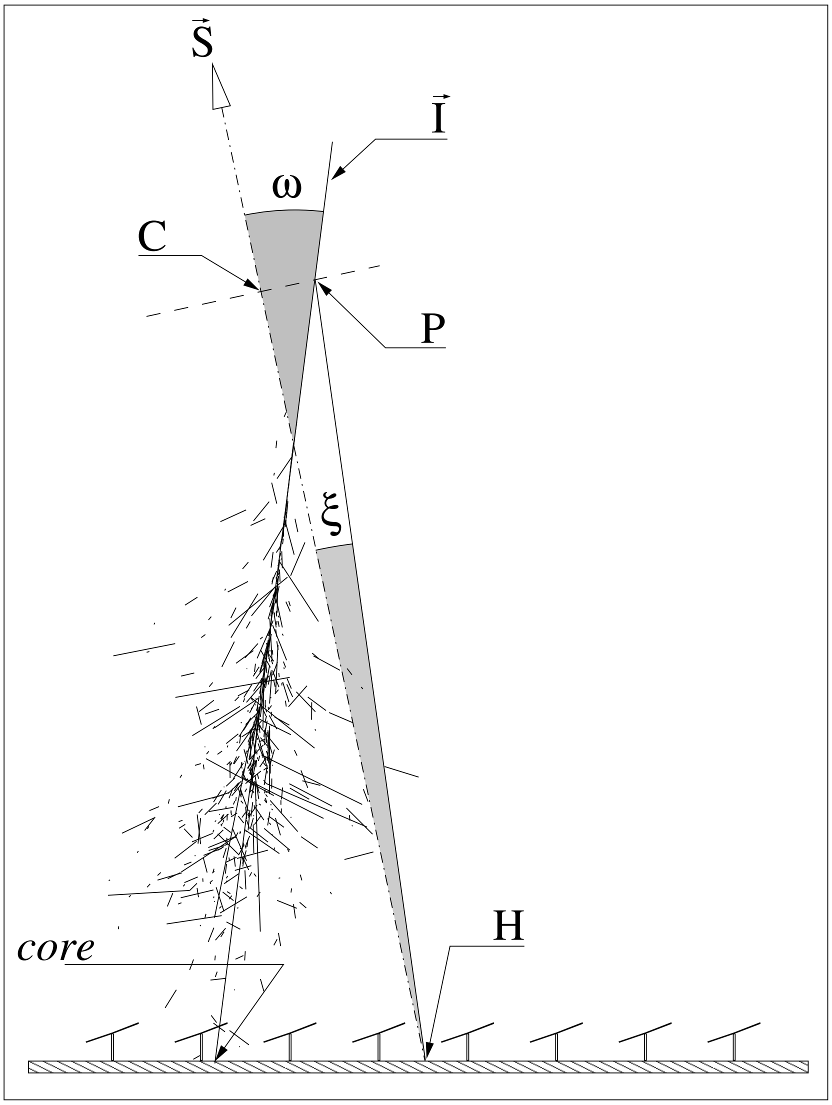

Figure 5.6: *Scheme of the process to reconstruct the incoming direction. The heliostat field observes source at $\vec{S}$, in convergent view, aiming to convergent point C. The detected shower crosses the convergence plain at P. The real deviation angle of the shower with respect to the observed direction is ω, but the reconstruction method, as it assumes that the core position is at H, obtains ξ as the deviation angle.*

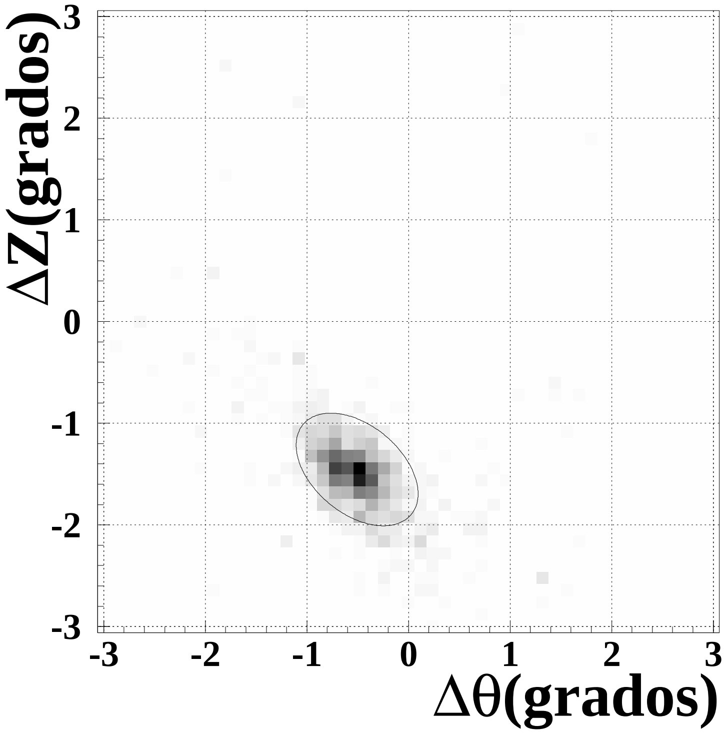

Figure 5.7: *Reconstruction of the incoming directions of a source located at a position different from the one chosen as start point of the identification method. In the example shown the source was shifted to (-0.5 degrees, -1.5 degrees). The center of the reconstructed directions is located at (-0.51,-1.46).*

the information collected at each heliostat position, and the identification heliostat-peak is not done until the reconstruction of the direction. Once the identification heliostat-pulse is done, it may be possible to develop a method to locate the core, and after that, in an iterative process, it might be possible to improve the values obtained for the reconstructed direction and the core position.

The maximum error caused by the fixed core position in the center of the heliostat field can be calculated with the effective are. As the maximum effective area is of the order of $10000\,\mathrm{m}^2$, we infer that in most detected showers the core is located at a distance of less than $60\,\mathrm{m}$ from the center of the heliostat field. Therefore, if P is located $11\,\mathrm{Km}$ away along the observation axis, the maximum error in the reconstructed direction is ~ 0.3 degrees.

We can highlight that the method employed in the identification of the Čerenkov pulses and the reconstruction of the directions does not show a preference for any direction, and there is no bias towards the correct direction, as it is chosen as the center of the first grid. This is easily testable defining a wrong starting direction in the method. In this case the reconstructed directions accumulate towards the real incoming direction, as is shown in figure 5.7.

5.2.3 Quality of the heliostat–peak identification

The described method is based on the correct identification of the theoretical pattern. It has been checked that in less than 1% of the events the sequence of detected pulses cannot be assigned to any direction. In order to determine the quality of the identification we define a new parameter τ_i for each identified heliostat, as:

$$\tau_i = |t_{id} - t_{re}|$$

where t_{id} is the arrival time of the pulse which the heliostat has been identified with, and t_{re} is the time in which it should be identified (obtained from the simulation). For each simulated event we calculated the mean value of τ_i, $\overline{\tau_i}$. Of the distribution of $\overline{\tau_i}$ for all the generated events we obtain the value of τ defined in such a way that the interval $(0, \tau)$ includes 63% percent of the events. We must take into account that, as the tie resolution of the traces is 0.5 ns, the minimum value of τ_i cannot be lower than that.

In the ideal case where the noise fluctuations are inexistent, the identification method obtains very good results. In this case the number of identified events is larger that 46, with $\tau \sim 0.6$ ns, very close to the theoretical limit. When noise fluctuations are introduced, the quality of the identification is worse, and τ becomes larger to a value close to 1.12 ns for γ-rays and $\sim$2.65 ns for protons, observing that it is almost constant for all directions, for a given primary. In the same manner, the number of identified peaks goes down to ~ 24.

These results have been obtained directly from the analysis. It is expected that a further analysis which rejects those events of worse quality, may increase the quality of the data, as is shown in the following section.

5.2.4 Quality cuts

For a non-negligible fraction of the simulated events, the quality of the reconstruction of the shower front is low, leading to important errors in the found direction. These events introduce inexactitudes in the sample, and therefore it is usual to apply some quality cuts, imposing restrictive conditions in some quality parameters.

These cuts must keep most of the events, specially those induced by γ-rays, because otherwise, even though the quality of the sample may increase significantly, the number of events might diminish in such a way that the statistical errors increase to the point of lowering the sensitivity of the detector.

We will take as a value for the quality of the remaining sample after the cuts, the value of τ above described.

In figures 5.8 we show the distributions of: the value of χ^2 for the reconstructed direction; the sum of the amplitudes for all the adjusted pulses, H_T; and the number of correctly identified heliostats, N_{id}. The distributions for events with $\overline{\tau_i}$ lower (blue) and larger (red) to 1 ns are shown, along with the resulting distributions for $\overline{\tau_i} > 1$ ns after the cuts (black). In order to carry out an study independent of the direction, the distributions have been calculated for all the generated events in all directions, keeping different graphics for the different primaries.

From these distributions it can be appreciated that there is a light dependence of the error in the identification method with N_{id} and H_T. No dependence is observed on parameter χ^2, for none of the considered primaries. From the analysis of these distributions we have chosen as cutting values that minimize error τ:

1. $N_{id} > 8$

2. $H_T > 400\, mV$

With these two cuts, the value of τ is reduced down to ~ 1.1 ns for γshowers, while for protons this value remains at $\sim$2.4 ns. The percentage of events that pass this double cut is relatively high, above 75% for γ-showers and 70% for protons. The resulting distributions after the cuts (black curves) show that no other cut may increase this results in a significant way.

These are the cut applied to obtain the results shown from now on. In the real experiment, due to instrumental effects not fully implemented in the simulation, it is necessary to apply other cuts. The cuts applied in the real case are determined for each data run.

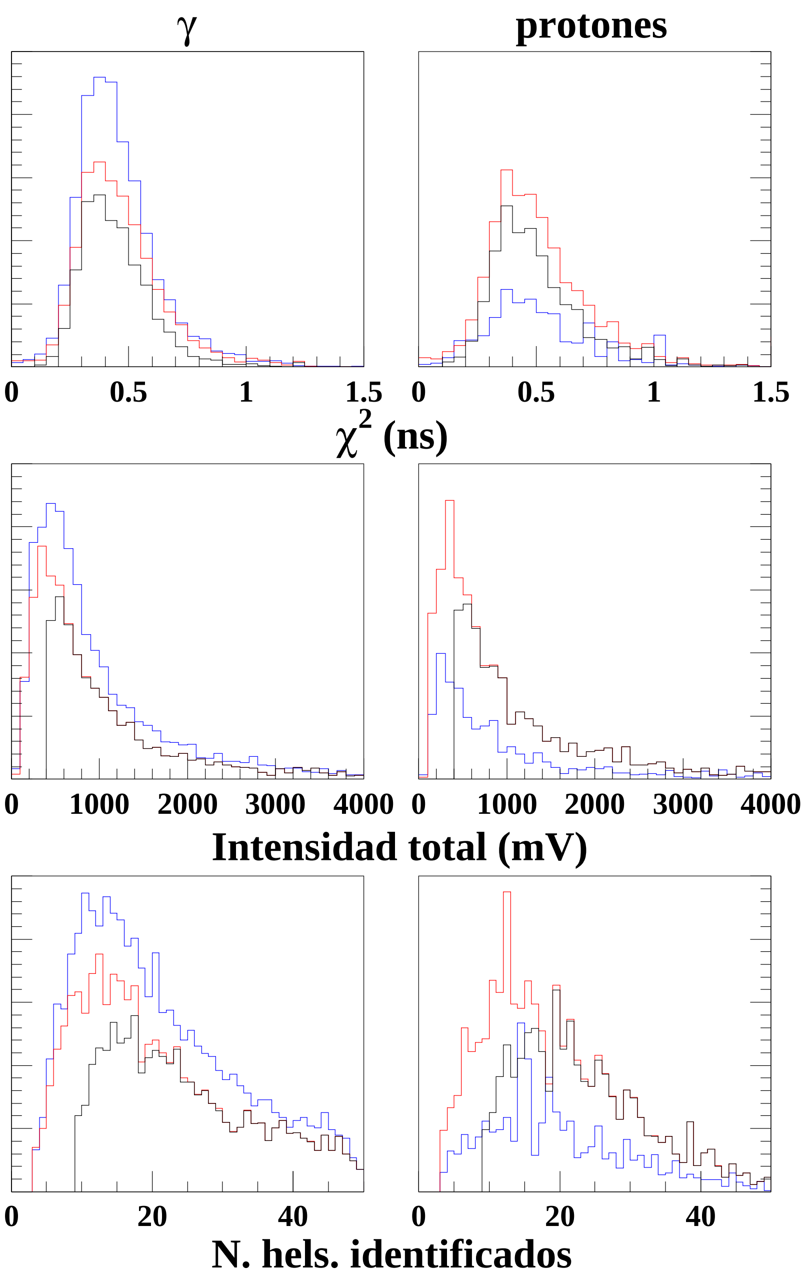

Figure 5.8: *Distributions of the mean parameters of the identification method. For each parameter three distributions are shown. each one obtained for all the events simulated in all directions, and corresponding to: (blue) events which fulfill* $\overline{\tau_i} < 1$ *ns, (red) events which fulfill* $\overline{\tau_i} > 1$ *ns, and (black) events which pass the cut but have* $\overline{\tau_i} > 1$ *ns.*

5.2.5 Reconstruction of the incident direction

As it has already been shown, due to the lack of information on the position of the core, the reconstruction of the core done in the identification method does not obtain the real incident direction, but the deviation angle ξ (see figure 5.6). In case the core position is known, it may be possible to develop a more advanced method to obtain the true incident direction, but until this is attained, the position of the sphere center P is the only accessible information. The distribution of the directions thus reconstructed, provides with information on the positions of the reconstructed sphere centers.

following the process described in §5.2.2 the incident directions for the simulated events have been reconstructed. For each event, the angular distance between the observed and reconstructed directions has been obtained, unfolding it in two components θ and Z, where Z corresponds to the angular deviation along the zenith axis, and θ corresponds to the angular deviation along the parallel of value zenith Z. The corresponding bidimensional distributions for γ-rays incident along the observed direction are shown in figure 5.9, while protons incident with isotropic distribution are shown in figure 5.10). These functions can be fitted with a bidimensional gaussian [20] like:

$$P(\theta, Z) = \frac{1}{2\pi\sigma_\theta\sigma_Z}\frac{1}{\sqrt{1-\rho^2}} \cdot exp\left\{-\frac{1}{2(1-\rho^2)}\left(\frac{\theta^2}{\sigma_\theta^2}+\frac{Z^2}{\sigma_Z^2}-\frac{2\rho\theta\, Z}{\sigma_\theta\sigma_Z}\right)\right\}$$

where:

$$\rho = \frac{\sigma_{\theta Z}}{\sigma_\theta\sigma_Z}$$

where $\sigma_{\theta Z}$ is the covariance of θ and Z, and σ_θ and σ_Z are the standard deviation of the distribution along both axis.

In this fit it is allowed a correlation on the axes, in such a way that the gaussian can be "rotated" with respect to the coordinate axis. We define in this case a new reference system (x,y) along the major and minor axis of the adjusted function, where the deviations along these axes are expressed as (see figure 5.11):

$$\begin{aligned}
\sigma_x &= \sqrt{\sigma_\theta^2 \cdot \cos^2\alpha + \sigma_Z^2 \cdot \sin^2\alpha + 2 \cdot \sigma_{\theta Z} \cdot \cos\alpha \cdot \sin\alpha} \\
\sigma_y &= \sqrt{\sigma_Z^2 \cdot \cos^2\alpha + \sigma_\theta^2 \cdot \sin^2\alpha - 2 \cdot \sigma_{\theta Z} \cdot \cos\alpha \cdot \sin\alpha}
\end{aligned}$$

where:

$$\alpha = \frac{1}{2}\arctan\left(\frac{-2\cdot\sigma_{\theta Z}}{\sigma_Z - \sigma_\theta}\right)$$

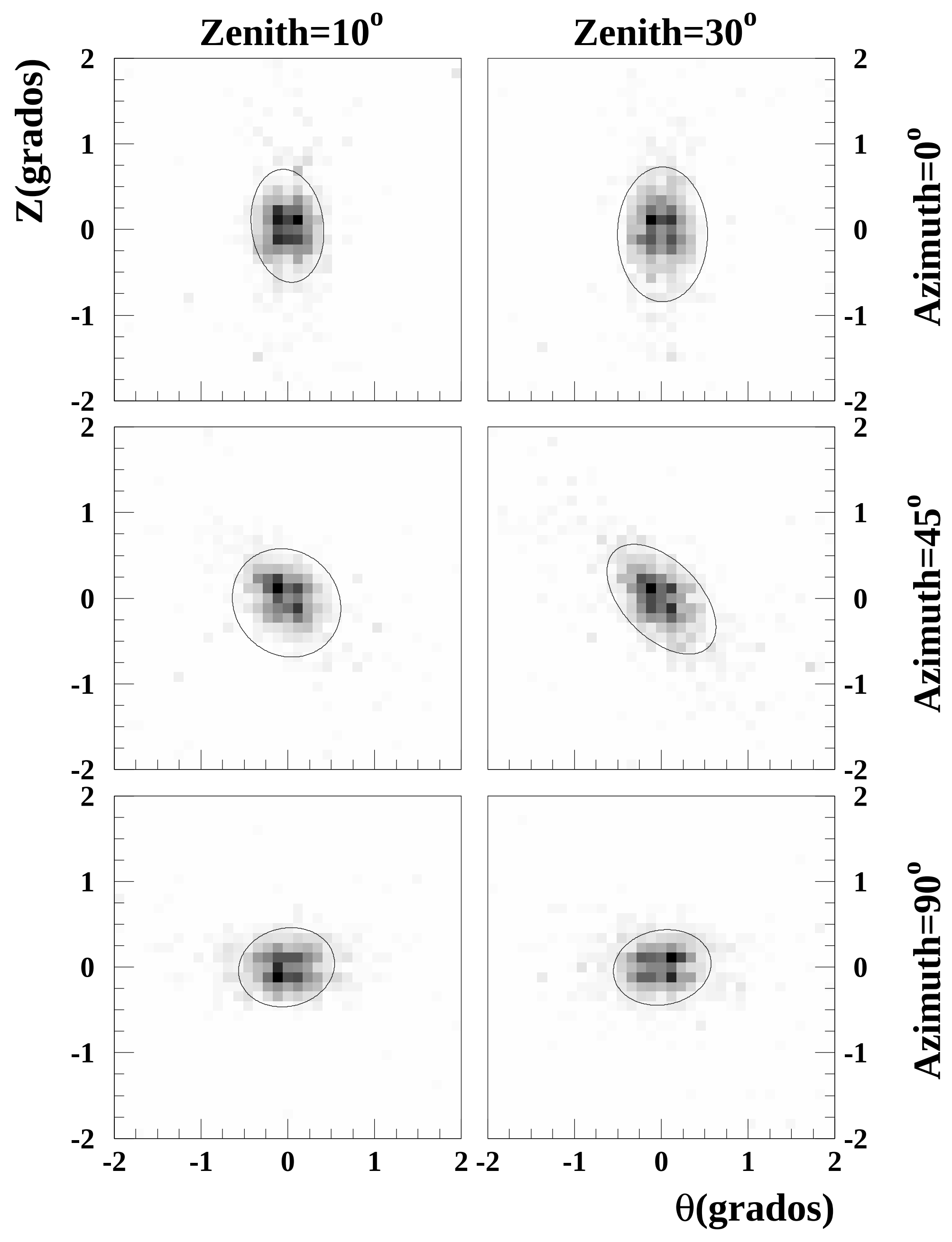

Figure 5.9: *Distributions of the deviations of the reconstructed directions with respect to the observed direction for simulated γ-rays, for the six observed directions. The picture axes correspond to deviations along the zenith axis Z, and the one perpendicular to this, θ. The ellipsis shown contain 63% of the events, and are obtained from the fitting of the distributions of the reconstructed events to a bidimensional gaussian.*

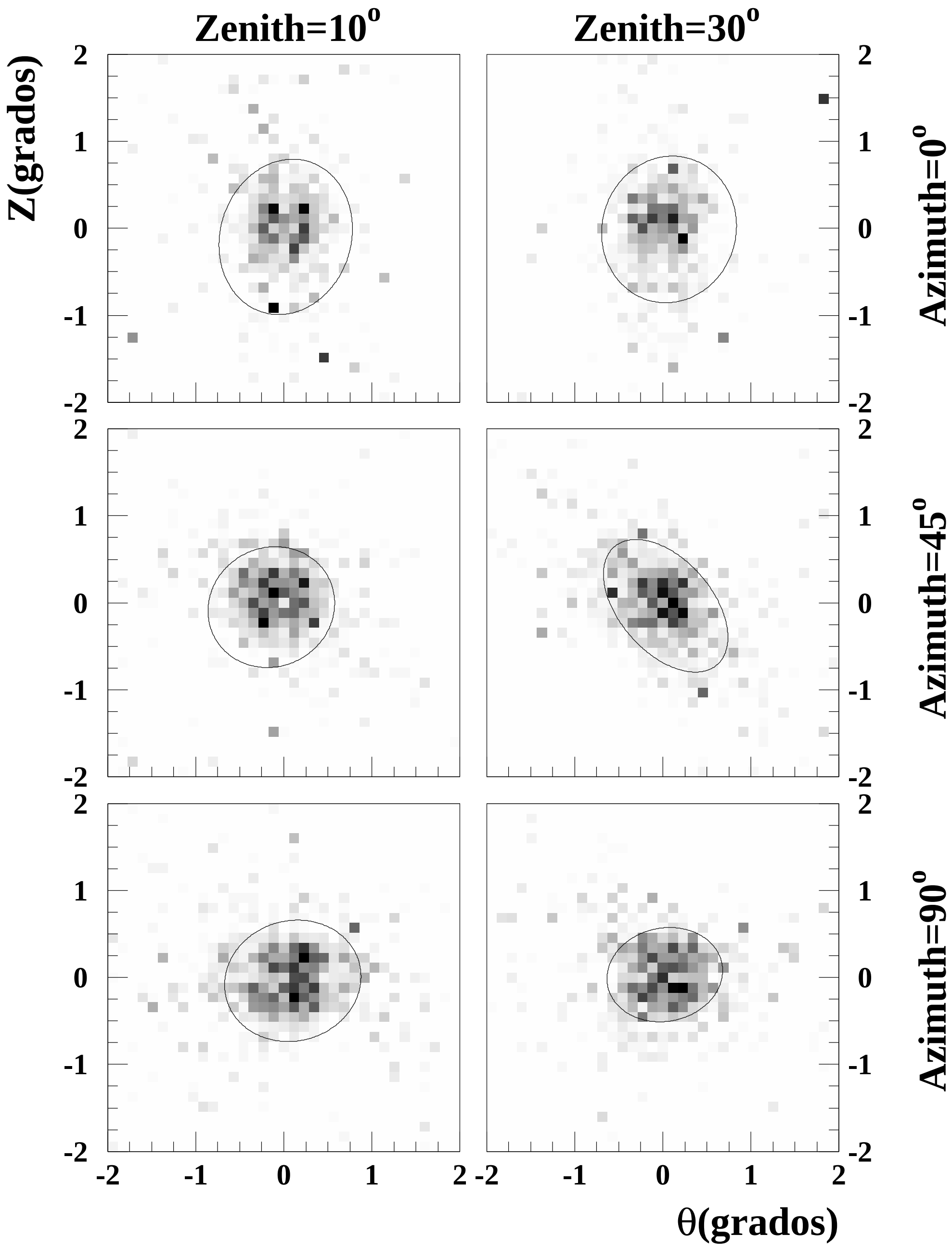

Figure 5.10: *Distributions of the deviations of the reconstructed directions with respect to the observed direction for simulated protons, for the six observed directions. The picture axes correspond to deviations along the zenith axis Z, and the one perpendicular to this, θ. The ellipsis shown contain 63% of the events, and are contained from the fitting of the distributions of the reconstructed events to a bidimensional gaussian.*

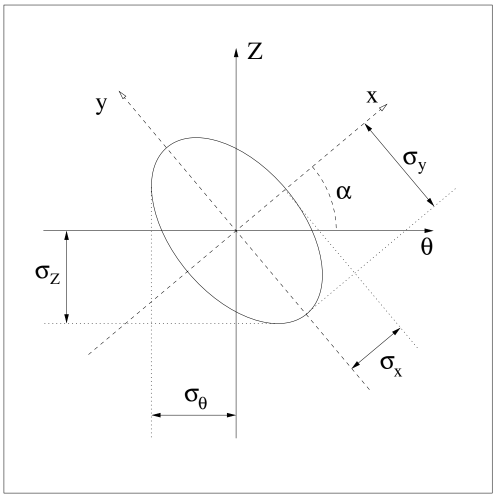

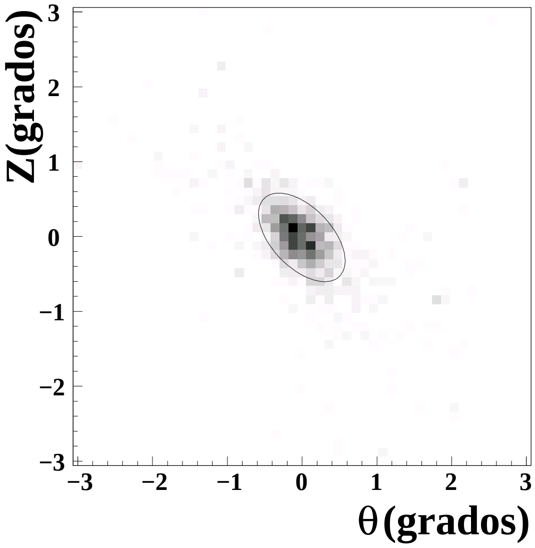

Figure 5.11: *Scheme of the fitting to a bidimensional gaussian, and the determination of the spreading along the major and minor axes, σ_x and σ_y. On the right it is shown an example of the resulting fit to a sample distribution of reconstructed events. The ellipse includes 63% of the reconstructed events.*

In order to represent this function of the plain of the reconstructed directions we calculate and project the equiprobability curve that includes 63% of the events, represented with an ellipse over-imposed to the diagrams of the reconstructed directions distributions. The major and minor axis of this ellipse, σ_x and σ_y, are significant of the achieved resolution in the direction reconstruction process.

The values obtain in the fitting of the distributions corresponding to the different observation directions and primaries are shown in table 5.4, where the values for the center of masses of the distribution, along with the values of the major and minor axes of the ellipse and its rotation angle with respect to axis Z are shown.

It can be observed that for γ events, the position of the center of the distribution matches almost perfectly the incoming direction. For protons, the error in the position of the center of the distribution is slightly larger, being in any case lower that 0.15 degrees, due mainly to the limited statistics of the sample after the trigger and imposed cuts. On the spread of the reconstructed directions, it can be highlighted that in most of the distributions of the reconstructed directions there is a clear radial asymmetry with respect to the observed direction. This fact is specially clear in γ-showers, while in protons showers, due partly to the limited statistics but also to the

		γ-rays				
Zenith	Azimuth	$\overline{\theta}$	$\overline{Z}$	σ_x	σ_y	α
10	0	-0.004	0.042	0.42	0.66	7.
	45	-0.014	-0.054	0.60	0.66	41.
	90	-0.014	-0.002	0.46	0.56	104.
30	0	0.014	-0.057	0.52	0.79	0.
	45	0.002	-0.011	0.45	0.78	44.
	90	0.011	-0.004	0.44	0.57	101.

		protons				
Zenith	Azimuth	$\overline{\theta}$	$\overline{Z}$	σ_x	σ_y	α
10	0	0.021	-0.099	0.74	0.90	-16.
	45	-0.142	-0.049	0.68	0.73	121.
	90	0.102	-0.039	0.69	0.78	107.
	0	0.071	-0.014	0.76	0.85	-13.
	45	0.032	-0.034	0.53	0.89	40.
	90	0.022	0.032	0.54	0.66	102.

Table 5.4: *Parameters of the fitted values to the distributions of reconstructed directions: $\overline{\theta}$ and $\overline{Z}$ determine the position of the geometric center, the width of the distribution along the major axes is given by σ_x and σ_y, and α represents the rotation of the ellipse with respect to the zenith angle.*

large errors in the reconstruction of the Čerenkov front, this fact is not so important. This translates in highly elongated fitted ellipses. The rotation of the fitted ellipse with respect to the coordinate axes shows a dependence with the observed azimuth angle, as for 0, 45 and 90 degrees of azimuth, the rotation angle of the ellipse, α (see table 5.4) shows values close to 0, 45 and 90 degrees. This relationship originates in the geometry of the heliostat field employed in the experiment. The heliostats are spatially distributed in an asymmetrical way, with a larger axis in the East–West direction compared to the North–South axis. Therefore it is evident that the asymmetry of the reconstructed distributions is due to the geometric asymmetry of the heliostat field. As the East–West baseline is larger, the precision in the determination of θ is larger that in Z. In fact, the ration between the two baselines is of the order of two, similar to the ratio of σ_x and σ_y.

Last we must comment that the proton distributions show a mean deviation with respect to the observed direction of 0.73 degrees, a value slightly over the one obtained for γ-showers, 0.57 degrees. This is comprehensible if we take into account that protons come from a great range of directions around the observed direction, while γ-rays come from a point source. As it was shown in §5.1.2, the distribution of the incident angles of protons with respect to the observed direction (ω) has a mean value of ~ 0.7 degrees, which matches the mean reconstructed deviation. This indicates that the identification and reconstruction method does not show a tendency to concentrate events toward the observed direction.

It is not useful to impose a cut on the maximum allowed deviation with respect to the observed direction, on the reconstructed events, in order to reduce the number of proton events, as the difference in the distributions for both primary types is not large enough.

5.3 Comparison with real data

As the GRAAL experiment has been taking data since July 1999, it has been possible to accomplish a fine tuning of the simulation to the characteristics of the real telescope (see §3.1). It is also possible to carry out a comparison of the different parameters obtained of the analysis of the real data with those obtained from the analysis of the simulation described in this work. Results shown in this section correspond to a comparison with the real data measured in an observation run on the Crab Nebula on the 30^{th} of December 2000. The analysis of other data collected in the same period yield similar results. Other, more exhaustive comparison are been carried out by other collaborators [21].

For the chosen run the data taken was done over a range of observation angles from (20^o Zenith, 16^o Azimuth) to (41^o Zenith, 26^o Azimuth). As there is no simulated events over that directions interval a close fixed direction was chosen: (45^o Zenith, 10^o Azimuth).

In order to carry out this comparison six parameters have been chosen: a) the number of pulses employed to carry out the assignment in the first direction grid, that is, the number of pulses above threshold ($n_1 \cdot \sigma$) in the four traces; b) the number of pulses that the method adjusts in this first grid $N_{\max}$; c) the number of pulses that finally are assigned to one heliostat, N_h; d) the error in the assignment done in the first grid, given by χ_1 (ns):

$$\chi_1 = \sqrt{\sum_i^{N_{\max}} (\Delta t_i)^2 / N_{\max}}$$

where Δt_i is the time difference between the real pulse and the closest theoretical pulse; e) the error in the final identification, given by χ_2 (ns) obtained from the heliostat–pulse assignments as:

$$\chi_2 = \sqrt{\sum_i^{N_h} (\Delta t_i')^2 / N_h}$$

where $\Delta t_i'$ is the time difference between the real pulse and the pulse of the theoretical heliostat with whom it has been identified; and f) the value of the total intensity of the trace, calculated as:

$$IC = \sum_j^{N_c} \sum_i^{N_b} (V_{ij} - \overline{V}_j)$$

where N_c is the number of cones (4), N_b is the number of bins in each trace (1000), V_{ij} is the value of the voltage in bin i of cone j, and $\overline{V}_j$ is the mean value of the voltage in the trace of cone j.

In figure 5.12 the different distributions are shown, normalized to the area, of the described parameters, segregating γ-rays from protons and the real sample. Units in the coordinates axis correspond, in all cases, to the number of events per bin.

In general it can be appreciated that the distributions obtained for γ-ray simulated events and protons show similar characteristics. Therefore we will talk about simulated events, in comparison with real events.

In diagrams a), b) and c) it can be appreciated that the maximum value reached in the x-axis by real distributions is slightly lower than that reached by simulated distributions. This can be explained taking into account that in the real experiment usually about five heliostats are inoperative sue to mechanical or tracking errors, and that pointing errors, not considered in the simulation, take place, thus lowering the amount of light collected from those heliostats. In the same way, in diagram a) differences between the simulated distributions and the real one can be appreciated for a low number of detected heliostats ($\sim$5–15), difference that does not appear in the two following distributions. The first distribution corresponds to almost raw events (it is only required that the pulses are larger than $(n_1 \cdot \sigma)$), while in the second and third graphics a fitting of the pulses to the expected signal has been carried out. This points to the fact that in the real data there are a series of pulses of relatively low amplitude (about two per trace) that are later discarded in the analysis. This indicates that they are noise pulses. This is perfectly compatible with what was said in §3.1.5, where the differences between the spectrum of amplitudes o the background noise in the simulation and the

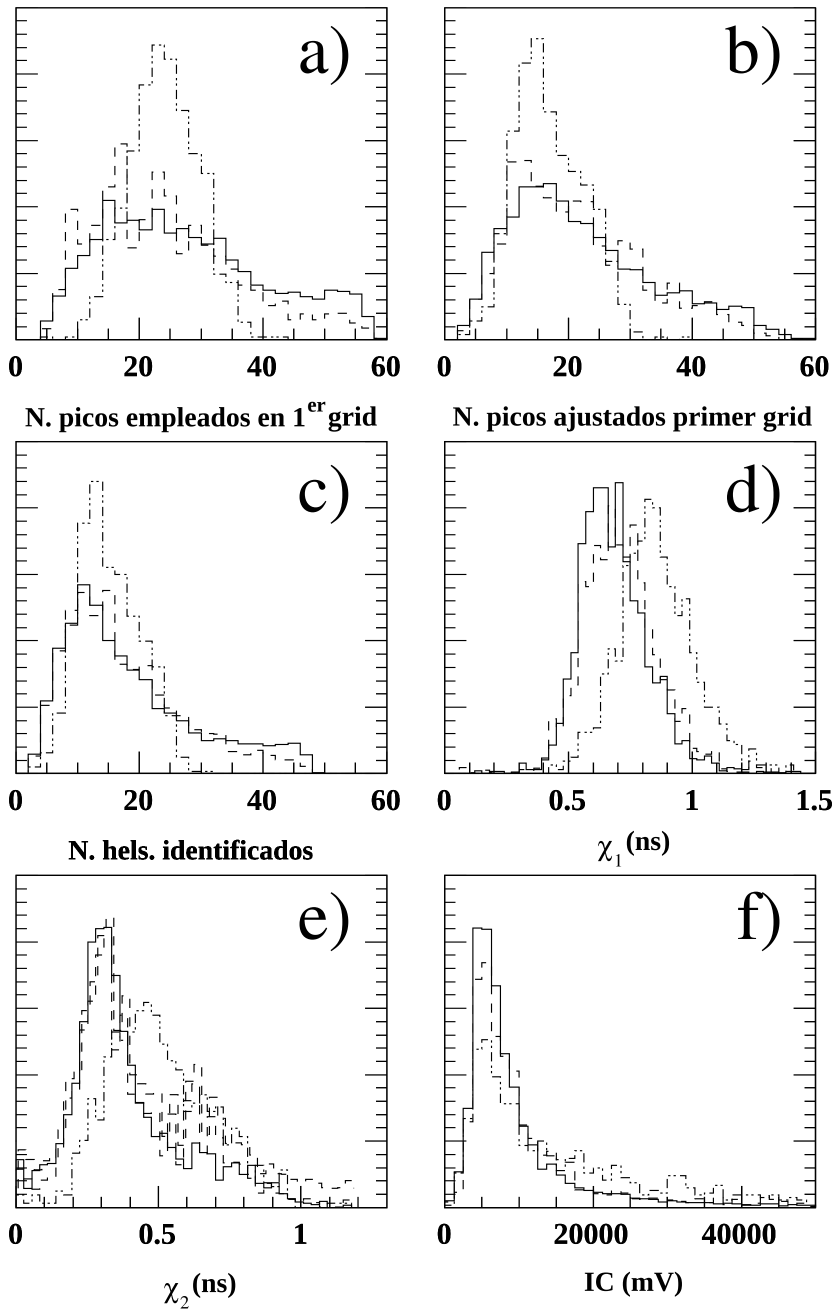

Figure 5.12: *Comparison of the distributions obtained from Monte Carlo for showers initiated by γ-rays (solid line), protons (dashed line) and real data (dotted line).*

real data are discussed. In the latter, the probability to have large amplitude pulses is larger that in the simulation, which reflects in the distributions here discussed.

The error distributions of the fittings carried out, d) and e), point, as expected to the fact that the real data yield slightly larger errors that the simulation. The mean values for the simulated events are ~ 0.7 ns and ~ 0.4 ns for χ_1 and χ_2 respectively, while for real distributions these errors are ~ 0.8 ns and ~ 0.5 ns. The differences are very small, and correspond to uncertainties in the knowledge of the positions of the cones with respect to the heliostats of a few centimeters.

Last, in graphic f) parameter IC is show, showing a slight discrepancy at large values, where the distribution for real data is slightly larger that for simulated distributions. The reason for this discrepancy is double. First, as it has been considered in plot a), the real noise seems to have a larger number of large amplitude pulses, which, no doubt, will increase the value of IC. On the other hand, in the simulation only events with energy up to 1 Tev for γ-rays and 4 TeV for protons are taken into account. More recent simulations where the energy range has been extended to higher energies show reduced differences.

Finally, the concordance between simulation and real data is reasonable, taking into account the large number of uncertainties in a experiment of these characteristics that can not be taken into account in the simulation as, not only the detector is simulated, but all the development of the shower in the atmosphere, whose properties, even selecting nights with very good observing conditions, present fluctuations that cannot be taken into account in the simulation.

5.4 Limits of the method

As it has already been shown in this chapter, GRAAL can detect γ-rays with an energy threshold similar or lower to existing conventional telescopes in operation. Due to the particular detection system of the GRAAL experiment, where light coming from groups of heliostats is collected in just one photomultiplier. it has been necessary to develop an analysis method to identify in the detected traces the pulses with the heliostats they come from. Thanks to this technique GRAAL is comparable to the other solar-plant telescopes in capacity to analyze the Čerenkov front, though it does not reach the energy thresholds expected in other experiments (CELESTE or STACEE) where each PMT only sees one heliostat.

In any case the use of soar plants as γ-ray telescope suffers from several intrinsic inconvenients very hard to avoid with the techniques presently in use:

The mean problem is the incapacity to determine with accuracy the **position of the core** of the shower. This uncertainty make sit impossible to determine with precision two most important parameters of the shower: the energy and the incident direction.

As it is well know, though the amount of atmospheric Čerenkov light generated by a shower increases with the energy of the primary, the uncertainty in the position of the core reduces in a great way this correlation. This is due to the fact that the Čerenkov light collected by the heliostat field that corresponds to showers of very high energy with the core far away from the center, is similar to that of low-energy showers with the core near the center.

About the incident direction of the detected cosmic ray, the analysis of the signal can locate the position of the center of the sphere formed by the Čerenkov front. But in order to precisely reconstruct the direction it would be necessary to know the impact point on the ground (see figure 5.6).

Unfortunately, for the moment, no group presently working in the detection of γ-rays with solar plants has developed a method, that through the analysis of the Čerenkov front can estimate the core position. As it was shown in the previous chapter, in a realistic detector, the limited sampling of the Čerenkov front along with the low detection efficiency ($\sim 15\%$) invalidate all the methods to locate the core in convergent view. In parallel view the center of gravity of the Čerenkov-light distribution on the ground is a good estimator of the core position. But due to the limited field of view, in parallel view the amount of detected light is significantly lower, and therefore the energy threshold is higher.

None of the methods tried in this work has been able to find parameters to efficiently discriminate the hadronic background from γ-rays. As described in chapter 4, though in the more idealistic cases it is possible to segregate both primary types, under realistic conditions the differences observed with restricted-field-of-view detectors are overtaken by the fluctuations due to the limited sampling of the Čerenkov front and the fluctuations induced by the low detection efficiency of photons.

All these drawbacks do not bar the detection of γ-ray sources. At present both the STACEE [22] and CELESTE [23] collaborations base their measurements on the difference of events measured in ON (on the source) and OFF (of the source) periods, a value which is very sensitive to small variations on the background light. If no analysis of the characteristics of the showers front is carried out, small differences between both periods can lead to the creation of artificial signals or anti-signals. In GRAAL [24, 21], we employ the information of the shower front reconstruction to carry out a normalization based of the number of events whose reconstructed direction is located on the wings of the corresponding distribution, and considering that such events are due only to noise. This hypothesis is referenced by the results shown in figures 5.9 and 5.10).

The determination of the core position would significantly increase the sensitivity of this technique thanks to a better angular resolution (angular cuts). In order to do this several alternative techniques are being studied, as a mixed observation configuration, with part of the heliostat field observing in parallel view, in order to locate the core position, while the rest of the heliostats are in convergent view to trigger low energy events. Other possibilities are being tested as, for example, the definition of several convergent points at different atmospheric depths, each observed by different groups of heliostats.

Conclusions

In the present work, the characteristics of the γ-ray telescope GRAAL have been determined with a detailed simulation based on experimentally tested parameters. This work has not been limited to a theoretical exposition of the experiment, as with the first data taking of the experiment in summer 1999, it has been possible to approximate the simulation to the real experiment.

In order to carry out this study, more than 10^5 atmospheric showers have been simulated, initiated both by γ-rays and protons in the energy range 0.05–4 TeV, using the Monte Carlo simulation code CORSIKA. We have modeled the optical components (heliostats, Winston cones, ...) that collect the Čerenkov light, and the electronics (cables, amplifiers and trigger system) that provide with the signal. The resulting traces from this process resemble very closely the real data.

For the first time a method to identify the pattern of Čerenkov pulses detected by the heliostats has been developed, allowing for the identification of the heliostats to peaks with a high accuracy, which provides very valuable information on the Čerenkov front (spatial and temporal distribution). This technique positions GRAAL, in relationship to the measurement of the Čerenkov front, in a similar state to other experiments using soar plants that employ a secondary optics and many electronic channels, which much more expensive and difficult to calibrate.

The more important parameters of the GRAAL detector have been determined. The effective area reaches a saturation value around 12000 $\mathrm{m}^2$for γ-rays. Energy threshold is about 250 GeV for γ-rays with 30 degrees of zenith angle. Though this value is higher than that attainable with more complex heliostat–PMT setups, it is lower than that of conventional present-day telescopes.

On the other hand, our simulation predicts a background cosmic trigger rate of about 3–4 Hz, in good concordance with real data.

Regarding the angular resolution, for γ-rays coming from a point source, the response function ("Point Spread Function") is described by a asymmetric bidimensional gaussian with values for σ_x and σ_y around 0.5 and

0.7 degrees. For the isotropic cosmic background these values are around 0.7 and 0.8 degrees respectively. The angular imprecision for γ-rays is caused basically by the uncertainty in the core position. This limitation is common to all solar-plant experiments. If one effective method to determine the core position would be developed, the angular resolution for γ-rays would become better, and so the detection sensitivity, as it would be possible to impose angular cuts in the analysis.

In order to better understand the Čerenkov signals detected a general study of the properties of the Čerenkov component of atmospheric showers detected by a array of Čerenkov-light detectors has been carried out, which can be extrapolated to any solar-plant experiment, and in general to and array of Čerenkov-light detectors with a limited field of view ($\sim 0.5^{o}$). Possible methods to reconstruct the principal parameters of the primary as the particle type or core position have been studied. It has been shown that both the fluctuations in the Čerenkov-light density and the time structure of the shower front and significantly different for γ-rays and protons. Unfortunately, the restricted field of view (even in convergent view) limits the separation power of these methods. In particular, the string time fluctuations of hadron showers are not detectable to a limited-field-of-view detector. Besides, though an heliostat field provides with a huge mirrored surface, the limited spatial sampling of the signal imposes additional restrictions to the methods. These problems, which are common to other experiments which employ solar plants, limit the potential of this technique in comparison with conventional Čerenkov telescopes.

In any case, it has been possible to detected γ-ray signal using this technique, employing the ON–OFF difference (CELESTE, STACEE) or employing a normalization and subtraction method (GRAAL). Under these conditions, solar plants are a very competitive method in the detection of γ-rays, due to the low energy threshold (specially in configuration with one PMT per heliostat), the low cost of the experiment, and the relatively low complexity, when compared with other techniques. Last, it cannot be discarded that, with the use of new observing strategies, which are under study at present, as mixed observation in parallel and convergent view, it would be possible to attain the primary parameters, which no doubt would in increase the sensitivity and potential of this kind of detectors.

Bibliography

[1] G. Wettermark. The solar power plants at Almeria. *Energy research commission, Stockholm*, 1986.

[2] E. Lorenz and R. Mirzoyan. Measurement of the night sky light background at La Palma. Technical Report MPI-PhE/94-35, Max-Planck-Institut für Physik, 1994.

[3] R. Monterreal. Informe de la PSA. Technical Report R12/95 RM, Plataforma Solar de Almería, 1995.

[4] K. P. Braun. HELIOS simulation of the incident flux distribution on the TSA receiver based on HERMES II measurements. Technical Report R24/94, Plataforma Solar de Almería, 1994.

[5] W. P. Welford and R. Winston. *The optics of nonimaging concentrators*, chapter 4. Academic Press, New York, 1978.

[6] The CELESTE collaboration. CELESTE experimental proposal: Čerenkov low energy sampling & timing experiment. 1996.

[7] J. N. Capdevielle et al. The Karlsruhe Extensive Air Shower Simulation Code CORSIKA. Technical Report KfK 4998, Kernforschungszentrum, Karlsruhe, 1992.

[8] J. N. Capdevielle. *J.Phys.G*, 15:909, 1989.

[9] A. Capella and J. T. T. Van. *Phys.Lett.B*, 93:146, 1980.

[10] P. K. F. Grieder. In *Proc. 16th ICRC*, volume 9, page 161, Kyoto, 1979.

[11] W. R. Nelson, H. Hiroyama, and D. W. O. Rogers. The EGS4 code system. Technical Report 265, SLAC, 1985.

[12] J. Linsley. In *Proc. 20th ICRC*, volume 2, page 442, Moscow, 1987.

[13] F. C. Andrés et al. Atmospheric effects on Cherenkov light from extensive air showers. In *Proc. 16th ECRS*, 1998.

[14] R. et al. Mirzoyan. On the influence of afterpulsing in PMTs on the trigger threshold of multichannel light detectors in self-trigger mode. In *Conference Record of Beune96-First Conference on New Developments in Photodetection*, 1996.

[15] V. R. Chitnis and P. N. Bhat. Čerenkov photon density fluctuations in extensive air showers. *Astroparticle Physics*, 9:45–63, 1998.

[16] V. R. Chitnis and P. N. Bhat. Simulation studies on arrival time distributions of Čerenkov photons in extensive air showers. *Astroparticle Physics*, 12:45–64, 1999.

[17] B. Wiebel. Chemical composition in high energy cosmic rays. Technical Report WUB 94-08, Gesamthochschule Wuppertal, April 1994.

[18] R. A. Ong et al. A new atmospheric Cherenkov detector using the heliostats of Solar Two. In M. Cresti, editor, *Towards a Major Atmospheric Cherenkov Detector-IV (Padova)*, 1995.

[19] The Whipple collaboration. The spectrum of TeV γ-rays from the Crab Nebula. *Astrophys.J.*, March 1998.

[20] *Statistics for Nuclear and Particle Physics*. Cambridge University Press, 1986.

[21] María Díaz Trigo. PhD thesis, U. Heidelberg, prevista para 2002.

[22] R. A. Ong et al. STACEE observations of active nuclei and other galactic sources. In *Proc. 27^{th} ICRC (Hamburg, Alemania)*, pages 2593–2596, 2001.

[23] D. Dumora and the CELESTE Collaboration. Search for high energy gamma ray pulsar emission with the CELESTE Experiment. In *Proc. 27^{th} ICRC (Hamburg, Alemania)*, pages 2436–2439, 2001.

[24] F. Arqueros et al. Very high-energy observations of the Crab nebula and other potential sources with the GRAAL experiment. *aceptado en Astroparticle Physics*, 2001.